

2023

Multifunctional photoacoustic materials for neural engineering

<https://hdl.handle.net/2144/46660>

Boston University

BOSTON UNIVERSITY
COLLEGE OF ENGINEERING

Dissertation

**MULTIFUNCTIONAL PHOTOACOUSTIC MATERIALS
FOR NEURAL ENGINEERING**

by

NAN ZHENG

B.E., Southern University of Science and Technology, 2018
M.S., Boston University, 2022

Submitted in partial fulfillment of the
requirements for the degree of
Doctor of Philosophy

2023

© 2023 by
NAN ZHENG
All rights reserved

Approved by

First Reader

Chen Yang, PhD
Associate Professor of Electrical and Computer Engineering
Associate Professor of Chemistry
Associate Professor of Materials Science and Engineering

Second Reader

David Kaplan, PhD
Stern Family Professorship in Biomedical Engineering
Distinguished Professor of Engineering
Distinguished Professor of Biology

Third Reader

Joyce Y. Wong, PhD
Professor of Biomedical Engineering
Professor of Materials Science and Engineering

Fourth Reader

Ji-Xin Cheng, PhD
Moustakas Chair Professor in Photonics and Optoelectronics
Professor of Biomedical Engineering
Professor of Electrical and Computer Engineering
Professor of Materials Science and Engineering
Professor of Chemistry
Professor of Physics

*Il n'ya qu'un héroïsme au monde :
c'est de voir le monde tel qu'il est et de l'aimer.*
— Romain Rolland

[There is only one heroism in the world: to see the world as it is, and to love it.]

Acknowledgments

I am deeply grateful to my advisor, Dr. Chen Yang, for the invaluable opportunity she offered, the inexhaustible patience she demonstrated, the constant encouragement she extended, and the expert guidance she provided upon me throughout my journey. Her support, mentorship, and dedication have profoundly shaped both my academic and personal growth, deepening my understanding of the subject matter, refining my abilities of critical thinking, and igniting my passion for lifelong learning. I consider myself incredibly fortunate to have had her as my advisor.

Thank Dr. David Kaplan, Dr. Joyce Wong, Dr. Timothy O'Shea and Dr. Jixin Cheng for serving as my dissertation committee members and providing valuable suggestions to help me with my research.

Thank all my colleagues, the current and former group members in Yang lab and Cheng lab, including Dr. Yimin Huang, Dr. Amartya Dutta, Dr. Ying Jiang, Dr. Linli Shi, Yueming Li, Ran Cheng, Guo Chen, Zhiyi Du. Your selfless assistance and collaborative efforts have greatly expedited my research progress. I sincerely extend my appreciation to our incredible collaborators, in particular Dr. David Kaplan, Dr. Vincent Fitzpatrick, Dr. Xiaoting Jia, Dr. Shan Jiang and Jongwoon Kim for their invaluable contributions and exceptional collaborations.

I would like to express deepest appreciation to my family for their unwavering support. Either the encouragement or the criticism spurred me going forward. And thank you Yiting, it still feels like a dream, meeting you within the first month of my arrival in Boston. You transformed my PhD study from a potentially painful endeavor into a journey with sweetness and joy.

And to all my friends, thank you for making my past five years an experience that is truly vivid and unforgettable.

MULTIFUNCTIONAL PHOTOACOUSTIC MATERIALS FOR NEURAL ENGINEERING

NAN ZHENG

Boston University, College of Engineering, 2023

Major Professor: Chen Yang, PhD

Associate Professor of Electrical and Computer
Engineering

Associate Professor of Chemistry

Associate Professor of Materials Science and
Engineering

ABSTRACT

Understanding the complex information transfer process of our nervous system is one of the most urgent needs in the biomedical community. Neuromodulation is a technique that can artificially influence or modulate the activity of the target neurons. It's an inevitable tool in both the neuroscience study but also the clinical treatment of neurological diseases. The conventional method for neural modulation is the electrical stimulation using implantable electrodes. However, its intrinsic current leakage problem is an obstacle for further improving its performance in clinical scenarios because of the finite spatial resolution and recording artifacts. In general, an ideal method should be able to modulate neural activities with a high spatial, temporal and functionality specificity but without biocompatibility and reliability issues even in long term.

Photoacoustic stimulation is an emerging light-mediated, non-genetic neural modulation method with high spatiotemporal resolution. Multiple devices have been

designed in the past few years. But there are still several gaps to be filled to further expand its applications. One is the material mismatch, and another is that more function is needed, for example the capability of simultaneous recording. My research focused on the design and development of two new types of photoacoustic materials to expand the use of photoacoustic stimulation. A soft hydrogel film and a multifunctional fiber-based emitter for photoacoustic neuromodulation have been developed in my Ph.D. research. The study on these materials increased our knowledge to photoacoustic neurostimulation, also help us to investigate the effect of photoacoustic neuromodulation in the treatment of neurological and neurodegenerative diseases.

Contents

1	Introduction	1
1.1	Introduction to neuromodulation techniques	1
1.2	Current available neuromodulation methods	2
1.2.1	Electrical stimulation	3
1.2.2	Ultrasound stimulation	4
1.2.3	Optogenetics	5
1.2.4	Photothermal neuromodulation	6
1.3	Development in photoacoustic neuromodulation methods	7
1.3.1	The principle of photoacoustic neuromodulation	8
1.3.2	Fiber-based optoacoustic emitter	9
1.3.3	Tapered fiber-based photoacoustic emitter	10
1.3.4	Semiconductor photoacoustic nanoparticles	12
1.4	Summary	12
2	Photoacoustic Carbon Nanotubes Embedded Silk Scaffolds for Neural Stimulation and Regeneration	15
2.1	Introduction	15
2.2	Materials and Methods	18
2.2.1	Preparation of Silk and Functionalized CNT	18
2.2.2	Fabrication of CNT/Silk Film and CNT/Silk Roll Scaffolds . .	19
2.2.3	Characterization of CNT/Silk scaffolds	19

2.2.4	Cortical neuron and dorsal root ganglia (DRG) isolation and culture	20
2.2.5	MTS Viability Assay	22
2.2.6	Histological Analysis	22
2.2.7	<i>In Vitro</i> Neurostimulation	22
2.2.8	Extracellular Recording of DRG Explants	23
2.2.9	Sytox Green Nucleus Acid Staining	23
2.2.10	Immunocytochemistry	24
2.2.11	Confocal Imaging and Image Analysis	25
2.2.12	ELISA Assay	26
2.2.13	Statistical Analysis	26
2.3	Results and Discussion	27
2.3.1	Fabrication and characterization of CNT/Silk scaffold	27
2.3.2	In vitro and in vivo assessment of CNT/Silk scaffold biocompatibility	33
2.3.3	CNT/Silk scaffold stimulated neuronal activities through PA waves	37
2.3.4	PA stimulations promote neurite extension	42
2.4	Conclusion	50
3	Multifunctional Fiber-based Optoacoustic Emitter as a Bidirectional Brain Interface	53
3.1	Introduction	53
3.2	Materials and Methods	57
3.2.1	Multifunctional fiber fabrication and optoacoustic emitter integration	57
3.2.2	Impedance measurement	59

3.2.3	Optoacoustic wave characterization	59
3.2.4	In vitro neurostimulation and calcium imaging	59
3.2.5	Implantation surgery procedure	60
3.2.6	In vivo electrophysiology recording and optoacoustic stimulation	61
3.2.7	Foreign body response assessment via immunohistochemistry .	62
3.2.8	Statistical information	63
3.3	Results	64
3.3.1	Design, fabrication and characterization of mFOE	64
3.3.2	mFOE stimulation of cultured primary neurons	70
3.3.3	In vivo simultaneous optoacoustic stimulation and electrophys- iological recording	77
3.3.4	Foreign body response comparison between mFOE and stan- dard optical fiber using immunohistochemistry	83
3.4	Discussion	85
4	Photoacoustic Neuromodulation in Disease Treatments	89
4.1	Application in Retinal Degenerative Diseases	90
4.1.1	Introduction to Retinal Regenerative Diseases (RRDs)	91
4.1.2	Retinal Degenerative Disease Model	92
4.1.3	Experimental Methods	93
4.1.4	Results	93
4.2	Application in Epilepsy	95
4.2.1	Epilepsy Disease Model	96
4.2.2	Experimental Methods	97
4.2.3	Results	98
5	Conclusion and Outlook	103
5.1	Conclusion	103

5.2 Outlook	104
A Appendix	106
A.1 Mechanical Index Calculation	106
References	107
Curriculum Vitae	127

List of Tables

2.1	Mechanical properties of silk and CNT/Silk films.	29
3.1	The Young's modulus of polymer materials used in mFOE (Vinogradov and Holloway, 1999; Khun and Liu, 2013) and the commercial silica optical fiber. (Holmes et al., 2022)	66

List of Figures

1·1	The schematic of the photoacoustic effect. A ultrasound wave is generated from the enclosed cell under the chopped light.	8
1·2	The schematic of a fiber-based photoacoustic emitter (FOE). The input laser is guided by the optical fiber and entering the photoacoustic emitter at the tip of FOE. Then the laser energy is converted into a point source ultrasound wave.	11
1·3	Spatio-temporal resolution of various neuromodulation methods. The open circle represents non-invasive methods and the black dots invasive methods. Photoacoustic neuromodulation can achieve a spatiotemporal resolution similar to optogenetics but is genetic-free.	13
2·1	Neurite tracing of immunofluorescence images of cortical neurons cultured on CNT/silk film(a) and glass substrate(b). Neurons were labeled with anti-Tau antibody (green).	25
2·2	The zeta-potential of raw CNT and DPSE-PEG functionalized CNT solution. Negative charges were introduced after functionalization. . .	27
2·3	Schematic of the fabrication process of CNT/Silk PA films.	28
2·4	The CNT embedded silk roll was fabricated through a self-folding strategy.	28
2·5	Absorption spectrum of silk and CNT/Silk film (20 $\mu\text{g}/\text{ml}$ and 40 $\mu\text{g}/\text{ml}$). . .	29

2.6	Characterization of PA properties of CNT/Silk films.: (a) Schematic of the PA measurement. (b) Acoustic wave generated by a 20 $\mu\text{g/mL}$ CNT/Silk film in time domain and frequency domain measured by a 10 MHz transducer. Laser pulse energy of 74.7 μJ	30
2.7	Normalized mean peak to peak amplitude of the PA waves as a function of the concentration of CNT (left panel) and laser pulse energy (right panel). Error bar, $n = 3$. Red dotted lines, fitting curves.	31
2.8	Temperature as a function of time measured at the surface of the area under laser illumination for silk film and CNT/Silk film. Laser durations of 3 ms, 10 ms, 20 ms, 50 ms and 100 ms. Laser pulse energy 53 μJ . Green solid lines indicate laser onset. $n = 3$, shaded area: \pm standard error of the mean (s.e.m.).	32
2.9	Biocompatibility of CNT/Silk film evaluated in vitro and in vivo. (a) Representative confocal image of cortical neurons cultured on CNT/Silk film. Neurons were fixed and stained with anti-Tau antibody (green) and DAPI for cell nuclei (cyan) at DIV7. (b-c) Quantification of the number of neurons per area (b) and the total neurite length per area (c). ROI: region of interest, 0.1013 mm^2 for all samples. The number of neurons was analyzed by counting the DAPI-stained nuclei. The total neurite length was analyzed by counting the length of anti-Tau labeled neurites. (d) Cell viability of neurons cultured on silk film as control, CNT/Silk film, silk film with freeform CNT measured by MTS assay. Error bars represent standard deviation. (e-l) Representative images of mouse skin with CNT/Silk roll implants with different CNT concentrations. (e)-(h), Day 3. Mild inflammation; (i)-(l), Day 30. it: insertion tract; csr: CNT/Silk roll; f: fibroplasia and granulation tissue.	34

2·10	Calcium imaging was performed on an inverted wide field fluorescence microscope to monitor neuronal activities. Pulsed laser light was delivered through a multimode optical fiber. The fiber location and the illumination area were controlled by a micromanipulator. DM: dichroic mirror.	37
2·11	(a, b) Representative calcium images of GCaMP6f-transfected cortical neurons at DIV 14 cultured on CNT/Silk film before (a) and after (b) the PA stimulation. Laser: 3 ns laser applied for a 5 ms duration with a 1.7 kHz repetition rate (corresponding to 8 pulses) and 14.7 μ J pulse energy. (c) Map of the maximum fluorescence change $\Delta F/F_0$ induced by the PA stimulation. Dashed lines: Illumination area. Scale bars: 100 μ m.	38
2·12	(a) Representative calcium traces of neuron cultured on CNT/Silk scaffold within the laser illumination area (CNT/Silk light +, orange), out of the laser illumination area (CNT/Silk light -, black) and cultured on silk scaffold within the laser illumination area (Silk light +, blue). (b) Representative calcium traces of neurons cultured on CNT/Silk film responding to PA stimulation with the pulse energy of 23.5 μ J (red), 14.7 μ J (orange) and 8.8 μ J (yellow).	39

2·13	(a-d) Colormaps of fluorescence change in neurons cultured on CNT/Silk scaffold with laser pulse energy of 23.5 μ J (a), 14.7 μ J (b) and 8.8 μ J (c) and silk scaffold with laser pulse energy of 14.7 μ J (d). All PA stimulation was performed at 5 s and marked by the red dashed lines. The duration of each stimulation was fixed at 5 ms. (e) Average of maximum fluorescence intensity changes shown in (a-d). Error bars represent standard deviation (n > 14, ** p < 0.01, n.s. p = 0.982, one-way ANOVA and Tukey's means comparison test). (f) Calcium trace of the neuron marked by the solid circle in Figure 2·11 undergone repeated PA stimulation.	40
2·14	No lasting damage was confirmed by Sytox Green nucleus acid staining. Neurons in the sample group were stimulated 5 times (pulse energy of 14.7 μ J, duration of 5 ms) with an interval of one minute in between. Dead neurons with a stronger Sytox Green signal (fluorescence intensity > 600 a.u.) before the stimulation were identified as the positive control group. Sytox Green fluorescence intensity of neurons in both groups remains the same 10 minutes after stimulation. The sample group shows much lower Sytox Green signals compared with the positive control group (463.29 vs 949.67).	42
2·15	Heat profile of CNT/Silk scaffold under the laser illumination. Three pulse energy, 8.8 μ J (a), 14.7 μ J(b) and 23.5 μ J(c) were examined with duration of 5 ms, 50 ms and 500 ms.	43
2·16	Calcium trace of a GCaMP6f transfected DRG at DIV 10 under the PA stimulation with the pulse energy of 14.7 μ J and the duration of 5 ms. The stimulation was triggered at 5 s.	43

2·17	(a) Schematic of extracellular recording and PA stimulation on DRG explants cultured on the CNT/Silk film. (b) Artifacts induced by the laser illumination recorded in the PBS without DRG explants. (c) Extracellular recording of DRG explants cultured on the CNT/Silk film. Red lines: Five repeat photoacoustic stimulations were performed with laser pulse energy of 14.7 μJ	44
2·18	PA stimulation promotes the neurite outgrowth. (a-d) Representative confocal images of DRGs stained for neurofilament (green): DRG cultured on CNT/Silk film with laser illumination (CNT/Silk light +, a) and without laser illumination (CNT/Silk light -, b). DRG cultured on glass bottom dish with laser illumination (Glass light +, c) and without laser illumination (Glass light -, d). Scale bar: 1 mm. (e-h) High-resolution confocal images of DRGs stained with Anti-Neurofilament 200 (NF) for neurites(green) and DAPI for nucleus (cyan). Scale bar: 50 μm . (i) The average neurite coverage area for DRGs in four groups. (j) The average neurite coverage area for PA stimulated DRGs with various stimulation frequency. Control: DRGs cultured on glass without light stimulation (glass light -). All DRGs were allowed to grow for 2 days before stimulation, and were fixed at day 10.	45
2·19	The coverage area of DRGs was determined by a computer algorithm to minimize the artificial error. The polygon was constructed by 360 endpoints along each direction separated by 1°	46
2·20	The schematic of laser pulse train used for investigating the effect of PA dosage. The total duration was fixed at 1 hour. The stimulation frequency was varied from every 30 seconds to every 4 minutes. Within each 5 ms pulse train, 8 pulses with pulse energy of 14.7 μJ were provided.	47

2·21	Impact of PA stimulation on the expression of BDNF and NGF. (a–b) The average concentrations of BDNF (a) and NGF (b) of PA-stimulated and unstimulated DRGs. Samples were collected 24 hours after PA stimulations. PA stimulations were provided every 2 minutes within the total duration of 1 hour. The stimulation condition was a laser train duration of 5 ms 1.7 kHz repetition rate, and the pulse energy of 14.7 μ J.	48
3·1	Confocal imaging of NeuN labelled neurons. At certain depth, NeuN labelled neurons are distributed unevenly because of the intrinsic structure of mice brain. For fair comparison, those samples were excluded from the later quantitative analysis. Scale bar: 100 μ m.	64
3·2	Schematic of mFOE for bidirectional communication with neurons. Input laser pulse (red) is used to generate optoacoustic waves (black mesh next to the emitter at the mFOE tip) by the emitter. Neural activities are recorded by embedded electrodes (brown) as the output electrical signal (blue). Neurons stimulated are highlight in the tan color, in contrast to the unstimulated neurons in the gray color.	65
3·3	Illustration of the thermal drawing process.	66
3·4	Components of the multifunctional fiber, including a PC/PVDF waveguide, BiSn alloy electrodes and PC sacrifice layer.	67
3·5	Optical properties of the waveguide and optoacoustic emitter of mFOE. a. The optical loss of waveguide measured at 1030 nm with the cut-back method. b. Vis-NIR absorption spectrum of CB/PDMS mixture.	68
3·6	Impedance measurements of the BiSn electrodes in multifunctional fiber. Shaded areas and solid curve in the figure represent the standard deviation and mean value respectively.	69

3·7	The coverage area was controlled through tuning the injection pressure and time. Injection time was varied between 1 second and 2 seconds, and the pressure was varied from 2 psi, 3 psi and 4 psi. Scale bar: 50 μm	70
3·8	Top view microscope image of the mFOE. Scale bar: 100 μm	71
3·9	a. Representative acoustic waveforms under different laser pulse energy recorded by a needle hydrophone. b. Frequency spectrum of acoustic waveforms shown in a.	72
3·10	Attenuation curve of optoacoustic wave generated by mFOE along the axial direction. Relative pressure plotted as a function of the distance. Laser pulse energy was fixed at 41.8 μJ	73
3·11	Schematic of in vitro mFOE stimulation and calcium imaging set up. Stimulation: 1030 nm pulsed laser is triggered by a function generator and delivered to the mFOE through an optical fiber. Calcium imaging: Oregon green is excited by 470 nm LED and the fluorescence signal is detected through a CMOS camera.	73

3·12	Calcium transients induced by mFOE in cultured primary neurons.	
a.	Calcium image of primary cultured neurons loaded with OGD-1. Twenty neurons within (orange) and outside (blue) the optoacoustic converter area are circled and labelled. Scale bar: 100 μ m. Solid circle: area outside the converter area; dashed line circle: area within the optoacoustic converter area. b-c. Calcium traces of neurons undergone repeated mFOE stimulations with a laser pulse train duration of 100 ms (red dots). Each pulse train was repeated 5 times. Colors and numbers of the traces are corresponding to the neurons labelled in a. d-g. Average calcium traces of neurons triggered by mFOE stimulation with durations of 200 ms (d), 100 ms (e), 50 ms (f) and 5 ms (g), respectively. Shaded area: the standard deviation (SD). N=15 h. Average maximum $\Delta F/F$ of neurons stimulated by mFOE. N = 15. (n.s.: non-significant, $p > 0.05$; *: $p < 0.05$; **: $p < 0.01$; ***: $p < 0.001$, One-Way ANOVA and Tukey's mean comparison test)	74
3·13	Illustration of the laser pulse train for 5 bursts with 100 ms duration at 1Hz.	75
3·14	Calcium imaging of neurons before and after mFOE stimulation with duration of 200 ms. Neurons were subjected to repeated stimulation using mFOE with a duration of 200 ms, repeated five times. The morphology and calcium signal of the same field of view were subsequently imaged and compared. No obvious differences were observed. Scale bar: 100 μ m.	76

3·15	Average calcium traces of laser only control groups. The laser duration was same with three conditions tested in mFOE stimulation (200 ms, 100 ms and 50 ms). Laser light with pulse energy of 41.8 μ J was triggered at the time point labelled by the red bar. Shaded areas: standard deviation. (N=3)	76
3·16	Temperature change of the optoacoustic emitter integrated on mFOE. The pulse energy was maintained at 41.8 μ J and the burst duration was varied from 50 ms (blue), 100 ms (yellow) to 200 ms (orange). Laser was trigger at 2.5 second as labelled by the red bar.	77
3·17	a. Illustration of the mFOE enabled bidirectional neural communication using laser signal as input and electrical signal as readout. b. mFOE was implanted into hippocampus of a wild type C57BL/6J mouse. c-f. Simultaneous optoacoustic stimulation and electrophysiological recording performed at 3 days (c), 7 days (d), two weeks (e) and one month (f) after implantation. Blue dots the laser pulse trains. For each laser train: 50 ms burst of pulses, pulse energy of 41.8 μ J, laser repetition rate 1.7 kHz.	79
3·18	LFP recording of sham control stimulation experiments. a. Electrophysiological recording under light only stimulations delivered through a bare multifunctional fiber without optoacoustic emitter. b. Simultaneous optoacoustic stimulation and electrophysiological recording of a euthanized mouse. Same laser condition was used: pulse energy of 41.8 μ J, 50 ms burst of pulses, 1 Hz, blue dots indicate the laser onset.	80

3·19	a. Part of the filtered spontaneous activity containing two separable group of spikes recorded by mFOE electrode at one month after im-plantation. b. Principal-components analysis (PCA) of the two group of spikes. c-d. Waveform of two group of spikes in b.	81
3·20	a. Local field potential (LFP) recorded by mFOE one month after implantation with an alternating anaesthesia level (0.5-3% v/v isoflu-rane). b-d. different LFP responses induced by varying the concentra-tion of isoflurane: b corresponds to the initial stage (0.5% of isoflurane level); c corresponds to the burst/suppression transition stage (after increasing the isoflurane level to 3%); d corresponds to the suppression stage (the isoflurane level was maintained at 3% and took effect). . .	82

3·21	Foreign body response comparison of mFOE and silica fiber using immunohistochemistry. a-d. Immunohistochemistry images of mouse brains implanted with mFOE and silica fiber one month after implantation (N = 3). Scale bar: 100 μ m. Brain slices were labelled with the neuron-specific protein (NeuN, cyan), ionized calcium-binding adaptor molecule 1 (Iba1, red) and glial fibrillary acidic protein (GFAP, green). e. Number of neurons in the field of view, calculated by counting the NeuN-positive cells for mFOE and silica fiber at 3 days and 1 mon after implantation. f. Microglial reactivity, assessed by counting the Iba-1 labelled area, for mFOE and silica fiber at 3 days and 1 mon after implantation. g. Astrocyte reactivity, assessed by counting the GFAP labelled area, for mFOE and silica fiber at 3 days and 1 mon after implantation. For each experimental group, two to four brain slices were used from each mouse (N= 3). (n.s.: non-significant, $p > 0.05$; **: $p < 0.01$; ***: $p < 0.001$, One-Way ANOVA and Tukey's mean comparison test)	84
4·1	Image of MEA recording setup. Two manipulator were used to control the position of retina and fiber. Ames's medium was supplied through the perfusion system. The response of ganglion cells under photoacoustic stimulation was recorded during the experiment.	94
4·2	a-b. Ganglion cells response under repeated photoacoustic stimulation recorded from two separate channels. c. Schematic of laser pulse train. In total of fifteen pulses were delivered as 5 groups. The gap between each group was 3 ms.	95

4.3	An example of electrographic recording by a fiber probe implanted in the hippocampus of KA injected mouse is shown. Various stages of mouse behavior before, during and after convulsive seizure are identified in red rectangles and the corresponding magnified traces are depicted below: baseline (non-ambulatory physiological stage), pre-ictal spiking (periodic electrographic discharges before or during seizure initiation), seizure (high frequency spikings during fully generalized tonic-clonic seizure), post-ictal spiking (periodic electrographic discharges immediately after seizure), and post-ictal suppression (behavioral arrest following convulsive seizure).	99
4.4	Gliosis in the hippocampus following Intrahippocampal administration of KA. Brain slice with thickness of 100 μm was stained by anti-GFAP to visualize the astrocyte distribution.	100
4.5	Representative EEG recording of 30 minutes experiment session. a. Stimulation group: KA injected mice received 2 minutes of low-frequency (0.5 Hz) photoacoustic stimulation at the session beginning. b. Control group: The spontaneous epileptic activity of KA injected mice. No external stimulation was provided.	101

List of Abbreviations

AAV	Adeno-associated Virus
AMD	Age-related Macular Degeneration
BDNF	Brain-derived Neurotrophic Factor
CNT	Carbon Nanotube
DRE	Drug-resistant Epilepsy
DRG	Dorsal Root Ganglia
FOE	Fiber-based Optoacoustic Emitter
LFP	Local Field Potential
mFOE	Multifunctional Fiber-based Optoacoustic Emitter
NGF	Nerve Growth Factor
NIR	Near-infrared
NIR-II	Second Near-infrared Window
PA	Photoacoustic
PDMS	Polydimethylsiloxane
RRDs	Retinal Regenerative Diseases
tDCS	Transcranial Direct Current Stimulation
TFOE	Tapered Fiber-based Optoacoustic Emitter
TLE	Temporal Lobe Epilepsy
TMS	Transcranial Magnetic Stimulation
TPU	Transcranial Pulsed Ultrasound
WT	Wild Type

Chapter 1

Introduction

1.1 Introduction to neuromodulation techniques

Within the 1.3-liter of the human brain, billions of neurons form a heterogeneous network that communicate with each other through electrical, chemical and physical signals. (Kandel et al., 2000) Understanding this complex information transfer process is one of the most urgent needs in the biomedical community. Solely in the United States, disease of nervous system, including but not limited to Alzheimer's disease, epilepsy, low back pain, spinal cord injury and Parkinson's disease, affect more than 100 million patients and generate nearly 800 billion dollars and is still rapidly rising due to the aging of the U.S. population. (Gooch et al., 2017) Neuromodulation is a technique that can artificially influence or modulate the activity of the target neurons. It's an inevitable tool in both the neuroscience study but also the clinical treatment of neurological diseases. It's importance and applicable fields can be understood from three perspectives:

1. Neuromodulation plays a crucial role in the fundamental study of neuroscience, enabling researchers to investigate the dynamics of neural circuits and animal behaviors. By combining neuromodulation techniques with specific recording technologies, scientists can repeatedly study the responses elicited by stimulating individual neurons or specific volumes within the brain.
2. Neuromodulation has emerged as a promising approach for the treat neurolog-

ical diseases. Unlike conventional pharmacotherapy, which lacks specificity and often leads to side effects, neuromodulation offers targeted, adjustable, and reversible therapeutic interventions. It has demonstrated its efficacy in treating movement disorders like Parkinson’s disease and essential tremor. It is increasingly being examined for its therapeutic potential across a range of neurological disorders, such as neuropathic pain and epilepsy. (Harmsen et al., 2020)

3. Neuromodulation facilitates the integration of input function to the brain machine interface and prosthesis devices. For instance, cochlear and retinal prostheses have the ability to restore auditory (Zeng et al., 2008) and visual sensory functions (Bloch et al., 2019) in patients, respectively. Similarly, limb prostheses can restore the sense of touch.

1.2 Current available neuromodulation methods

Since the weak current stimulating neural activities was observed in the early 19th century, a variety of neuromodulation techniques have been developed. The signature characteristic of the neuronal activity is a millisecond-long 80-100 mV spikes in the membrane potential, called action potential. (Kandel et al., 2000) Because of the intrinsic voltage-sensitive ion channels, action potentials propagate along the neuronal membrane and trigger the downstream chemical signaling pathway, which releases the neurotransmitters in the synaptic gap. Once the neurotransmitter bind to the postsynaptic terminal, it will active the receptors on the membrane and induce the signal transduction. Beside the electrical and chemical signals, nerve system is able to respond to other physical stimuli, such as temperature (Patapoutian et al., 2003), mechanical force (Delmas et al., 2011), pH (Wemmie et al., 2013) and etc. Therefore, based on those properties, researchers developed corresponding methods to modulate neural activities. In general, an ideal method should be able to modu-

late neural activities with a high spatial, temporal and functionality specificity but without biocompatibility and reliability issues even in long term. (Lewis et al., 2016; Chen et al., 2017)

1.2.1 Electrical stimulation

Electrical stimulation is the most common method to alternate the neural activities. It initiates a functional response by depolarizing the membranes of excitable neurons cells. As Hodgkin and Huxley described in their original paper, the action potentials of neurons are driven by the ionic flow across the cell membrane. (Hodgkin and Huxley, 1952) Similarly, the electrical stimulation is achieved by the flow of ionic current between electrodes, specifically which is in close proximity to the target tissue. (Cogan, 2008) Therefore, there are three fundamental factors of electrical stimulation affecting the stimulation effect: (1) the current delivered by the stimulation electrode; (2) the electrical properties of the target neural tissue; and (3) the electrical properties of electrode–tissue interface. In the past decades, from the electrode design to the charge injection waveform, numerous efforts have been made to improve the performance of electrical stimulation in clinical applications. Up to date, it has been applied in clinical disease treatments, including Parkinson’s disease, essential tremor and epilepsy. (Cogan, 2008) However, the intrinsic physical properties of electrical stimulation limit its spatial precision when target specific volume and introduce artifacts in simultaneous electrophysiology recordings. In addition, the electrical stimulation usually is invasive because of the electrode placement. This implantation procedure carry associated risks like infection and complications in clinical applications. And the mechanical and chemical mismatch between electrode made of hard materials (usually metals and semiconductors) often yields a foreign body response and gliosis in neighboring neural tissue, which is one of the reasons of treatment effect variation. (Frank et al., 2019)

1.2.2 Ultrasound stimulation

More than 90 years ago, it has been first observed that sound wave is capable of stimulating the contraction of frog's muscle. (Harvey, 1929) Different with the electrical neuromodulation, ultrasound stimulation usually is a non-invasive method to enhance or suppress the neural activities. In a typical ultrasound stimulation, acoustic wave with frequency above 20 kHz (exceeds the hearing range of human) is generated by the ultrasound transducer and delivered transcranially to the brain tissue. (Tufail et al., 2011) Multiple parameters, including frequency, intensity, pulse length, repetition frequency and etc., determine the characteristics of the ultrasound wave used in neuromodulation. In the past decades, the ability of ultrasound wave in neuromodulation has been demonstrated across a wide range of stimulation patterns in a variety of experimental settings. With the development of ultrasound engineering, the focused ultrasound technique can deliver acoustic wave to a particular location and further pushes the spatial resolution to the order of the wavelength of the driving frequency. For example, Tufail et al. showed the transcranial pulsed ultrasound (TPU) can functionally stimulate mouse brain circuits without requiring surgery or genetic modification, while conferring a spatial resolution of 3 mm. (Tufail et al., 2010) Therapeutic applications of ultrasound in brain, like ablation therapies, has been developed and applied in clinical scenarios. (Hynynen and Clement, 2007) However, using it for neuroscience and neurological disorders are still at initial stage. There is a need for neuroscientists to further study the bioeffects of ultrasound in brain physiology and the mechanism of ultrasound in neuromodulation. Currently, multiple hypotheses have been proposed, such as the micropore formation (Krasovitski et al., 2011) and cavitations and mechanosensitive ion channels (Yoo et al., 2022), but the conclusion is still unclear. If the future studies demonstrate its usefulness and safety in neuromodulation, it will eliminate the surgery implantation of electrodes

used by current electrical based brain stimulation. (Tyler, 2011)

1.2.3 Optogenetics

The desire toward a neuromodulation technique with both high-temporal and cellular precision remains within the field of neuroscience and neuroengineering. Compared with electrical field and acoustic wave, light is an ideal medium for precision control of neural activities. A light spot smaller than the single neuron can be easily achieved through modern optics. Optogenetics was developed for fast, specific excitation or inhibition within systems as complex as freely moving mammals. (Fenno et al., 2011) Optogenetics control the neural activities through the light-sensitive microbial opsins. For the opsins controlling inward cation currents, their expression in neurons are used to depolarize the neuronal membrane under the light exposure. Similarly, for those optical pump of chloride ions, the outward currents and hyperpolarization will inhibit spikes. Besides the development of opsins, delivering tools also plays critical role in the application of optogenetics in neural engineering. Viral expression system has the advantage of fast, versatile and high effective copy for robust expression level. Especially, the adeno-associated viral (AAV) vectors have been used successfully to introduce opsins into the mouse, rat, and primate brain. (Zhang et al., 2010) Although the AAV delivering system is successful and widely used in experimental study, the virus delivery is still an obstacle for its application in clinical settings, because of its invasiveness, potential off-target and ethical considerations. Currently, a significant application of optogenetics is to identify the clinically relevant target for conventional treatments, like drug and electrical stimulation. This cellular-level activation or silencing makes the screening process more precise than other study methods. (Chow and Boyden, 2013) But the direct usage of optogenetics in clinical treatment is still at early stage. For example, one Phase I/II clinical trial of optogenetics for vision restoration is registered and underway in North America at

the Retina Foundation of the Southwest (ClinicalTrials.gov identifier NCT02556736, sponsor Allergan). (Simunovic et al., 2019) Once the effectiveness and safety have been demonstrated, optogenetics has potential for the clinical therapeutic treatment in more and more neurological diseases.

1.2.4 Photothermal neuromodulation

Photothermal is another light-mediated technique that use light and heat to regulate the neural activities in the brain or other parts of nervous system. It's a genetic-free approach that also offers the spatially precise control over neural circuits leveraging the physical properties of light. The process of photothermal neuromodulation typically involves the use of nanoparticles that can absorb light and convert it into heat. These nanoparticles, such as gold (Au), silicon (Si), Mxene, and graphene-based nanoparticles are engineered to improve the light-heat conversion efficiency and bind to the neurons of interest. (Carvalho-de Souza et al., 2015; Rastogi et al., 2020; Jiang et al., 2016b; Wang et al., 2021) When illuminated with light of a specific wavelength, the nanoparticles rapidly heat up, causing localized temperature changes in the surrounding tissue. The induction of temperature elevation or a temperature gradient is the main contributor for the modulation effect. Two potential mechanisms are proposed in previous studies. One is the displacement current cross the membrane by changing the membrane capacitance *via* rapid localized temperature variations, *i.e.*, *via* the 'optocapacitive' effect. (Shapiro et al., 2012) Another theory is that the temperature change can stimulate the temperature-sensitive channels. These ion channels, such as TRP channel family (TRPV1, TRPV2, TRPV3 and TRPM8), are activated when the temperature fluctuation reaches certain threshold. (McKemy et al., 2002; Peier et al., 2002) Then the change of ion conductance upon activation of temperature-sensitive ion channels modulates the electrical activity of the cell membrane. (Karatum et al., 2023) Instead of the gene delivery, the largest concern

for photothermal modulation is the thermotoxicity to the nerve tissue. Until today, to the best of my knowledge, there were no specific clinical trials on photothermal neuromodulation registered on public records.

1.3 Development in photoacoustic neuromodulation methods

Both optogenetics and photothermal neuromodulation techniques leverage the physical properties of light to achieve the high spatial resolution but are limited by the concern on gene transfection and thermotoxicity. Photoacoustic, also known as optoacoustic, is also a light-mediated effect and has been discovered about 150 years ago. (Bell, 1880) It was discovered by Alexander Graham Bell that an acoustic signal was produced when a sample in an enclosed cell was shined by a periodic light (i.e. chopped light) and could be heard by means of a hearing tube attached to the cell as shown in Figure 1.1. (Rosencwaig and Gersho, 1976) Photoacoustic effect with gas was well-established for the gas analysis. However, photoacoustic with solid was ignored for over 90 years after the discovery. From 1990s, there was a growing interest in the application of the photoacoustic effect in biomedical imaging. Short laser pulses are used to generate the megahertz ultrasound waves through photoacoustic effect in biological tissues. Such non-ionizing waves pose no health hazard compared with conventional X-ray imaging. At the same time, the photoacoustic imaging provides higher contrast and spatial resolution than the pure ultrasound imaging, since the ultrasound only detects the mechanical properties in biological tissue. (Xu and Wang, 2006) Following the similar idea, photoacoustic wave were proposed for precise neuromodulation recently. (Jiang et al., 2020b; Shi et al., 2021; Jiang et al., 2021) Ultrasound waves are generated locally and defined by the light spot. Theoretically, it can achieve the similar spatial resolution compared with the optogenetics and pho-

tothermal neuromodulation but without the gene transfection and thermotoxicity.

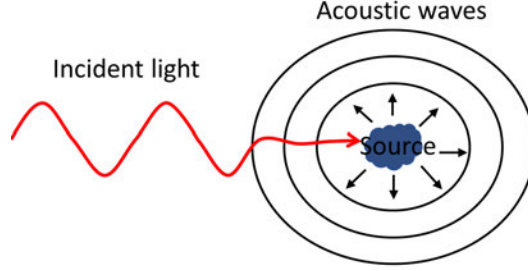


Figure 1.1: The schematic of the photoacoustic effect. A ultrasound wave is generated from the enclosed cell under the chopped light.

1.3.1 The principle of photoacoustic neuromodulation

Photoacoustic neuromodulation is a way to stimulate neural activities benefiting from the mechanical stimuli from ultrasound as well as the photons with high spatial precision. (Shi et al., 2022) The general optoacoustic equation for wave generation and propagation in an inviscid medium has been described (Wang and Wu, 2012) as:

$$\left(\nabla^2 - \frac{1}{v_s^2} \frac{\partial^2}{\partial t^2} \right) p(\vec{r}, t) = -\frac{\beta}{k v_s^2} \frac{\partial^2 T(\vec{r}, t)}{\partial t^2} \quad (1.1)$$

where $p(\vec{r}, t)$ is the acoustic pressure at location r and time t , T is the temperature rise, v_s is compressibility, which can be expressed as:

$$k = \frac{C_P}{\rho v_s^2 C_V} \quad (1.2)$$

Here, ρ is the mass density, C_P and C_V are the specific heat capacities at constant pressure and volume, respectively. The left part of Eq.(1.1) describes the wave propagation, whereas the right-hand side represents the wave generation term.

For effective photoacoustic generation, laser duration should be less than two confinements, *i.e.*, thermal confinement and stress confinement. (Zhigilei and Garrison, 2000) Meeting the thermal confinement means that thermal diffusion during laser

illumination can be neglected:

$$\tau_{th} = \frac{d_c^2}{\alpha_{th}} \quad (1.3)$$

where α_{th} is the thermal diffusivity (m^2/s) and d_c is the characteristic dimension of the heated region (m). The stress confinement means how fast the mechanical pressure propagates in during the acoustic generation process, which is defined by the stress relaxation time and estimated as:

$$\tau_s = \frac{d_c}{v_s} \quad (1.4)$$

where v_s is the speed of sound in the sample. When both criterion are met, it means propagation of both heat and mechanical stress are limited within the illumination region or the propagation is negligible during the laser excitation. Regarding those criterion, a fast laser, such as picosecond or nanosecond pulse laser is required for the generation of thermoelastic pressure.

1.3.2 Fiber-based optoacoustic emitter

Sharing the same mechanism, photoacoustic wave can be generated through the emitter designed in different forms. Fiber-based photoacoustic emitter (FOE) is a miniaturized point source to generate ultrasound using the photoacoustic effect. The optical fiber is utilized to guide the input laser pulse and a thin layer or multiple layers of photoacoustic material are attached to the fiber tip to convert the laser energy into acoustic wave. (Figure 1-2) Previously, such highly miniaturized ultrasound generator has been developed and applied in the biomedical field for drug delivery, (Shi et al., 2020) ultrasound imaging (Alles et al., 2016) or being integrated into clinical devices such as catheters or needles to provide real-time guidance during surgery. (Ansari et al., 2018) The first time that photoacoustic effect was applied in neuro-modulation was done by Jiang et al. through a FOE. (Jiang et al., 2020b) In this

work, Jiang et al. showed that the FOE with a total diameter of 600 μm generates an acoustic wave and was capable of direct neuron stimulation with sub-millimeter resolution *in vitro* and *in vivo*. An unique feature of FOE developed in this work is the two-layers photoacoustic emitter. The first layer is the light diffusion layer consisted of ZnO/epoxy and the second layer is the light absorption layer made of graphite/epoxy. This design allows the FOE to produce the fast decay omnidirectional ultrasound and such localized pressure achieved neurostimulation with about 500 μm spatial precision in rat primary cortical neurons, confirmed by calcium imaging. The successful neuromodulation was also demonstrated in the animal model. The *in vivo* electrophysiology measurement recorded the local field potential (LFP) in mice cortex when FOE was placed and functioning nearby. Importantly, the FOE stimulation at primary somatosensory cortex only induced localized LFP responses at the stimulation site with no response in the contralateral auditory cortex, which showed direct neural activation without the involvement of auditory pathway. For the study of conventional ultrasound neuromodulation, the auditory pathway was hard to bypass in the animal experiment due to the bulky ultrasound transducer. In addition, the FOE stimulation on mice motor cortex also successfully induced the response of forelimb muscle, which demonstrated its effectiveness in controlling the animal behavior.

1.3.3 Tapered fiber-based photoacoustic emitter

Based on the concept of FOE, Shi et al. continued to improve the performance of FOE, especially on its spatial resolution by miniaturizing the size of emitter. (Shi et al., 2021) Through fiber tapering technique, the size of photoacoustic emitter of FOE was further reduced to 20 μm and the mixture of carbon nanotube (CNT) and polydimethylsiloxane (PDMS) was used as a more efficient photoacoustic material. This tapered fiber-based photoacoustic emitter (TFOE) generates the acoustic wave

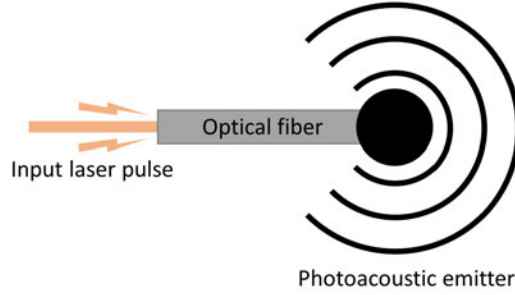


Figure 1.2: The schematic of a fiber-based photoacoustic emitter (FOE). The input laser is guided by the optical fiber and entering the photoacoustic emitter at the tip of FOE. Then the laser energy is converted into a point source ultrasound wave.

with a pressure of 2.7 MPa and shows an attenuation to $1/e$ at a characteristic distance of $39.6 \mu\text{m}$, allowing single cell stimulation and subcellular stimulation of axons and dendrites. Another improvement was that the TFOE was capable of stimulating neuron using single acoustic wave induced by single laser pulse. This single pulse stimulation was much shorter than reported ultrasound neuromodulation using piezo-based acoustic transducer, which usually requires tens or hundreds of milliseconds of acoustic wave. (Tufail et al., 2011) In neuroscience study, patch clamp is the gold standard to investigate the activities of neurons. Because it requires a stable seal between the patch and target neuron, conventional ultrasound transducer often disrupts the recording due to the large acoustic field. However, the TFOE generates a near-field acoustic wave offering minimal disturbance and a stable patch condition. The electrophysiology recording has been simultaneously achieved during TFOE single neuron stimulation using whole cell patch clamp performed in brain slices. (Shi et al., 2021) As a genetic-free, high spatial resolution neuromodulation technique, TFOE provides a new way to investigate the mechanism of neural stimulation and behavior of neural circuits.

1.3.4 Semiconductor photoacoustic nanoparticles

Nanomaterials are desired for biomedical applications because they are minimally invasive, cost-effective, and biocompatible compared to conventional implantable devices. (Knoben et al., 2022) It has been developed to working with multiple types of stimuli, such as light, (Nakatsuji et al., 2015; Carvalho-de Souza et al., 2015; Maya-Vetencourt et al., 2020; Chen et al., 2018a) magnetic, (Chen et al., 2015; Huang et al., 2010) and ultrasound. (Cafarelli et al., 2021; Marino et al., 2015) Recent years, the photoacoustic nanoparticle for neuromodulation has also been developed using a new class of nanoparticles, semiconductor polymer nanoparticles. (Jiang et al., 2021) It has a unique property that can absorb the light in the near-infrared (NIR) region. In this study, Jiang et al. demonstrated that photoacoustic nanotransducers (PAN) with size of 50 nm can generate robust acoustic signal with a peak pressure of 1.36 kPa upon nanosecond laser excitation at 1030 nm. Through a non-specific charge-charge interaction, PAN bind to the neuronal membrane by coculturing for 15 minutes. The bound PAN was able to induce the neuronal activation under laser illumination through photoacoustic effect and confirmed by calcium imaging of GCaMP expressing rat cortical neurons. Also, its functionality has been demonstrated in the animal model. Both the LFP and muscle response were observed in the mice with PAN injected. Because of the deep penetration depth, PAN has the potential for deep brain stimulation with NIR light through optoacoustic effect. It opens new opportunities for genetic-free and noninvasive neuromodulation with high spatial temporal resolution.

1.4 Summary

Recently, the photoacoustic effect was demonstrated could be a new way to modulate neural activities.(Jiang et al., 2020b; Jiang et al., 2021; Shi et al., 2021) In the past

decades, lots of progresses have been made on photoacoustic biomedical imaging. But as a neuromodulation method, photoacoustic is a relatively new technique. Compared with existing technique, such as electrical stimulation, optogenetics, photothermal neuromodulation, transcranial direct current stimulation (tDCS), transcranial magnetic stimulation (TMS) and etc., it's a light-mediated technique, which can achieve high spatial and temporal resolution without genetic transfection. (Figure 1·3)

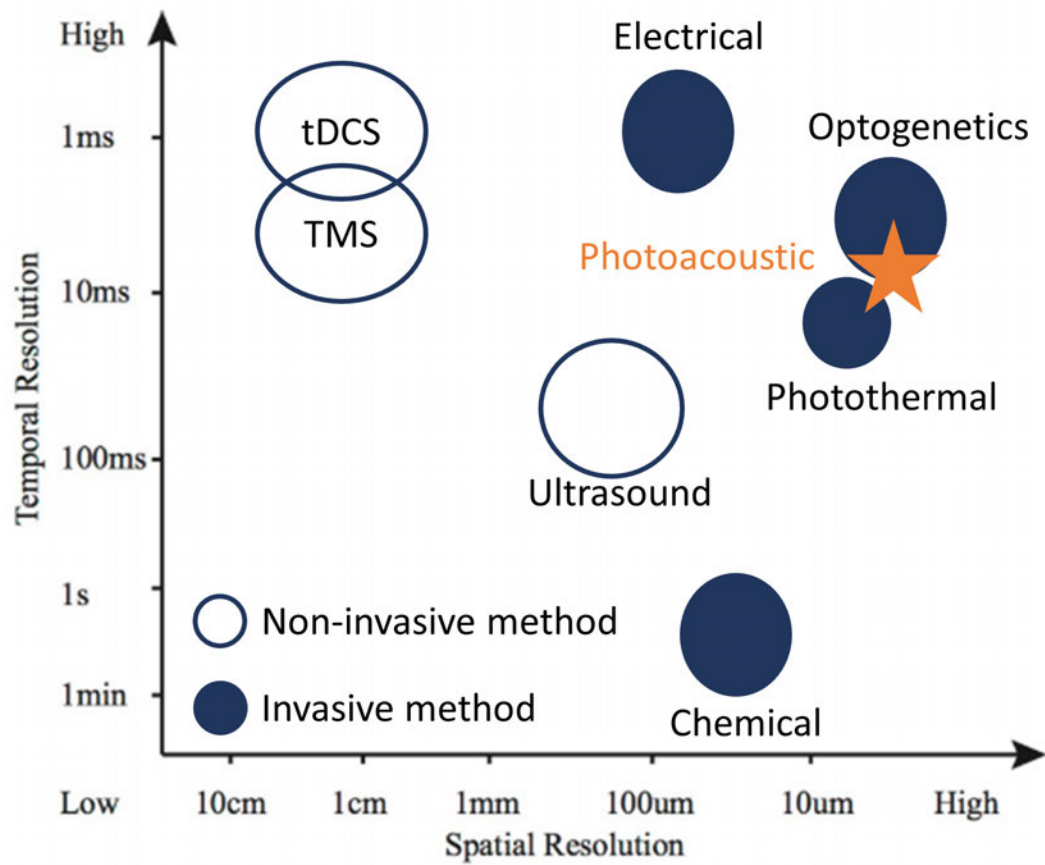


Figure 1·3: Spatio-temporal resolution of various neuromodulation methods. The open circle represents non-invasive methods and the black dots invasive methods. Photoacoustic neuromodulation can achieve a spatiotemporal resolution similar to optogenetics but is genetic-free.

In these previous works, (Jiang et al., 2020b; Jiang et al., 2021; Shi et al., 2021) research more focused on a tool for neuroscience rather than neurological disease

treatment. And there are several gaps need to be filled to further expand its applications. One is the material mismatch. Different form of neural interface is required for different target region. For example, for brain cortex, a soft film is preferred to enable conformal contact with the curved brain surface. For peripheral nerve, like sciatic nerve, a roll or a cuff structure is better. Also, when move forward to the in vivo application, the foreign body response has to be considered. Another gap is that more function is needed, for example the capability of simultaneous recording. Therefore, my research focused on the design and development of two new types of photoacoustic materials to expand the use of photoacoustic stimulation into more applications. One is a soft hydrogel film. And another is a multifunctional fiber-based emitter. The study based on these materials increased our knowledge to photoacoustic neurostimulation, also help us to investigate the effect of photoacoustic neuromodulation in the neurological and neurodegenerative diseases treatment.

Chapter 2

Photoacoustic Carbon Nanotubes Embedded Silk Scaffolds for Neural Stimulation and Regeneration

2.1 Introduction

In tissue engineering, scaffolds offer multiple synergistic functions for regeneration, including providing support for cell adhesion, structural support for the tissue, and facilitating mass transport of nutrients and growth factors, while also being biocompatible. For neural tissue, biophysical and biochemical stimulation leveraging the innate ability of neural tissue to react to stimuli is an additional key strategy to improve neurite outgrowth and promote functional regeneration. (Lavrador et al., 2021) Approaches to functionalize nerve scaffolds include physical stimulation, through electrically conductive scaffolds, (Chen et al., 2018b; Li et al., 2013) mechanical cues, (Huang et al., 2018; Zhu et al., 2020) and chemical stimulation, through drug and growth factor release. (Lee et al., 2003; Li et al., 2018)

By modulating neuronal activities, neural stimulation techniques like optogenetics, (Park et al., 2015a) electrical (Al-Majed et al., 2000b; Al-Majed et al., 2000a) and ultrasound stimulation, (Han et al., 2020; Jiang et al., 2016a) encourage nerve regeneration. Electrical stimulation is the most widely applied neural stimulation technique to promote nerve regeneration. For example, applying an external electric field for 1 hour at 20 Hz in vitro significantly promoted axon regeneration after nerve transec-

tion and microsurgical repair. (Geremia et al., 2007) Conventional transducer based ultrasound treatment can be non-invasive but has limited spatial resolution. Optogenetics promoted neurite outgrowth with high spatial precision and in a cell-specific manner. (Park et al., 2015a) However, this approach requires viral transfection which makes human applications challenging.

While the electrical field or currents can be applied through ionically conductive tissue fluid environment, a more efficient and controllable delivery requires electrically conductive neural scaffold. (Hiltunen et al., 2016) These scaffolds showed improved performance in promoting nerve regeneration, including conductive polymers (Xu et al., 2014; Molino et al., 2018; Zou et al., 2016) and carbon-based materials.(Chen et al., 2018b; Xu et al., 2020) However, in clinical applications, the delivery of electrical stimulation to conductive scaffolds remains challenging. Current solutions are limited to stimulation within the intraoperative time frame, or transcutaneous stimulation after surgery. Multiple postoperative stimulations are important for enhanced neuron regeneration and functional recovery, (Koo et al., 2018) but require the use of transcutaneous wires, and therefore an increased risk of infection. To overcome the significant limitations, wireless (Koo et al., 2018; Choi et al., 2020) and self-powered (Liu et al., 2020) electronics systems were developed and demonstrated enhanced neural regeneration as a result of multiple episode stimulations. However, the intrinsic property of electrical current applied for stimulation can lead to a current spread beyond the injury site to healthy tissues, with undesirable impacts.

Recently, photoacoustic (PA) stimulation has been shown as a non-genetic and high-precision method for neural stimulation.(Jiang et al., 2020b; Jiang et al., 2021) In a photoacoustic process, pulsed light is delivered into absorbers, generating acoustic waves at ultrasonic frequencies. (Tam, 1986) Photoacoustic polymer nanoparticles, upon excitation by pulsed light in the second near-IR window (NIR-II), activate

primary neurons in culture with single-neuron precision.(Jiang et al., 2021) Optical fibers with a photoacoustic coating composed of graphite mixed with epoxy, or carbon nanotubes mixed with PDMS, provide sub-millimeter photoacoustic stimulation in vitro and in vivo.(Jiang et al., 2021) We here hypothesize that introducing highly efficient absorbers like carbon nanotubes into a biocompatible material, through a nanocomposite approach, would enable PA stimulation in biomaterials used for scaffolds. As a light-mediated non-genetic method, neural scaffolds with PA stimulation capabilities could promote neurite outgrowth as an alternative to electrical stimulation and optogenetics, without the requirement of transcutaneous wire connections or viral transfection.

In this work, we report a biocompatible silk fibroin (silk) scaffold with PA capabilities, enabling neural stimulation and promoting neurite outgrowth. We introduced CNTs into silk using a nanocomposite approach. The silk matrix in the CNT/Silk material provides structural support for tissue growth. The embedded CNTs absorb the pulsed NIR-II light and transduce light energy to acoustic, which activates neurons cultured on the CNT/Silk to promote neural outgrowth. We chose silk fibroin as a matrix material. As a natural polymer derived from silkworm, silk fibroin is an FDA-approved biocompatible material, (Bettinger et al., 2007) and its abilities in supporting neural adhesion and preserving neural functions have been confirmed previously. (Benfenati et al., 2012; Shi et al., 2019) In addition, silk fibroin provides a controllable rate of biodegradation, (Cao and Wang, 2009) tunable drug-loading capabilities, (Pritchard and Kaplan, 2011) and tunable mechanical properties, (Mandal et al., 2012) all of which are important for neural scaffolds. CNTs provide high PA-conversion efficiency and strong absorption in NIR-II, (Won Baac et al., 2010) which provides potential for tissue penetration.

Unlike our previous report on fiber-based PA devices, the scaffold approach de-

scribed here in film or 3D structure formats, offers implant materials for neural stimulation and enhanced regeneration. PA stimulation achieved upon the excitation of the NIR light offers potential non-invasive neural stimulation and thus regeneration. In addition, compared with reported stimulation work on nanoparticles upon NIR excitation, the scaffold approach allows the embedded nanoparticle transducers (i.e. CNT) functioning at the implanted target site, which avoids the difficulty of controlling the fate of injected nanoparticles. (Benfenati and Lanzani, 2021) Our approach suggests a new neural interface based on PA biomaterials and highlights the efficacy of PA stimulation for regeneration.

2.2 Materials and Methods

2.2.1 Preparation of Silk and Functionalized CNT

The silk fibroin solution used for the silk roll fabrication was prepared using published protocols. (Rockwood et al., 2011) Briefly, pieces of *Bombyx mori* cocoons were boiled in 0.02 M aqueous Na_2CO_3 for 30 min. The degummed silk was extensively rinsed in distilled water, dried overnight, and dissolved in 9.3 M LiBr at 60°C for 4 h. The silk/LiBr solution was dialyzed against distilled water for 2 d with ten changes of water. The solution was centrifuged at 9,000 rpm for 2×20 min. For the subsequent silk roll fabrication, the silk concentration was determined using an analytical balance by evaporating water from a solution of known weight and weighing the remaining solid.

Multiwall CNT (< 8 nm OD, 2–5 nm ID, Length 0.5–2 μm , VWR Inc., NY, USA) aqueous solution (2 mg mL^{-1}) and DSPE-PEG 2000 (88120, Avanti Polar Lipids, AL, USA) aqueous solution (5 mg mL^{-1}) were mixed at a volume ratio of 1:2 and sonicated 3 hours in a bath sonicator at room temperature. Unfunctionalized CNT was first removed by centrifugation at 10k and 12k rpm for 10 minutes twice, respectively.

Then the unbound surfactant was thoroughly removed by repeated filtration through 100 kDa filters (Vivaspin 6, Sartorius) at 3.5k rpm for 3×10 min. The concentration was determined by the absorbance at 500 nm of a diluted sample compared with the standard curve.

2.2.2 Fabrication of CNT/Silk Film and CNT/Silk Roll Scaffolds

The CNT/Silk films were fabricated on a glass substrate by drop-casting 125 μL premixed silk (2%) and CNT (0-100 $\mu\text{g mL}^{-1}$) solution per cm^2 and then immersed in an 80% methanol solution to ensure insolubility. The CNT/Silk roll scaffold was fabricated by a bilayer structure following our previously reported method. (Huang et al., 2020) A bilayer film was first fabricated on a cover glass by drop-casting 41.67 μL agarose solution (%) per cm^2 and 125 μL premixed silk (2%) and CNT (0-100 $\mu\text{g mL}^{-1}$) solution per cm^2 sequentially. After drying, the agarose/silk bilayer film was cut to desired size and aspect ratios. After immersion in 80% methanol solution, the self-folding CNT/Silk rolls were achieved by peeling the bilayer film off the glass substrate and immersing in water. All scaffolds were disinfected with 70% ethanol and UV light overnight.

2.2.3 Characterization of CNT/Silk scaffolds

For generating PA, a 1030 nm Q-switch laser with a pulse width of 3 ns was delivered to the scaffold through a multimodal optical fiber with 200 μm core diameter (Thorlabs Inc.). An ultrasound transducer (10 MHz, XMS-310-B, Olympus, MA) with a preamplifier (0.2–40 MHz, 40 dB gain, Model 5678, Olympus, USA) was utilized to detect the acoustic waves. A digital oscilloscope (DSO6014A, Agilent Technologies, CA) was used to display and record the converted electrical signals from the transducer. The scaffold and ultrasound transducer were both immersed in deionized water to reduce the loss during the wave propagation and mimic the real application environ-

ment. The thermal effect generated by the scaffold was characterized by monitoring the change of surface temperature of scaffold in dry state. Thermal camera (A400, FLIR® Systems, Inc.) and thermal probe (DI-245, DATAQ Instruments, Inc., OH) were used to measure the temperature change.

Uniaxial tensile testing of silk films were performed on an Instron 3366 testing frame equipped with a 100 N capacity load cell and screw side action tensile grips. Dog-bone shaped silk film samples were obtained by casting the silk solution – loaded or not with carbon nanotubes – into a mold, obtained by fused deposition modeling of polylactic acid, and 3D printed on a Creator Pro 3D printer (Flashforge, China). The films were left to dry, water-annealed as previously described, (Hu et al., 2011) and subsequently hydrated in phosphate-buffered saline (PBS) prior to testing. For tensile testing, a crosshead extension rate of 2 mm/min was used. The Young’s modulus and ultimate tensile strength were obtained from the stress/strain plots.

To measure the optical absorbance of the CNT-loaded silk films, 40 μ L of silk solution, loaded with 0, 20 or 40 μ g/mL of CNTs, was deposited in a 96-well plate. The solution was allowed to dry, and the resulting silk films were water-annealed, as previously described. The films were then hydrated in 200 μ L of PBS, and the optical absorbance was determined using a plate reader (Synergy H1 microplate reader (Bio-Tek, USA)). Eight separate wells were measured and averaged, and the range of wavelengths measured was 300 nm to 1000 nm. The average of eight wells containing 200 μ L of PBS alone were used as a blank.

2.2.4 Cortical neuron and dorsal root ganglia (DRG) isolation and culture

All experimental procedures complied with all relevant guidelines and ethical regulations for animal testing and research established and approved by Institutional Animal Care and Use Committee (IACUC) of Boston University (PROTO201800534). Both primary cortical neuron and DRGs were isolated from embryonic day 15 (E15)

Sprague-Dawley rat embryos of either sex (Charles River Laboratories, MA).

To obtain cortical neurons, cortices were dissected and digested in TrypLE Express (Thermofisher scientific). Then the neurons were plated on poly-D-lysine ($50 \mu\text{g mL}^{-1}$, Thermofisher scientific) coated CNT/Silk scaffolds, silk scaffolds or glass. Neurons were first cultured with a seeding medium comprised of 90% Dulbecco's Modified Eagle Medium (Thermofisher scientific) and 10% fetal bovine serum (Thermofisher scientific) and 1% GlutaMAX (Thermofisher scientific), which was then replaced 24h later by a growth medium comprised of Neurobasal Media supplemented with $1 \times$ B27 (Thermofisher scientific), $1 \times$ N2 (Thermofisher scientific) and $1 \times$ GlutaMAX (Thermofisher scientific). AAV9.Syn.Flex.GCaMP6f.WPRE.SV40 virus (Addgene, MA) was added to the cultures at a final concentration of $1 \mu\text{g mL}^{-1}$ at day 5 in culture for GCaMP6f expression. Half of the medium was replaced with fresh growth medium every 3-4 days. Cells cultured in vitro for 10-14 days were used for PA stimulation experiments.

To extract DRGs, the spinal cord was exposed and individual DRG explants were trimmed of nerve roots and additional connective tissue and placed in a container of growth medium comprised of Neurobasal Media supplemented with $1 \times$ B27 (Thermofisher scientific), $1 \times$ N2 (Thermofisher scientific), $1 \times$ GlutaMAX (Thermofisher scientific) and 50 U/mL penicillin/streptomycin (Thermofisher scientific). Scaffold or glass were coated with poly-D-lysine ($50 \mu\text{g mL}^{-1}$, Thermofisher scientific) and laminin ($5 \mu\text{g mL}^{-1}$, Corning) and rinsed with growth medium prior to seeding. DRGs were randomly selected and directly seeded on the scaffold or glass substrate. They were allowed to attach the substrate for 4 hours with 20 μL growth medium for each DRG explant. After 4 hours, DRGs were covered by the growth medium. Half of the medium was replaced with fresh growth medium every 3 days. All DRGs were grown for 48 hours prior to applying PA stimulation and fixed 10 days following

seeding.

2.2.5 MTS Viability Assay

Neuronal cell viability was determined using the 3-(4,5-dimethylthi-azol-2-yl)-5-(3-carboxymethoxyphenyl)-2-(4-sulfophenyl)-2H-tetrazolium reduction assay (MTS assay, Abcam) following the manufacturer’s instructions. Unlike the MTT assay, the colored formazan dye generated in the MTS assay was soluble in cell culture medium. To avoid interference from the color of CNT/Silk scaffolds, the final solution was transferred into a new 96-well plate and the absorbance was measured at a wavelength of 490 nm using a microplate reader (SpectraMax i3x, Molecular Devices).

2.2.6 Histological Analysis

All animal experiments were performed under the guidance and approval of the Institutional Animal Care and Use Committee (IACUC) of Tufts University (protocol number: M2019-121). Ten female FVB/NJ mice aged 10 weeks were randomly separated into 2 groups. Group 1 was euthanized 3 days after implantation, to assess the acute immune response. Group 2 was euthanized 30 days after implantation to assess chronic inflammation. Two small longitudinal incisions (about 0.5-1 cm) were made through the skin of each mouse. Sterile CNT/Silk roll scaffold were inserted in the resulting subcutaneous pouches. The incision was closed with surgical clips. Animals were monitored daily for the first three days after implantation, then weekly until euthanasia.

2.2.7 *In Vitro* Neurostimulation

Cortical neurons/DRGs were cultured on CNT/Silk scaffold. A Q-switched 1030-nm nanosecond laser with repetition rate of 1.7 kHz and the pulse width of 3 ns (Bright Solution, Inc. Calgary Alberta, CA) was delivered through a 200 μ m core diameter

multimodal optical fiber. The fiber position was controlled by a 3-D micromanipulator (Thorlabs, Inc., NJ, USA) to target an area of the scaffold. During the PA stimulation, the fiber was placed 50 μm approximately above the scaffold and the illumination area was calculated to be 0.05 mm^2 . Calcium fluorescence imaging was performed on a lab-built wide-field fluorescence microscope based on an Olympus IX71 microscope frame with a $20\times$ air objective (UPLSAPO20X, 0.75NA, Olympus, MA), illuminated by a 470 nm LED (M470L2, Thorlabs, Inc., NJ) and a dichroic mirror (DMLP505R, Thorlabs, Inc., NJ). Image sequences were acquired with a scientific CMOS camera (Zyla 5.5, Andor) at 20 frames per second. The fluorescence intensities, data analysis and exponential curve fitting were analyzed using ImageJ (Fiji) and Origin 2018.

2.2.8 Extracellular Recording of DRG Explants

Before the extracellular recording, DRG explants were extracted and cultured on CNT/Silk film for five days following the procedure mentioned in above cell culture section. A micro tungsten electrode (Microprobes for Life Science, MD USA) was used as the recording electrode and a stainless-steel wire was placed in the petri dish as the ground electrode. Both electrodes were connected to the headstage (CV7-B, Molecular Devices Corp, CA), then the electrical signal was acquired by the amplifier (MultiClamp 700B, Molecular Devices Corp, CA) and digitizer (Digidata 1550, Molecular Devices Corp, CA) in sequence. For PA stimulation, 1030-nm nanosecond laser with repetition rate of 1.7 kHz and the pulse width of 3 ns (Bright Solution, Inc. Calgary Alberta, CA) was delivered through a 200 μm core diameter multimodal optical fiber.

2.2.9 Sytox Green Nucleus Acid Staining

5 mM SYTOXTM Green Nucleic Acid Stain solution in DMSO (S7020, Thermofisher scientific) was added in the neuron culture dish with a final concentration of 1 μM

10 minutes before the PA stimulation. Fluorescence imaging was performed on the same wide-field fluorescence microscope described above. Before the PA stimulations, the nucleus of dead neuron was already labeled with green fluorescence and those neurons were picked as the positive control group. For the PA stimulated neurons, in situ fluorescence images were captured before and 10 minutes after the stimulations. The fluorescence intensity of stimulated neurons was compared with positive control group to confirm its viability.

2.2.10 Immunocytochemistry

Cortical neurons were fixed at day 7 with 4% (wt.%) paraformaldehyde (Thermofisher scientific) solution in phosphate buffered saline (PBS, Thermofisher scientific) for 20 min and permeabilized with 0.1% Triton X-100 (Sigma) in PBS for 10 min at room temperature. After 1 hour blocking with 5% Bovine Serum Albumin (BSA) in PBS at room temperature, cells were incubated with the primary antibody, 1:200 anti-Tau antibody (TAU-5) for 2 hours. Then cells were incubated with the secondary antibody, 1:500 Alexa Fluor 488 Goat anti-Mouse IgG (ab150113, Abcam) for 1 hour. Lastly, samples were incubated with 1:10,000 DAPI (D9542, Sigma) solution in PBS for 15 min.

DRGs were fixed at day 10 with 4% (Wt.%) paraformaldehyde (Thermofisher scientific) solution in phosphate buffered saline (Thermofisher scientific) for 20 min and permeabilized with 0.1% Triton X-100 (Sigma) in PBS for 10 min at room temperature. After blocking overnight with 2.5% goat serum (Abcam) in PBS at 4°C, DRG samples were incubated with the primary antibody, 1:500 rabbit anti-neurofilament antibody (N4142, Sigma) solution in 2.5% goat serum solution in PBS for 1 hour. Then samples were incubated with the secondary antibody, 1:1000 Alexa Fluor 633 Goat anti-Rabbit IgG (A-21070, Thermofisher scientific) in 2.5% goat serum in PBS for 1 hour. Lastly, samples were incubated with 1:10,000 DAPI (D9542, Sigma) so-

lution in PBS for 15 min.

2.2.11 Confocal Imaging and Image Analysis

Confocal images were acquired by a laser scanning confocal microscope (FV3000, Olympus). The overview images were taken with an air-immersion 10X objective (Olympus) and stitched by ImageJ (Fiji). The detail high magnification images were taken with 20X objective (Olympus). For the analysis of cortical neurons, acquired images were analyzed by ImageJ. Specifically, neurite was first traced (purple in Figure 2-1) through a semi-automated tracing plugin in ImageJ called SNT. Then the total neurite length within a region of interest (ROI) was calculated. The number of neurons was analyzed by manually counting the DAPI-stained nuclei. For the analysis

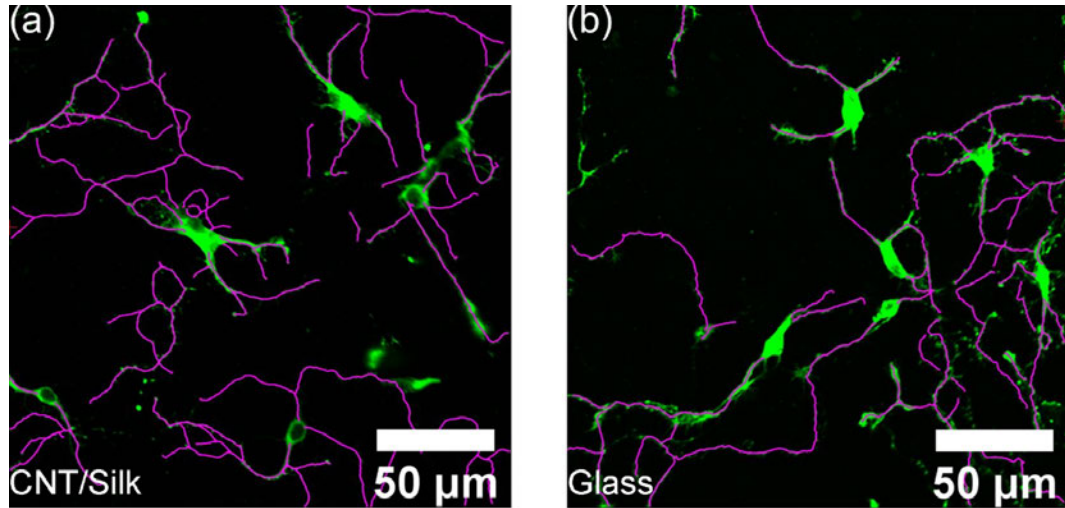


Figure 2-1: Neurite tracing of immunofluorescence images of cortical neurons cultured on CNT/silk film(a) and glass substrate(b). Neurons were labeled with anti-Tau antibody (green).

of DRGs growth, the coverage area of DRGs were calculated by an analysis algorithm written in MATLAB (Mathworks, Natick, MA). The stitched confocal images were firstly converted into a binary image and the boundary of DRGs were marked along 360 radial lines separated by 1° . A polygon was then constructed based on these

boundary points. Finally, the coverage area was derived from the area of the polygon and scale conversion.

2.2.12 ELISA Assay

Cell extractions of PA stimulated DRGs and DRGs in all control groups were collected 24 hours following stimulation by a cell lysis buffer (FNN0011, Thermofisher scientific). The concentrations of brain-derived neurotrophic factor (BDNF) and nerve growth factor (NGF) were measured by the ELISA assay kits (ERBDNF and ERNGF, Thermofisher scientific) following instructions provided. Briefly, experiment samples and standard samples were incubated with pre-coated 96-well plate for 2.5 hours at room temperature. Then biotin conjugate, Streptavidin-HRP, TMB substrate and stop solution were added and incubated successively. Optical absorbance was measured using a microplate reader (SpectraMax i3x, Molecular Devices) at 450 nm, and the concentration was calculated according to the standard curve.

2.2.13 Statistical Analysis

Data shown are mean \pm standard deviation (SD). For the comparison on neurons per area, total neurite length per area and cell viability, one-way ANOVA and Tukey's means comparison test was conducted by using OriginLab. 5 view fields of 0.1013 mm^2 were analyzed for each group. For the comparison on DRG coverage area and the concentration of neurotrophic factors, $N = 5$ samples were analyzed using a one-way ANOVA with Tukey's post-hoc test. P values were determined as: n.s.: non-significant, $p < 0.05$; *: $p < 0.05$; **: $p < 0.01$. Fluorescence images were analyzed using ImageJ (Fiji). Biocompatibility, maximum fluorescence change, DRG coverage area and concentrations of neurotrophic factors were analyzed and plotted using Origin. The coverage area of DRGs were calculated by a custom algorithm in MATLAB.

2.3 Results and Discussion

2.3.1 Fabrication and characterization of CNT/Silk scaffold

The CNT/Silk scaffolds are nanocomposite materials consisting of silk fibroin and CNTs. We functionalized the CNTs with DPSE-PEG2000 (1,2-distearoyl-sn-glycero-3-phosphoethanolamine-N-[methoxy(polyethylene glycol)-2000]) to uniformly disperse the CNT in the silk and to increase the concentration of CNTs in the silk, in order to maximize the light-to-acoustic conversion (Figure 2·2). (Hwang et al., 2013) To

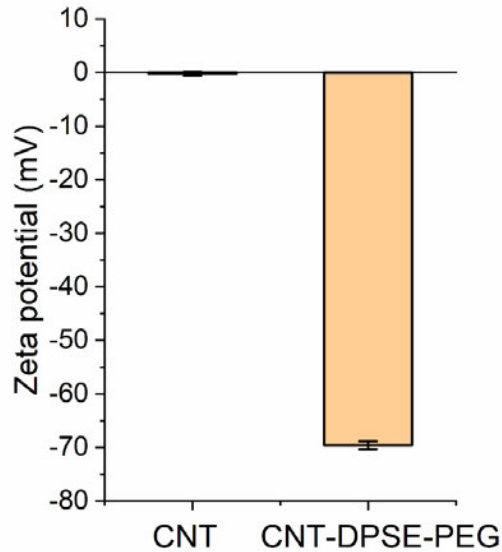


Figure 2·2: The zeta-potential of raw CNT and DPSE-PEG functionalized CNT solution. Negative charges were introduced after functionalization.

prepare the CNT/Silk scaffolds, 20-100 $\mu\text{g/mL}$ of functionalized CNT solution was mixed with 2% (w/v) silk fibroin solution to obtain the solution for casting. The CNT/Silk scaffolds were then prepared through a cast-and-dry method (Figure 2·3) to form films with a typical thickness of $32.54 \pm 1.98 \mu\text{m}$ or a 3D roll structure (Figure 2·4) through the self-folding strategy we have previously reported. All CNT/Silk films used in following experiments were fabricated from solutions of 20 $\mu\text{g/mL}$ func-

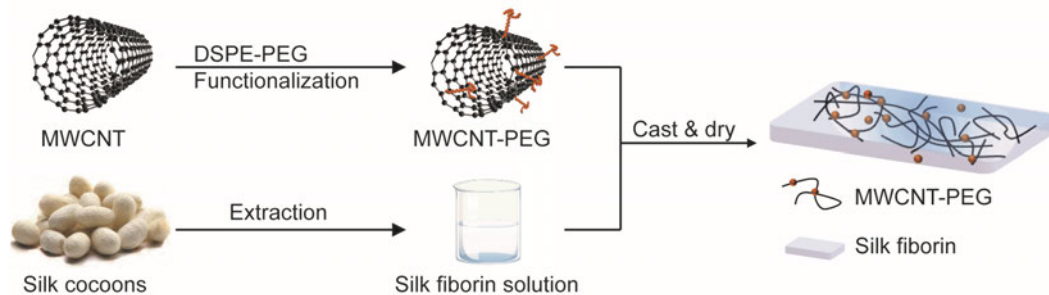


Figure 2.3: Schematic of the fabrication process of CNT/Silk PA films.

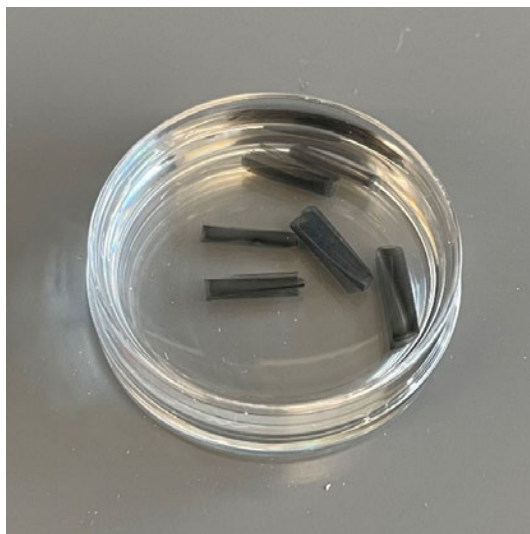


Figure 2.4: The CNT embedded silk roll was fabricated through a self-folding strategy.

tionalized CNT and 2% (w/v) silk fibroin, unless otherwise specified. 20 $\mu\text{g/mL}$ CNT embedded silk film showed a stronger light absorbance than the neat silk film over the UV-VIS-NIR spectrum (Figure 2.5). Also, compared with pure silk film, the tensile modulus and tensile strength of 20 $\mu\text{g/mL}$ CNT/Silk film was improved by 9.7% and 16.9%, respectively (Table 2.1). We quantified the PA signals generated by the CNT/Silk films under pulsed laser illumination. A 1030 nm laser with a pulse width of 3 ns at a 1.7 kHz repetition rate was delivered through a 200 μm core diameter multimodal optical fiber, providing an illumination area of 0.05 mm^2 to the

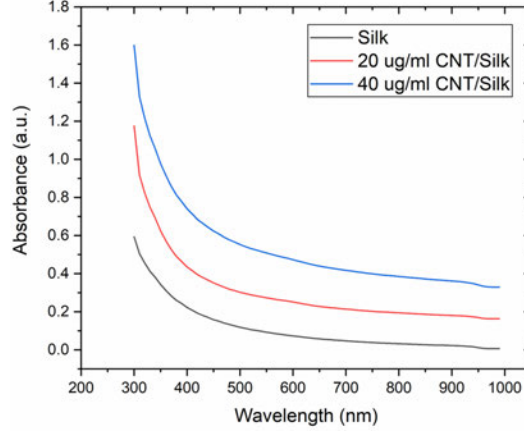


Figure 2.5: Absorption spectrum of silk and CNT/Silk film (20 $\mu\text{g}/\text{ml}$ and 40 $\mu\text{g}/\text{ml}$).

Table 2.1: Mechanical properties of silk and CNT/Silk films.

Film material	Tensile modulus (MPa)	Tensile strength (MPa)
Silk	17.90 ± 2.70	2.78 ± 0.26
20 $\mu\text{g}/\text{ml}$ CNT/Silk	19.64 ± 1.20	3.25 ± 0.38
40 $\mu\text{g}/\text{ml}$ CNT/Silk	21.16 ± 2.21	3.11 ± 0.42

CNT/Silk film. The acoustic waveforms generated were measured by a 10 MHz ultrasound transducer under water. The schematic of the measurement is shown as Figure 2.6a. A representative acoustic wave in the time domain under a single laser pulse is shown in Figure 2.6b. After Fast Fourier Transform (FFT), the PA frequency spectrum exhibited a broad frequency range up to 20 MHz and a peak frequency of 1.2 MHz. This broad frequency band is characteristic of PA signals, compared to narrow frequency bands in ultrasound generated by traditional piezoelectric-based transducers.(Lee et al., 2018) To control the amplitude of the PA signals generated, we varied the concentration of CNTs in the composite, as well as the laser energy, based on the following rationale. According to the basic PA theory, (Kim et al., 1998)

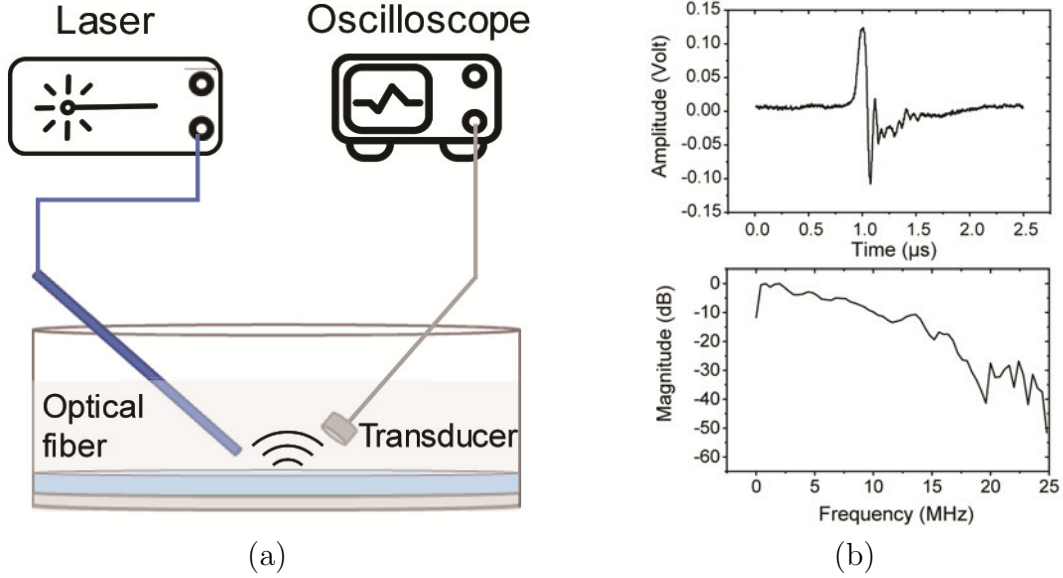


Figure 2.6: Characterization of PA properties of CNT/Silk films.: (a) Schematic of the PA measurement. (b) Acoustic wave generated by a 20 $\mu\text{g/mL}$ CNT/Silk film in time domain and frequency domain measured by a 10 MHz transducer. Laser pulse energy of 74.7 μJ .

the pressure (Pa) is correlated to several factors and can be expressed as:

$$P_0 = \frac{\beta c^2}{C_p} A \frac{F}{l} \quad (2.1)$$

where β is the volumetric thermal-expansion coefficient (K^{-1}), c is the sound speed (ms^{-1}), C_p is the specific heat capacity at constant pressure ($\text{J kg}^{-1} \text{K}^{-1}$), A is the light absorption ($0 < A < 1$, dimensionless), F is the laser fluence (J m^{-2}), and l is the characteristic length (m). Therefore, the amplitude of the PA wave is linearly proportional to the light absorption and input laser energy. We first varied the light absorption of the PA film by changing the concentration of the embedded CNTs (Figure 2.7). The CNT/silk films fabricated from 0, 20, 40, and 80 $\mu\text{g/mL}$ functionalized CNTs and 2% (w/v) silk fibroin were tested with a fixed laser pulse energy of 74.7 μJ . Second, we tested the effect of laser pulse energy. The CNT/silk film with a CNT concentration of 20 $\mu\text{g/mL}$ was used, and the laser pulse energy varied from 22.9 to

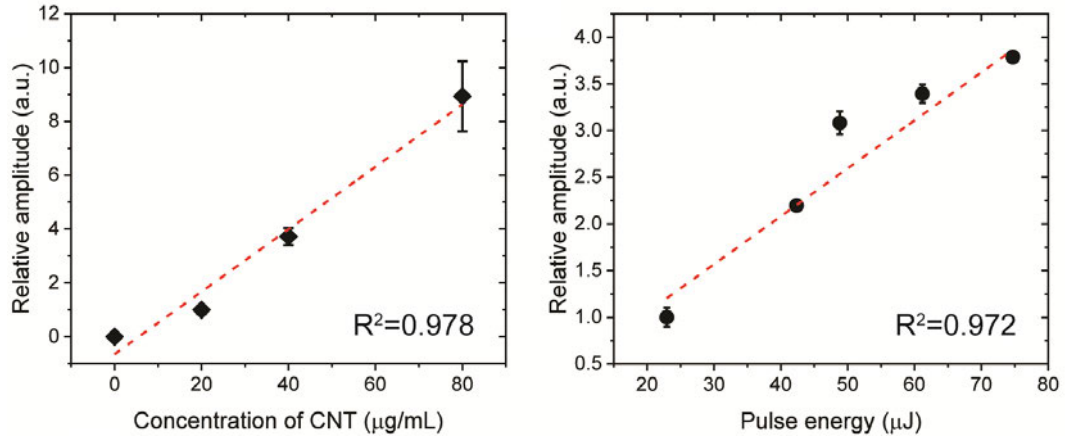


Figure 2-7: Normalized mean peak to peak amplitude of the PA waves as a function of the concentration of CNT (left panel) and laser pulse energy (right panel). Error bar, $n = 3$. Red dotted lines, fitting curves.

74.7 μJ . The higher concentration of embedded CNTs and larger laser pulse energy induced larger amplitudes of PA waves, in a linear fashion (R -square = 0.978 and 0.972, respectively), as expected based on Eq.(2.1). The linear characteristics enabled facile control of the amplitude of PA waves through these two key parameters (CNT concentration and laser pulse energy). It should be noted that a 40 μm needle hydrophone was also used to measure the pressure of the PA waves from the 20 $\mu\text{g/mL}$ CNT/silk film at a pulse energy of 14.7 μJ (corresponding to an energy density of 29.4 mJ/cm^2). The generated PA pressure was 0.185 ± 0.015 MPa, which will be shown below to successfully induce neural stimulation in primary neuron cultures.

The photoacoustic effect is associated with a transient temperature increase. To characterize the thermal increase generated by CNT/Silk scaffolds during the photoacoustic process, the temperature of the CNT/Silk surface of the light illumination area was measured by a thermal camera. The laser pulse energy and repetition rate were fixed at 53 μJ and 1.7 kHz. The laser duration was increased from 3 ms to 100 ms. Figure 2-8 plots the temperature measured as a function of time upon the excitation of a laser pulse train with a duration at 3, 10, 20, 50 and 100 ms, respectively.

A maximal temperature increase of 0.64 ± 0.06 K was observed for a laser duration of 100 ms. For durations of 50 ms and 20 ms, the temperature increases were 0.42 ± 0.15 K and 0.26 ± 0.03 K, respectively. A negligible temperature increase was observed when the duration was below 10 ms for the CNT/Silk scaffold. No temperature increase was noticed on the surface of the pure silk scaffold, confirming that the observed temperature increase was mainly due to the light absorption of CNTs. These results suggest that a minimal thermal effect was generated during the photoacoustic process with the conditions tested. Specifically, when the photoacoustic process was performed with a laser pulse energy of 53 μ J and a laser duration below 10 ms, no photothermal effect was exhibited, suggesting that cells will not be thermally damaged during PA stimulation of the scaffolds.

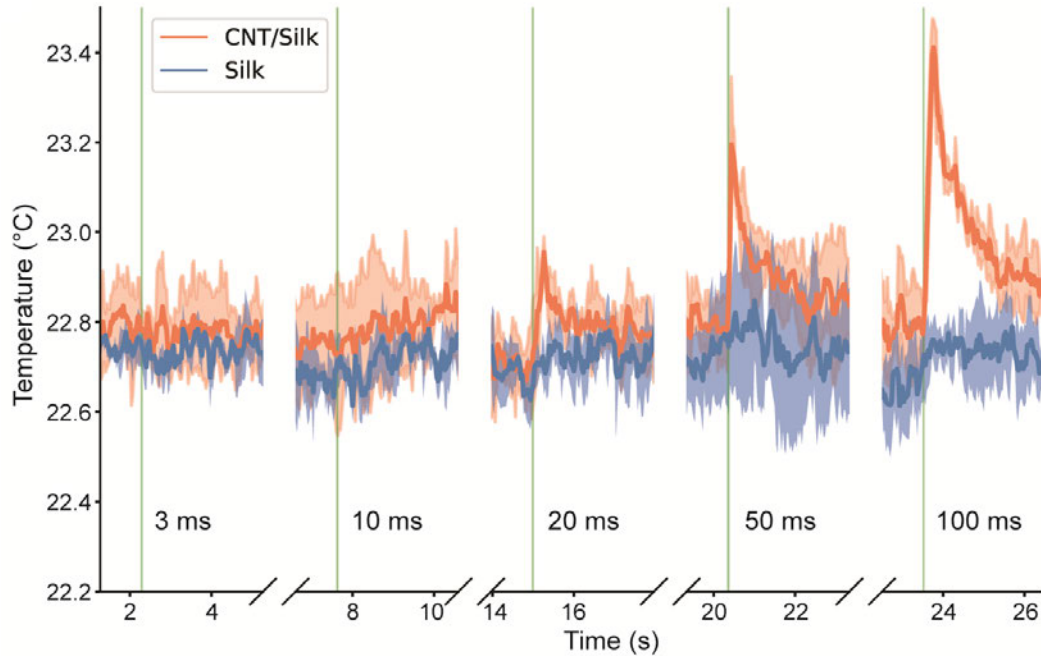


Figure 2-8: Temperature as a function of time measured at the surface of the area under laser illumination for silk film and CNT/Silk film. Laser durations of 3 ms, 10 ms, 20 ms, 50 ms and 100 ms. Laser pulse energy 53 μ J. Green solid lines indicate laser onset. $n = 3$, shaded area: \pm standard error of the mean (s.e.m.).

2.3.2 In vitro and in vivo assessment of CNT/Silk scaffold biocompatibility

We tested the biocompatibility of the CNT/Silk PA materials both in vitro and in vivo. We first compared the morphology of rat cortical neurons cultured on CNT/Silk films and glass (control group) through immunofluorescent staining and confocal microscopy (Figure 2-9a). After 7 days of in vitro (DIV) culture, neurons were fixed and labeled with anti-Tau antibody (green) and DAPI for cell nuclei (cyan) to estimate total neurite length and quantify neuron population from an area of 0.1013 mm^2 for all samples (Figure 2-1). According to the literature and our previous experience, seeding density affects neuron growth. (Lu et al., 2016) Therefore, cultures with two seeding densities were studied: $1 \times 10^5 / \text{cm}^2$, termed “low density”, and $2 \times 10^5 / \text{cm}^2$, “high density”. Compared to the control group, neurons cultured on the CNT/Silk films showed no significant differences in neurite length and number of neurons in both the high and low seeding density conditions (Figure 2-9b, c). Our observations of no significant difference in the number and neurite length of cultured neurons on coverslips and on soft CNT/Silk film at DIV7 were consistent with previous studies reported. (Benfenati et al., 2012; Georges et al., 2006) Several reasons have been proposed to explain these results. For example, the stiffness of substrate not only alters the growth of neurons but also the astrocytes, which reduces the difference. And the optimal stiffness of materials for neuronal growth is below the value of both CNT/Silk film and coverslip.

The viability of cortical neurons cultured on the CNT/Silk material was also evaluated using the MTS (3-(4,5-dimethylthiazol-2-yl)-5-(3-carboxymethoxyphenyl)-2-(4-sulfophenyl)-2H-tetrazolium) assay. In addition to the CNT/Silk films and the unloaded silk films controls, we also evaluated pure silk films with increasing concentrations of freeform functionalized CNTs in the medium, to mimic degraded CNT/Silk

scaffolds. The concentration of CNTs was calculated from a previously reported degradation rate of 20% remaining weight after 14 days of enzymatic degradation from the silk film prepared by the same protocol. (Jin et al., 2005) After DIV 14, the viability of neurons in each group was determined by MTS assay. No significant difference was detected in the CNT/Silk film group, or the unloaded silk film with increased amount of CNT group, compared to the control group (Figure 2-9c). These

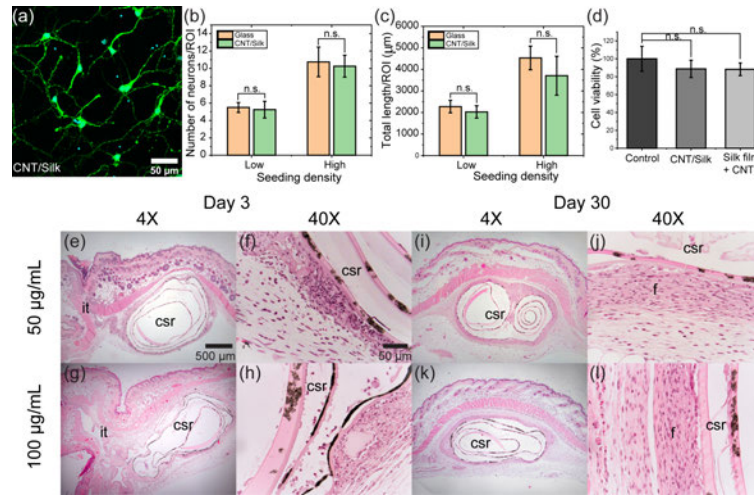


Figure 2-9: Biocompatibility of CNT/Silk film evaluated in vitro and in vivo. (a) Representative confocal image of cortical neurons cultured on CNT/Silk film. Neurons were fixed and stained with anti-Tau antibody (green) and DAPI for cell nuclei (cyan) at DIV7. (b-c) Quantification of the number of neurons per area (b) and the total neurite length per area (c). ROI: region of interest, 0.1013 mm² for all samples. The number of neurons was analyzed by counting the DAPI-stained nuclei. The total neurite length was analyzed by counting the length of anti-Tau labeled neurites. (d) Cell viability of neurons cultured on silk film as control, CNT/Silk film, silk film with freeform CNT measured by MTS assay. Error bars represent standard deviation. (e-l) Representative images of mouse skin with CNT/Silk roll implants with different CNT concentrations. (e)-(h), Day 3. Mild inflammation; (i)-(l), Day 30. it: insertion tract; csr: CNT/Silk roll; f: fibroplasia and granulation tissue.

results confirmed that the presence of the CNT/Silk scaffold did not change the morphology or the viability of cultured neurons and demonstrated the cytocompatibility

of CNT/Silk scaffolds in neuron culture.

The biocompatibility of implanted CNT/Silk scaffold was evaluated using a mouse model. CNT/Silk rolls with a length of 7 mm, diameter of 2 mm and CNT concentrations of 50 $\mu\text{g/mL}$ and 100 $\mu\text{g/mL}$ were prepared and implanted subcutaneously. The acute and chronic inflammatory responses were studied at days 3 and 30 post implantation, respectively, by H&E staining of histological slices of the explanted scaffolds. In the day 3 samples (Figure 2-9e-h), there was a focal disruption of the skin surface and an insertion tract through the skin layers that led to the implant. This insertion tract was composed of clear space and inflammatory cells. There was severe dermal hyperplasia adjacent to or overlying the implant, and there were multiple serocellular crusts on the skin surface. Some mild inflammation (mostly macrophages and neutrophils and small numbers of lymphocytes and multinucleate cells) was observed in the periphery of the CNT/Silk roll. At day 30, the insertion tract was not evident, and the skin surface was intact. The epidermis was normal to mildly hyperplastic. At day 30 (Figure 2-9i-l), there was a thick layer of fibroplasia and/or granulation tissue (fibroplasia and neovascularization) encapsulating the CNT/Silk rolls in all sections. Fibroplasia and granulation tissue are expected consequences of a mild foreign body reaction after implantation of silk biomaterials. (Li et al., 2020) Of note, a possible undesired side-effect of the formation of fibrous tissue is to limit cell responsiveness to PA stimulation by the CNT/Silk scaffolds. Future work should investigate the effect of the foreign body response on the CNT/Silk scaffolds in terms of PA stimulation, in an animal model and assessing functional outcomes. Only scattered inflammatory cells (mostly lymphocytes with fewer macrophages and multinucleated giant cells) remained. A small amount of cellular debris was observed between layers within the CNT/Silk rolls. At 3 and 30 days, there was no difference in the inflammatory response between the 50 $\mu\text{g/mL}$ and 100 $\mu\text{g/mL}$ concentration of CNT groups. The in-

flammatory response in the acute (day 3) samples was consistent with what has been described in the literature as an expected mild foreign body reaction to implanted silk biomaterials. (Anderson et al., 2008; Audouard et al., 2021; Klopffleisch and Jung, 2017) This inflammatory response was cleared by 30 days. By 30 days, fibroplasia and granulation tissue surrounded the implant with very slight inflammation and minimal overall response, indicative of biocompatibility.

Degradation is another key process of biocompatible scaffold for the successful tissue regeneration. Silk is mostly degraded through enzymatic degradation by proteases, like protease XIV, α -chymotrypsin, matrix metalloproteinase and collagenase. (Li et al., 2020; Horan et al., 2005; Brown et al., 2015) This degradation has been shown to decrease the molecular weight and strength of the silk over time in vitro. In vivo, silk degradation has been shown in numerous animal studies, and can be tuned from minutes to years by adjusting the properties of the scaffold. In vivo, the host immune system plays an important role in silk degradation in vivo, (Wang et al., 2008) mediated by multiple pathways, including phagocytosis and secreted proteolytic enzymes. As such, in vivo degradation of silk scaffold is highly dependent on both scaffold properties (molecular weight, molecular structure and crystallinity, porosity, material format, geometry and surface topography) and the properties of the host (including species, implant site and animal health). (Li et al., 2020) Previous work on CNT/silk biomaterials have demonstrated that incorporating CNTs does not have a significant effect on the secondary structure of silk fibroin, assessed by FTIR. (Zhao et al., 2020) These results suggest that the biological properties of silk scaffolds, including biocompatibility and degradation, are not affected by the addition of CNTs.

2.3.3 CNT/Silk scaffold stimulated neuronal activities through PA waves

To confirm the stimulation function of the CNT/Silk scaffolds, GCaMP6f labeled primary neurons (DIV 12-14) were cultured on the CNT/Silk films and calcium imaging was used to monitor neuronal activity (Figure 2-10). A 3-nanosecond pulsed laser at

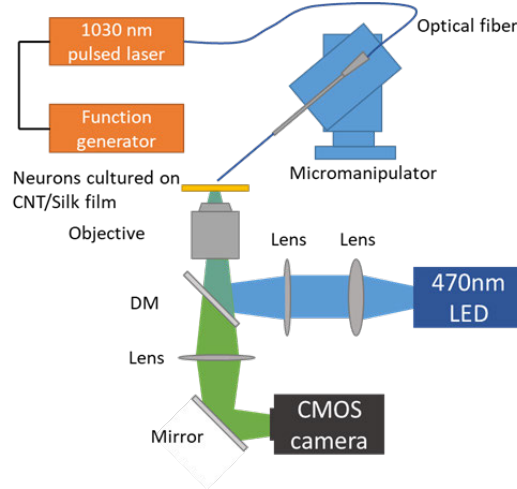


Figure 2-10: Calcium imaging was performed on an inverted wide field fluorescence microscope to monitor neuronal activities. Pulsed laser light was delivered through a multimode optical fiber. The fiber location and the illumination area were controlled by a micromanipulator. DM: dichroic mirror.

1030 nm with a repetition rate of 1.7 kHz was used to generate a laser pulse train with a duration of 5 ms, corresponding to 8 pulses with a pulse energy of 14.7 μJ (energy density = 29.4 mJ/cm^2) for PA neural stimulation. The laser light was delivered to the CNT/Silk surface through a 200 μm core diameter multimodal optical fiber. The location of the illumination area was controlled by a 3D micromanipulator, and the illumination area was calculated to be 0.05 mm^2 . Representative fluorescence images of the neuron cultures on the CNT/Silk films before and after PA stimulation are shown in Figure 2-11a, b, with the dashed circles showing the illumination area. Increased fluorescence intensity of GCaMP6f in individual neurons within the illumination area was clearly observed immediately after applying the pulsed laser. Of the

18 neurons studied in one trial, 17, corresponding to 94.4%, showed an increase in fluorescence greater $\Delta F/F_0$ than 10% after the onset of laser exposure (Figure 2.11b). F_0 is the baseline fluorescence signal of the neurons before the stimulation. The map of maximum fluorescence change $\Delta F/F_0$ (Figure 2.11c) also confirmed that neurons within the illumination area were successfully activated, while no fluorescence change was observed outside of the illumination area.

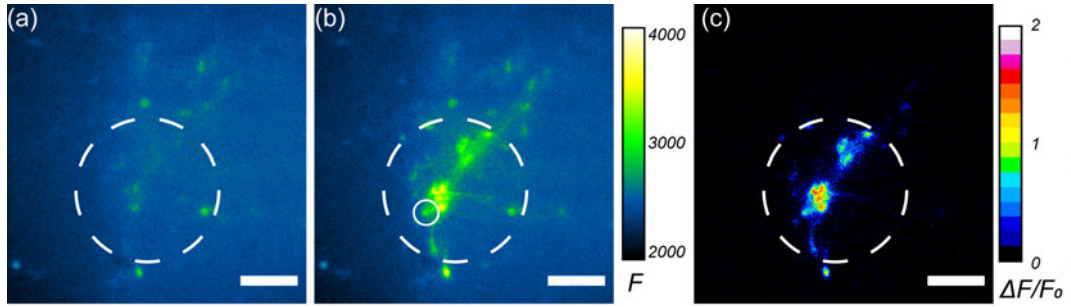


Figure 2.11: (a, b) Representative calcium images of GCaMP6f-transfected cortical neurons at DIV 14 cultured on CNT/Silk film before (a) and after (b) the PA stimulation. Laser: 3 ns laser applied for a 5 ms duration with a 1.7 kHz repetition rate (corresponding to 8 pulses) and 14.7 μJ pulse energy. (c) Map of the maximum fluorescence change $\Delta F/F_0$ induced by the PA stimulation. Dashed lines: Illumination area. Scale bars: 100 μm .

To confirm that the observed activation was due to PA stimulation rather than light illumination only, the calcium traces of PA-stimulated neurons (neurons cultured on CNT/Silk films with light applied, labeled CNT/Silk light +) and two control groups, including neurons cultured on CNT/Silk films without application of light (labeled CNT/Silk light -) and neurons cultured on silk films with application of light (labeled Silk light +). Representative traces are shown in Figure 2.12a. No significant fluorescence change was observed in the control groups. This result confirmed that the induced neuronal activity observed was due to the PA stimulation generated by the CNT/Silk films.

We next investigated the effect of laser pulse energy on PA stimulation. The

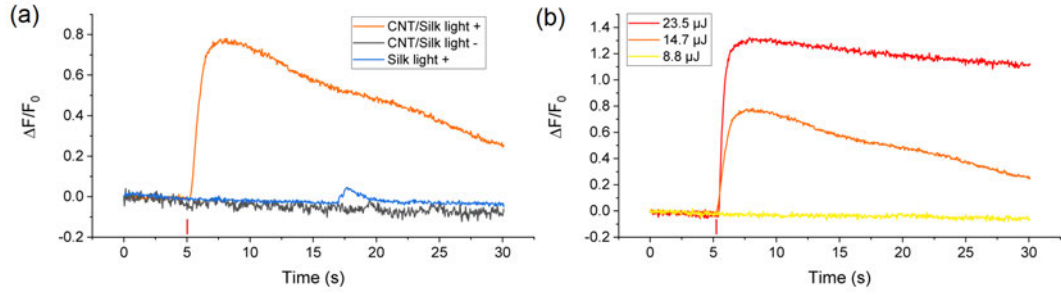


Figure 2-12: (a) Representative calcium traces of neuron cultured on CNT/Silk scaffold within the laser illumination area (CNT/Silk light +, orange), out of the laser illumination area (CNT/Silk light -, black) and cultured on silk scaffold within the laser illumination area (Silk light +, blue). (b) Representative calcium traces of neurons cultured on CNT/Silk film responding to PA stimulation with the pulse energy of 23.5 μ J (red), 14.7 μ J (orange) and 8.8 μ J (yellow).

duration of the pulse train in each stimulation was fixed at 5 ms. Three laser pulse energies, 23.5 μ J, 14.7 μ J and 8.8 μ J were applied to the CNT/Silk films to modulate neural activity. The PA stimulation successfully induced neural activity with laser pulse energies of 23.5 μ J and 14.7 μ J, but not with 8.8 μ J. Representative calcium trances are plotted in Figure 2-12b. Results from more neurons for each pulse energy are plotted as heatmaps in Figure 2-13a-d. For the laser pulse energy of 23.5 μ J and 14.7 μ J, 99.0% and 96.1% neurons in the illuminated area showed a fluorescence change above 10% after laser onset, respectively. But when the laser pulse energy was reduced to 8.8 μ J, the ratio was only 1.2%, which is more consistent with spontaneous action potential firing. The averages of maximum fluorescence change obtained from these three groups and from neurons cultured on the pure silk scaffolds as controls with pulse energy of 14.7 μ J are compared in Figure 2-13e. With the laser pulse energy of 23.5 μ J and 14.7 μ J, neurons showed an average maximum fluorescence change of $134\% \pm 56.9\%$ and $87.3\% \pm 40.8\%$, significantly higher than $7.7\% \pm 16.9\%$ from the silk only control group. When the pulse energy was reduced to 8.8 μ J, it was no longer able to evoke activation and the amplitude of the maximum fluorescence

change was similar to the silk control group (n.s., $p = 0.982$). These results suggested that there was a threshold of laser pulse energy between 8.8 μJ and 14.7 μJ required for activation, given a pulse train duration of 5 ms. We had previously measured that the CNT/Silk films generated PA waves with a peak pressure of 0.185 MPa for a laser pulse energy of 14.7 μJ . Therefore, we conclude that the threshold pressure for successful activation is close to 0.185 MPa, which is in the range of pressure (0.1-2 MPa) used for ultrasound neural stimulation. (Tyler et al., 2018; Tufail et al., 2011) Larger pulse energy led to PA waves with larger amplitudes (Figure 2-7 right panel) and induced larger calcium influxes, suggesting more action potential firings.

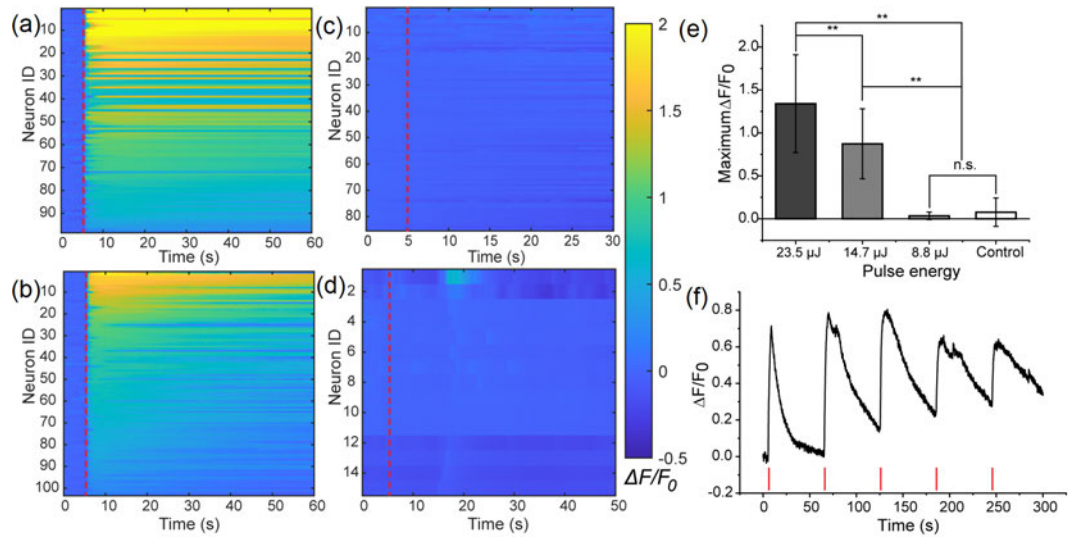


Figure 2-13: (a-d) Colormaps of fluorescence change in neurons cultured on CNT/Silk scaffold with laser pulse energy of 23.5 μJ (a), 14.7 μJ (b) and 8.8 μJ (c) and silk scaffold with laser pulse energy of 14.7 μJ (d). All PA stimulation was performed at 5 s and marked by the red dashed lines. The duration of each stimulation was fixed at 5 ms. (e) Average of maximum fluorescence intensity changes shown in (a-d). Error bars represent standard deviation ($n > 14$, ** $p < 0.01$, n.s. $p = 0.982$, one-way ANOVA and Tukey's means comparison test). (f) Calcium trace of the neuron marked by the solid circle in Figure 2-11 undergone repeated PA stimulation.

To further investigate whether CNT/Silk scaffolds activate neurons reliably and

repeatedly, we stimulated the same area 5 times sequentially, at 1 min intervals. Five repeated successful activations were observed for all 5 stimulations of the same neuron (Figure 2-13f). We observed a decrease in $\max \Delta F/F$ for each sequential stimulation, which could be attributed to calcium depletion (Cohen and Fields, 2004; Asteriti et al., 2017) or spike frequency adaptation. (Ha and Cheong, 2017) This result demonstrated the repeatability of PA stimulation of the CNT/Silk scaffolds and no damage inflicted to the neurons by PA stimulation.

To investigate if there is any lasting damage caused by PA stimulations, nucleus staining was also performed by using Sytox Green for determination of cell viability. Dead neurons with a stronger Sytox Green signal (fluorescence intensity > 600 a.u.) before the stimulation were identified as the positive control group. Sytox Green fluorescence intensity of neurons in both groups remains the same 10 minutes after stimulation. The sample group shows much lower Sytox Green signals compared with the positive control group. (Figure 2-14). These results confirmed no lasting damage was induced to neurons by PA stimulations.

To confirm the minimal thermal effect associated with light conditions used for successful PA stimulation, we examined the surface temperature of the CNT/Silk scaffolds again for these specific conditions using a miniaturized ultrafast thermal probe (Figure 2-15). The temperature increase was below 0.1°C , 0.15°C and 0.33°C for $8.8 \mu\text{J}$, $14.7 \mu\text{J}$ and $23.5 \mu\text{J}$ laser pulse energies, respectively. These temperature changes were much smaller than the previously reported threshold for thermally induced neural activation through infrared neural stimulation ($\Delta T > 5^{\circ}\text{C}$). (Shapiro et al., 2012) Therefore, neuronal activity stimulated by the CNT/Silk scaffolds was mainly due to the generated PA waves rather than a thermal effect. This minimal thermal effect means that CNT/Silk PA stimulation avoids potential thermotoxicity to neural tissue, compared with thermal-based neural stimulation.

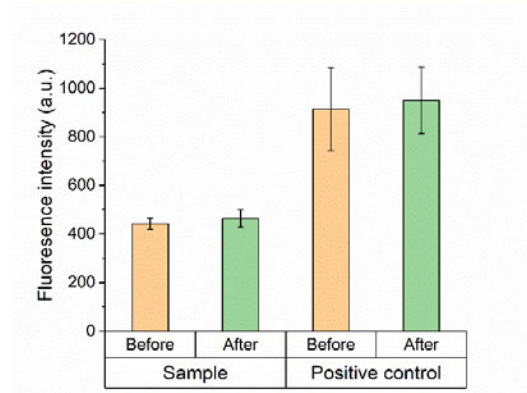


Figure 2-14: No lasting damage was confirmed by Sytox Green nucleus acid staining. Neurons in the sample group were stimulated 5 times (pulse energy of 14.7 uJ, duration of 5 ms) with an interval of one minute in between. Dead neurons with a stronger Sytox Green signal (fluorescence intensity > 600 a.u.) before the stimulation were identified as the positive control group. Sytox Green fluorescence intensity of neurons in both groups remains the same 10 minutes after stimulation. The sample group shows much lower Sytox Green signals compared with the positive control group (463.29 vs 949.67).

2.3.4 PA stimulations promote neurite extension

After demonstrating the ability of CNT/Silk scaffolds for neural stimulation, we next evaluated the efficacy of PA stimulation on neurite extension. Whole DRG explants from E15 Sprague Dawley (SD) rat embryos were utilized as an ex vivo model. DRG explants are widely used to facilitate the study of nerve regeneration, because they allow for the evaluation of neurite outgrowth. (Klimovich et al., 2020) DRG explants with a diameter of approximately 300 μm were randomly selected and seeded onto either CNT/Silk scaffolds or a glass substrate as a control. Both substrate surfaces were coated with poly-D-lysine (50 $\mu\text{g}/\text{mL}$) and laminin (5 $\mu\text{g}/\text{mL}$) to improve DRG adhesion. DRGs in all groups were immersed in neurobasal medium supplemented with N2 and B27 but without neurotrophic factors. Using calcium imaging, we first confirmed that the PA waves generated by the CNT/Silk scaffold also stimulated DRG explants (Figure 2-16). All DRGs were grown for 2 days prior to stimulation.

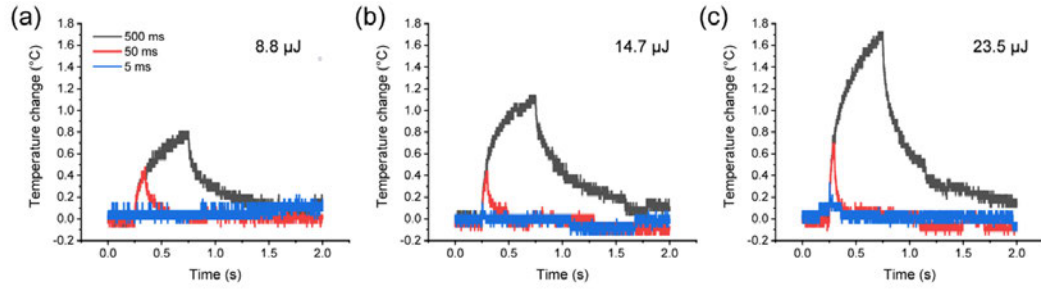


Figure 2-15: Heat profile of CNT/Silk scaffold under the laser illumination. Three pulse energy, 8.8 μJ (a), 14.7 μJ (b) and 23.5 μJ (c) were examined with duration of 5 ms, 50 ms and 500 ms.

The stimulation conditions were the same as those used in cultured neurons (a laser train duration of 5 ms, 1.7 kHz repetition rate, a pulse energy of 14.7 μJ).

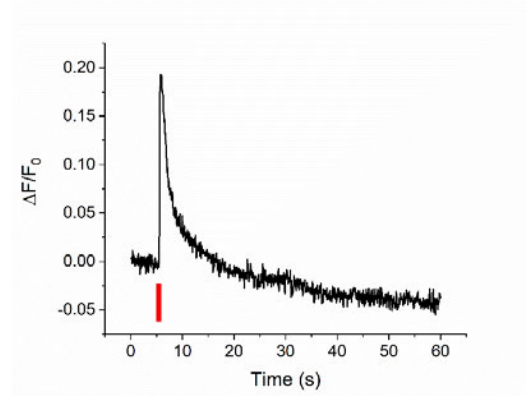


Figure 2-16: Calcium trace of a GCaMP6f transfected DRG at DIV 10 under the PA stimulation with the pulse energy of 14.7 μJ and the duration of 5 ms. The stimulation was triggered at 5 s.

The response of DRG to PA stimulation was also investigated through the extracellular electrical recording (Figure 2-17a). The extracellular potential of DRG explant cultured on the CNT/Silk film was recorded under five repeated PA stimulations with the same laser condition above. A recording of the metal electrode in PBS without DRG tissue under the same laser conditions was performed as control group (Figure 2-17b). Light induced artifacts due to photoelectric effect on the metal electrode were observed. Compared with control group, the potential change recorded

from DRG explants showed an amplitude of 3 times larger than the control group and longer recover time (Figure 2-17c), indicating the change is due to the neuronal activities induced by PA stimulation. This extracellular recording result, together with the results of calcium imaging, confirmed the ability of CNT/Silk film in stimulating DRG explants through photoacoustic signals. Note that under these conditions the temperature increase associated with the stimulation was 0.15°C (Figure 2-15b), indicating a negligible thermal effect on neurite growth. (Cancalon, 1985)

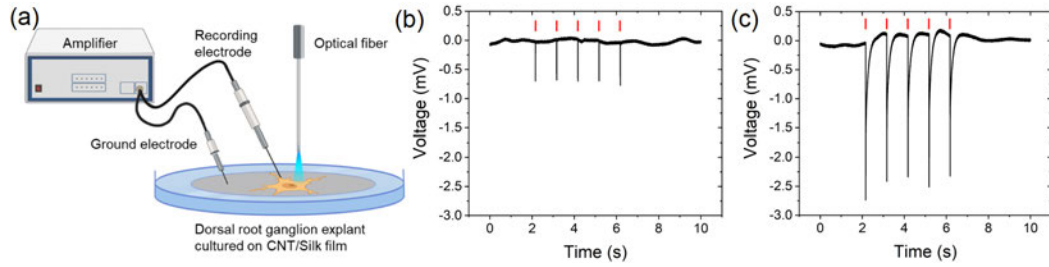


Figure 2-17: (a) Schematic of extracellular recording and PA stimulation on DRG explants cultured on the CNT/Silk film. (b) Artifacts induced by the laser illumination recorded in the PBS without DRG explants. (c) Extracellular recording of DRG explants cultured on the CNT/Silk film. Red lines: Five repeat photoacoustic stimulations were performed with laser pulse energy of $14.7 \mu\text{J}$.

To study the effect of stimulation on outgrowth, guided by previous electrostimulation and optogenetic stimulation work on neural growth, we applied one time PA stimulation for a total duration of 1 hour. During this 1-hour treatment, the laser pulse train of 5 ms every 2 minutes was applied to avoid potential desensitization and calcium depletion.

We designed the experiments to evaluate the effects of PA stimulation and substrates on neurite outgrowth. For this purpose, in addition to the PA-stimulated group (CNT/Silk light +), we tested three other control groups, including DRGs cultured on CNT/Silk without light illumination (CNT/Silk light -), DRGs cultured on glass with light illumination (glass light +) and DRGs cultured on glass without light

stimulation (glass light -). All DRGs were grown for 2 days prior to stimulation, and fixed and stained at day 10 with Anti-Neurofilament 200 to label neurites and DAPI to label nuclei for immunofluorescence imaging and analysis (Figure 2-18a-h).

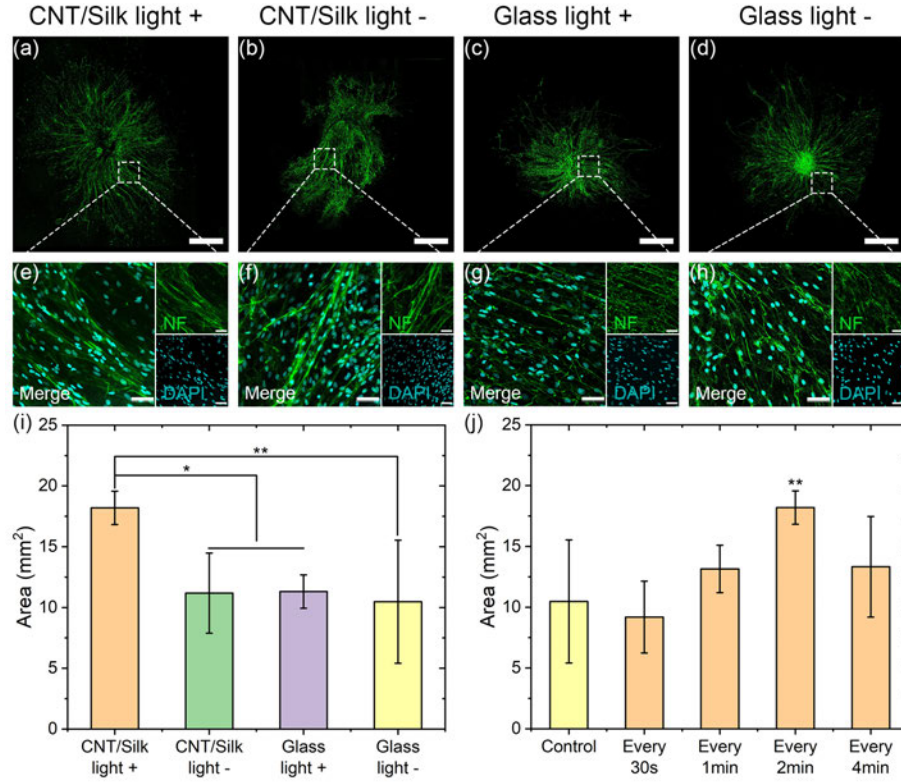


Figure 2-18: PA stimulation promotes the neurite outgrowth. (a-d) Representative confocal images of DRGs stained for neurofilament (green): DRG cultured on CNT/Silk film with laser illumination (CNT/Silk light +, a) and without laser illumination (CNT/Silk light -, b). DRG cultured on glass bottom dish with laser illumination (Glass light +, c) and without laser illumination (Glass light -, d). Scale bar: 1 mm. (e-h) High-resolution confocal images of DRGs stained with Anti-Neurofilament 200 (NF) for neurites (green) and DAPI for nucleus (cyan). Scale bar: 50 μ m. (i) The average neurite coverage area for DRGs in four groups. (j) The average neurite coverage area for PA stimulated DRGs with various stimulation frequency. Control: DRGs cultured on glass without light stimulation (glass light -). All DRGs were allowed to grow for 2 days before stimulation, and were fixed at day 10.

To minimize human error during area counting, an algorithm for determining coverage area was developed (Figure 2-19). High magnification confocal images demonstrated that the neurites and nuclei were stained by the corresponding antibodies. The neurite extensions of PA-stimulated DRGs were significantly promoted as compared to the DRGs in the control groups (Figure 2-18i). For the PA-stimulated DRGs, the average growth area was $18.19 \pm 1.38 \text{ mm}^2$, a 1.63-, 1.61- and 1.74-fold increase as compared to DRGs cultured on CNT/Silk without light illumination ($11.18 \pm 3.24 \text{ mm}^2$), DRGs cultured on glass with light illumination ($11.31 \pm 1.37 \text{ mm}^2$) and DRGs cultured on glass without light illumination ($10.48 \pm 5.06 \text{ mm}^2$). These results confirmed that PA stimulation generated by the CNT/Silk scaffolds had a strong positive effect on neurite outgrowth and offers a new strategy to promote nerve regeneration.

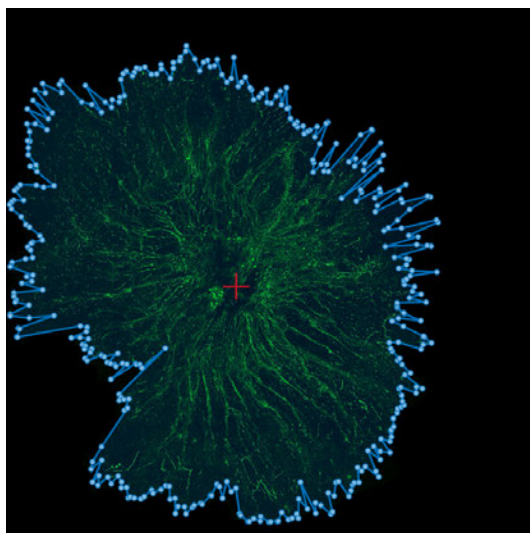


Figure 2-19: The coverage area of DRGs was determined by a computer algorithm to minimize the artificial error. The polygon was constructed by 360 endpoints along each direction separated by 1° .

To investigate the effect of PA stimulation dose on neurite outgrowth, we further examined the neurite extension of PA-stimulated DRGs varying the stimulation frequency from every 30 seconds to every 4 minutes, while maintaining the same

stimulation conditions and the total duration of 1 hour (Figure 2·20). The average coverage area observed for groups stimulated every 30 s, every 1 min, every 2 min and every 4 min were $9.19 \pm 2.95 \text{ mm}^2$, $13.15 \pm 1.95 \text{ mm}^2$, $18.38 \pm 1.38 \text{ mm}^2$ and $13.14 \pm 4.14 \text{ mm}^2$, respectively. These results indicated that the positive effect of PA stimulation on neurite outgrowth reached a maximum when stimulation was applied every 2 minutes. For the group with the highest stimulation frequency at every 30 s, the average coverage area of DRGs ($9.19 \pm 2.95 \text{ mm}^2$) was slightly smaller than the control group ($10.48 \pm 5.06 \text{ mm}^2$).

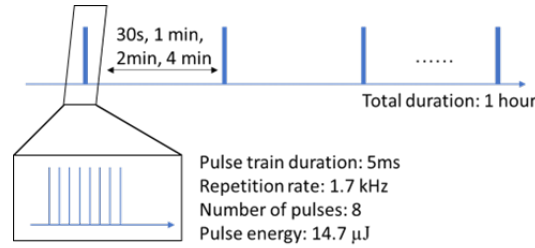


Figure 2·20: The schematic of laser pulse train used for investigating the effect of PA dosage. The total duration was fixed at 1 hour. The stimulation frequency was varied from every 30 seconds to every 4 minutes. Within each 5 ms pulse train, 8 pulses with pulse energy of 14.7 μJ were provided.

To test whether PA stimulation increased the expression of neurotrophic factors, we measured the concentration of BDNF and nerve growth factor (NGF) 1 day after stimulation in PA-stimulated DRGs at the optimized stimulation frequency of every 2 min for 1 hour. DRGs in the other three control groups used above were also tested as controls (Figure 2·21). Both BDNF and NGF expression were measured by ELISA assay. PA-stimulated DRGs showed a concentration of BDNF of $86.52 \pm 17.07 \text{ pg/ml}$, a 1.96-fold increase, compared to $44.20 \pm 22.31 \text{ pg/ml}$ measured for the control group where DRGs were cultured on glass without light stimulation. The two other control groups, DRGs cultured on CNT/Silk without light stimulation and DRGs cultured on glass with light stimulation, showed BDNF concentrations of 26.19

± 24.82 pg/ml and 33.03 ± 25.58 pg/ml, close to the glass light- control. All four groups exhibited a similar expression level of NGF, and no significant difference was observed in PA-stimulated DRGs ($p > 0.05$).

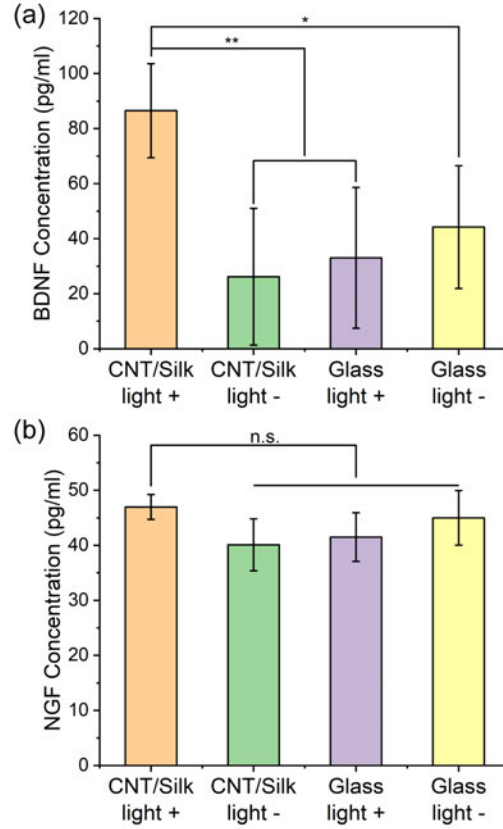


Figure 2-21: Impact of PA stimulation on the expression of BDNF and NGF. (a-b) The average concentrations of BDNF (a) and NGF (b) of PA-stimulated and unstimulated DRGs. Samples were collected 24 hours after PA stimulations. PA stimulations were provided every 2 minutes within the total duration of 1 hour. The stimulation condition was a laser train duration of 5 ms 1.7 kHz repetition rate, and the pulse energy of 14.7 μ J.

The increase in intracellular calcium caused by electrical stimulation and optogenetics has been shown to impact neural regeneration. (Park et al., 2015a; Al-Majed et al., 2000a) As a central regulator for neural growth, calcium serves multiple functions in the regeneration process (Mahar and Cavalli, 2018) including regulating gene

expression, reducing the membrane tension through activating proteases to cleave spectrin, or stimulating growth cone formation. These calcium-sensitive processes each have their own optimum calcium level, which could conceivably lead to an overall optimal level of calcium resulting in maximal neurite growth. Increasing calcium levels to reach the optimal level will increase growth, while increasing the level further above the optimal level will decrease the effect and could even lead to cell death. (Doherty et al., 2000; Kater and Mills, 1991) With PA stimulation, the optimal frequency of every 2 min observed could be associated with the optimal calcium level for neurite outgrowth.

Impacting signaling pathways of neurotrophic factors is one mechanism through which stimulation promotes neural regeneration. Previous work demonstrated that increased neurite extension in response to electrical stimulation was correlated with changes in BDNF expression (Lever et al., 2001) and the externalization of its high affinity tropomyosin-related kinase B (TrkB) receptor. (Meyer-Franke et al., 1998) Besides the upregulation of BDNF, the concentration of NGF was observed to continuously increase both in electrically stimulated and unstimulated DRGs, but the elevation of NGF in stimulated DRGs was greater. (Park et al., 2015a) Our results indicated that PA stimulation with an optimized dose increased the expression of BDNF but did not significantly affect NGF. From the calcium imaging, we confirmed PA stimulation induced a strong and slow decay calcium influx in neurons. And the BDNF expression is regulated in an activity-dependent way, especially by the calcium. (West et al., 2001; Tao et al., 2002) Here we suggest that PA stimulation promoted neurite outgrowth through two steps. First, PA stimulation elevated intracellular calcium concentration either by calcium influx following action potential firings, or directly opening the calcium channels. Then the elevated calcium concentration regulated a series of regeneration-related activities, including the expression

of neurotrophic factors like BDNF and finally led to a promoted neurite outgrowth.

2.4 Conclusion

We integrated PA capability into a silk-based neural scaffold using a nanocomposite approach, in which PEG-functionalized CNTs were dispersed in the silk matrix. Upon excitation by the 1030 nm pulsed laser, the CNT/Silk film generated a broadband PA wave, whose amplitude can be controlled by varying CNT concentration and laser energy. The pressure of the generated PA waves for successful neural stimulation is measured to be 0.185 MPa. Minimal thermal effects were associated with the illumination or the PA generation. The biocompatibility of this multifunctional scaffold was confirmed in vivo through H&E staining of histological slices of subcutaneously implanted scaffolds. The CNT/Silk scaffolds supported neural growth, and compared with control group, did not affect the morphology or viability. Through time-resolving calcium imaging, we demonstrate the reliable and repeatable neural stimulation function of the scaffold on the cultured cortical neurons with $> 94\%$ neurons in the light illumination area activated. Using the DRG neurite extension model, CNT/Silk scaffolds are shown to promote neurite outgrowth of DRG explants by 1.74-fold and upregulate the expression of BDNF compared with the control group.

Photoacoustic neural stimulation is an emerging method, and its mechanisms of action are not fully understood. For ultrasound neurostimulation using conventional transducers, several hypotheses have been proposed, including the activation of mechanosensitive ion channels, (Kubanek et al., 2016; Kubanek et al., 2018; Ye et al., 2018; Yoo et al., 2022) the transient mechanical disruption of the neural membrane including the opening of pores, (Shi et al., 2020; Lin et al., 2010) and the induction of capacitive currents by intramembrane cavitation. (Krasovitski et al., 2011; Plaksin et al., 2014) Recently, Sangjin et al. show that ultrasound excites

neurons through a primarily mechanical mechanism mediated by calcium-selective mechanosensitive ion channels. The activation of these calcium channels leads to a gradually calcium accumulation, generating a burst firing response. Our study indicates that transient disruption of the membrane and activation of calcium ion channels are possibly involved in PA neural stimulation. (Jiang et al., 2020b; Shi et al., 2021) Similar to the result of ultrasound stimulation, a burst of multiple action potentials firings triggered by the PA stimulations was also observed in our previous study using patch clamp recording, (Shi et al., 2021) which might be a consequence of transient calcium currents. (Huguenard, 1996) These results also explain why the neurons showed a relatively long decay constant of GCaMP dynamics. In the present work, we demonstrate that a PA material, specifically CNT/Silk, can be a new route to promote neural growth through neural stimulation. Compared to existing neural stimulation methods (electrical stimulation and optogenetics), this offers several advantages. First, it is a light-mediated method using NIR-II light. Because of its longer wavelength, NIR-II light has sufficient penetration depth in human tissue. (Cao et al., 2020) Thus, PA materials excited by NIR-II light potentially enable non-invasive postoperative stimulation. Second, compared with optogenetic stimulation, PA material-based neural stimulation does not require genetic transfection. As a foreign protein antigen, either the opsin itself or the expression method, like viral transfection, may raise technical and ethical issues for human applications. (Ordaz et al., 2017) Also, our work demonstrated that the photoacoustic capability can be integrated through a hydrogel nanocomposite approach. Owing to the design flexibility, this approach adds new light-responsiveness into hydrogel materials. Among current strategies, photothermal is a major mechanism that enables the light-responsive functions of hydrogel scaffolds in numerous applications. (Shao et al., 2018; Andoy et al., 2020; Gangrade et al., 2020) However, in tissue engineering applications, (Shi et al.,

2015) damage due to heating surrounding tissues has to be considered. The PA-mediated light-responsiveness eliminates thermal toxicity because of the negligible temperature increase.

Chapter 3

Multifunctional Fiber-based Optoacoustic Emitter as a Bidirectional Brain Interface

3.1 Introduction

Bidirectional communication with dynamic local circuits inside the brain of individual behaving animals or humans has been an invaluable approach for fundamental studies of neural circuits and for effective clinical treatment of neurological diseases, like epilepsy, Parkinson's disease, and depression. (Wilbrecht and Shohamy, 2009; Chen et al., 2017) Additionally, bidirectional neural interface paves the way for the closed-loop control, as it could enable more sophisticated, real-time control over neural dynamics, (Sohal et al., 2009) behaviors (Paulk et al., 2015) and achieve effective therapeutic effect in neurological disease. (Rosin et al., 2011; Paz et al., 2013) To achieve real time assessment of the stimulated outcome, neural interfaces with ability to simultaneously manipulate and directly monitor the neural activities are preferred. Among the technologies developed in past decades, electrical stimulation and electrophysiology recording have been widely used and forms the basis of current implantable devices, which has been applied to clinical applications. (Harmsen et al., 2020) For example, to restore both the motor and sensory modalities, electric stimulation of the cortical surface is often associated with electrophysiology recording, (Hughes et al., 2020; Zhou et al., 2018) like electrocorticography (ECoG). Also, the electrical stimulation and recording system has demonstrated promising treatment effect in neu-

rological diseases, such as epilepsy. The responsive neurostimulation (RNS) system, leveraging ECoG recording as the trigger to provide stimulation, showed a statistically significantly greater reduction in seizure frequency and the benefits increased over time in a two-year study. (Heck et al., 2014; Sun and Morrell, 2014) However, the current-controlled or voltage-controlled stimulation field may interfere with the electrical signals used for recording, leading to artifacts in electrophysiology recording. (Chen et al., 2017; Miocinovic et al., 2009) Although researchers are improving its performance through technologies such as current steering, (Paff et al., 2020) novel electrode design, (Buhlmann et al., 2011) and artifacts cancellation, (Qian et al., 2016) considering the intrinsic conductivity of brain tissue, (Koessler et al., 2017) the artifact issues is hard to be fully eliminated. Therefore, electrical stimulation for the bidirectional communication of brain may not be the ideal candidate, especially when working with the electrophysiology recording.

Exploring alternative neuromodulation methods that are orthogonal with electrical recording and potentially improve the spatial resolution of modulation could offer a new bidirectional brain interface for fundamental studies and clinical applications. Optogenetics is a powerful method that utilizes light and transfected opsins to control and manipulate neurons in brain and other neural systems with cell specificity. (Deisseroth, 2011) It targets and modulates only cells that express the photosensitive channels of interest, while leaving other cells unaffected. (Cardin et al., 2010) This further boosts the stimulation selectivity within the spatial pattern of illumination. To take this advantage, early efforts developed so-called optoelectrodes by simply assembling the optical fibers for optogenetics stimulation with the electrodes, such as Utah arrays, (Abaya et al., 2012a; Zhang et al., 2009; Wang et al., 2011) Michigan probes (Royer et al., 2010; Zhang et al., 2016) and microwires. (Kravitz et al., 2013) Semiconductor fabrication techniques and multiple material processing

methods have recently been applied to improve the integration of those bidirectional devices. New processing techniques not only make the device more compact but also strengthen its functionality and biocompatibility. For example, monolithically integrated micro-light-emitting-diodes (μ LEDs) were used to reduce the complexity of light-guide structures and significantly boosted the number of stimulation sites and stimulation resolution. (Wu et al., 2015; Vöröslakos et al., 2022) Alternatively, a high-throughput thermal drawing method has been used to integrate the function components, for example, electrodes, microfluidic channels, and optical waveguides, to the flexible multifunctional polymer fiber. (Canales et al., 2015; Park et al., 2017) Through this approach, the flexible fiber probes showed low bending-stiffness and enabled multifunctionalities, including optical waveguide, electrical recording and drug delivery. (Jiang et al., 2020a; Antonini et al., 2021; Park et al., 2021) Optogenetics utilizing the expression of light-sensitive opsins in neurons through gene modification (Park et al., 2017) enables cell specificity. However, it also impose challenges of low efficiency in viral transfection and safety when applying optogenetics to non-human primates and human, (Bansal et al., 2022) limiting its further applications in fundamental studies in primates and clinical applications. Photothermal modulation also leverages the optical waveguide developed in a variety of interfaces to perturb neural activity. (An and Nam, 2021; Lyu et al., 2016) For example, Meneghetti et al. developed a soft fibre-based device to deliver the infrared laser pulse in the 2 μ m spectral region while recording electrophysiological signals, (Meneghetti et al., 2022) but the infrared laser illumination on the seconds scale raises some safety concerns for thermal toxicity in clinical applications. (Cayce et al., 2014) In addition, chemical modulator using the drug delivery capability of the multifunctional neural probe can also work with a pathologic electrophysiological recording, (Jonsson et al., 2016) but have a limited spatiotemporal resolution.

Recently, our team showed non-genetic optoacoustic neural stimulation with a high spatial resolution up to single neuron level. (Jiang et al., 2020b; Shi et al., 2021) In an optoacoustic process, the pulsed light is illuminated on an absorber, causing transient heating and thermal expansion, and generating broadband acoustic pulses at ultrasonic frequencies. (Wang and Hu, 2012; Lee et al., 2018) As a light-mediated neural modulation method, optoacoustic is an ideal candidate to work with electrical recording for bidirectional neural communication. Compared with existing technologies, it exhibited the advantages as a light mediated method, including a high spatial resolution and minimal crosstalk noise with electrical recording. Importantly, the non-genetic optoacoustic neurostimulation alleviates the challenges and safety concern in optogenetics since no viral transfection is required.

Here, we developed a multifunctional fiber-based optoacoustic emitter (mFOE) as a miniaturized bidirectional brain interface performing simultaneously non-genetic neural stimulation and electrical recording of the neural activities. Through a thermal drawing process, (Canales et al., 2015; Abouraddy et al., 2007) fabrication of mFOE integrated an optical waveguide and multiple electrodes within a single fiber with a total diameter of 300 μm , comparable to the typical size of silica fibers used in optogenetic studies. An optoacoustic coating was selectively deposited to the tip of the core optical waveguide in the mFOE through a controlled micro-injection process. Upon nanosecond pulse laser delivered to the photoacoustic coating, the mFOE generates a peak-to-peak pressure greater than 1 MPa, confirmed by the hydrophone measurement, which is sufficient for successful neural stimulation *in vitro* and *in vivo*. By calcium imaging, the optoacoustic stimulation function of the mFOE was validated in Oregon green-loaded rat primary neurons. Importantly, we demonstrated the reliable functions of the chronic implanted mFOE for simultaneously stimulating and recording neurons in mouse hippocampus. Chronic recording also demonstrated that

the embedded electrodes could monitor both the local field potential and spike activities in the mice brain. The histological evaluation of the brain tissue response confirmed that our flexible mFOE established a stable and biocompatible multifunctional neural interface. mFOE is the first device integrated both optoacoustic stimulation with electrical recording for bidirectional neural communication. With the bidirectional capabilities and excellent biocompatibility, it offers a non-genetic tools probing brain circuits, alternative to the optoelectrode devices, with improved feasibility in non-human primates and human. It also opens up potentials for closed-loop neural stimulation and brain machine interface.

3.2 Materials and Methods

3.2.1 Multifunctional fiber fabrication and optoacoustic emitter integration

Multifunctional fibers were fabricated from a preform fiber and then drawn into thin fibers through TDP in a customized furnace. For the preform fiber, PVDF film (0.003" Thick, 8675K21, McMaster) and PC film (100 μm thick, LEXANTM FR83, laminated plastics) were rolled onto a PC rod (1/2" Diameter, 8 Feet Long, 8571k14, McMaster) and followed by a consolidation process in vacuum at 200 °C. Next, four rectangular grooves (2 mm \times 2 mm) were machined on the solid PC layer and inserted with the BiSn (RIBBONBO-123407, Indium Corporate) electrodes. Then, another PVDF layer was rolled over the rod to form an insulation layer for the electrodes and followed by an additional PC as the sacrifice layer for the convenience of TDP. The detailed fabrication process was discussed in the previous paper. (Jiang et al., 2020a)

A composite of 10% carbon black (diameter < 500 nm, Sigma Aldrich) and 90% polydimethylsiloxane (PDMS, Sylgard 184, Dow Corning Corporation, USA) were used as the optoacoustic material. The mixture was sonicated for 1 hour followed

by degassing in vacuum for 30 minutes. The mixture was then filled in the glass micropipette (Inner diameter = 30 μm , TIP30TW1, World Precision Instruments, USA) and connected to the pico-liter injector (PLI-100A, Warner Instruments, USA). Before the injection of optoacoustic material, the deposition surface of the fiber was polished by optical polishing papers to reduce roughness from 30 μm to 1 μm . Under the microscope, the glass micropipette was aligned with the core waveguide of multifunctional fiber and the mixture was deposited to the surface of the core waveguide by controlling the injection pressure and time. The deposited fiber was then cured vertically at room temperature for 2 days. Then the cured optoacoustic emitter was inspected under an upright optical microscope to confirm its position and thickness through top view and side view, respectively.

Before use, mFOE was further prepared for the optical coupling and electrodes connection. For the optical coupling, a ceramic ferrule (Thorlabs, USA) was added and affixed to the end of the fiber by the 5-min epoxy (Devcon, ITW Performance Polymers, USA). Then the end surface was polished by optical polishing papers to reduce roughness from 30 μm to 1 μm . For the connection to electrodes embedded in the multifunctional fiber, the electrodes were exposed manually along the side wall of the fiber by using a blade and silver paint (SPI Supplies, USA). Then copper wires were wrapped around the fiber at each exposure locations along the fiber and the silver paint were applied for the fixation and lower resistance. The copper wires connected to fiber electrodes were soldered to the pin connector while a stainless-steel wire was also soldered as the ground wire for later extracellular recording. In addition, the 5-min epoxy (Devcon, ITW Performance Polymers, USA) was applied to the connection interface for strengthening affixation and better electrical insulation.

3.2.2 Impedance measurement

First, multifunctional fiber probes were prepared into two centimeters long and the embedded electrodes were electrically connected to the copper wire (connecting details in the above fabrication and integration section). The impedance Spectrum results were acquired via a potentiostat (Interface 1010E, Gamry Instruments). During the measurements, two-electrode experiments were performed with fiber probes as a working electrode, Pt wire (Basi) as $1 \times$ phosphate-buffered saline (PBS, Thermo Fisher) as electrolyte by an AC voltage of 10 mV (10 Hz–100 kHz).

3.2.3 Optoacoustic wave characterization

To generate the optoacoustic signal, a compact Q-switched diode-pumped solid-state laser (1030 nm, 3 ns, 100 μ J, repetition rate of 1.7 kHz, RPMC Lasers Inc., USA) was used as the excitation laser source. The laser was first connected to an optical fiber through a 200 μ m fiber coupling module and then connected to the mFOE with a SubMiniature version A (SMA) connector. The pulse energy was adjusted through a fiber optic attenuator (varied gap SMA Connector, Thorlabs, Inc., USA). The acoustic signal was measured through a homebuilt system including a needle hydrophone (ID. 40 μ m; OD, 300 μ m) with a frequency range of 1–30 MHz (NH0040, Precision Acoustics Inc., Dorchester, UK), an amplifier and an oscilloscope. The mFOE tip and hydrophone tip were both immersed in degassed water. The pressure values were calculated based on the calibration factor provided by the hydrophone manufacturer. The frequency data was obtained through a fast Fourier transform (FFT) calculation using the OriginPro 2019.

3.2.4 In vitro neurostimulation and calcium imaging

Oregon Green[™] 488 BAPTA-1 dextran (OGD-1) (ThermoFisher Scientific, USA) was dissolved in 20% Pluronic F-127 in dimethyl sulfoxide (DMSO) at a concentration of 1

mM as stock solution. Before imaging, neurons were incubated with 2 μ M OGD-1 for 30 min, followed by incubation with normal medium for 30 min. Q-switched 1030 nm nanosecond laser was used to generate light and delivered to mFOE. The pulse energy was adjusted through a fiber optic attenuator (varied gap SMA Connector, Thorlabs, Inc., USA). Notably, 1030 nm is far from the excitation peak of Oregon Green (494 nm) and pass band of emission filter (500-540 nm), therefore assuring no effect from direct excitation of OGD by any light leak from the fiber. A 3D translational stage was used to position the mFOE approaching the target neurons.

Calcium fluorescence imaging was performed on a lab-built wide-field fluorescence microscope based on an Olympus IX71 microscope frame with a 20 \times air objective (UPLSAPO20X, 0.75NA, Olympus, USA), illuminated by a 470 nm LED (M470L2, Thorlabs, USA), an emission filter (FBH520-40, Thorlabs, USA), an excitation filter (MF469-35, Thorlabs) and a dichroic mirror (DMLP505R, Thorlabs, USA). The converter area is visible and identifiable through the inverted microscope when the mFOE was placed close enough to the imaging plate. Image sequences were acquired with a scientific CMOS camera (Zyla 5.5, Andor, Oxford Instruments, UK) at 20 frames per second. The fluorescence intensities, data analysis, and exponential curve fitting were analyzed using ImageJ (Fiji) and MATLAB 2022.

3.2.5 Implantation surgery procedure

All surgery procedures complied with all relevant guidelines and ethical regulations for animal testing and research established and approved by Institutional Animal Care and Use Committee (IACUC) of Boston University (PROTO201800534). Eight to ten weeks old male wildtype C57BL/6-E mice (Charles River Laboratories, US) were received and allowed to acclimate for at least 3 days before enrolling them in experiments. All mice in experiments had access to food and water ad libitum and were kept in the BU animal facility maintained for 12-h light/dark cycle. During

the implantation surgery, mice were anesthetized by isoflurane (5% for induction, 1-3.5% during the procedure) and positioned on a stereotaxic apparatus (51500D, Stoelting Co., USA). After hair removal, a small incision was made by sterile surgery scalpel at the target region and then a small craniotomy was made by using a dental drill. Assembled mFOE was inserted into mice hippocampus (-2.0 mm AP, 1.5 mm ML, 2 mm DV) using the manipulator with respect to the Mouse Brain Atlas. The ground stainless steel wire was soldered to a miniaturized screw (J.I. Morris) on the skull. Finally, the whole exposed skull area was fully covered by a layer of Metabond (C&B METABOND, Parkell, USA) and dental cement (51458, Stoelting Co., USA). Buprenorphine SR was used to provide long effective analgesia after the surgery.

3.2.6 In vivo electrophysiology recording and optoacoustic stimulation

Extracellular recording was performed through an electrophysiology system (Molecular Devices, LLC, USA). mFOE electrodes were connected to the amplifier (Multiclamp 700B, Molecular Devices, LLC, USA) through the pin connector and headstages after the animals recovered from surgeries. The amplified analog signal was then converted and recorded by the digitizer (Digidata 1550, Molecular Devices, LLC, USA).

Q-switched 1030 nm nanosecond laser was used to generate light and delivered to mFOE. During the extracellular electrophysiological recording, the preset trigger signal was generated by the digitizer and used to trigger the Q-switch laser for optoacoustic stimulation. The pulse energy was adjusted through a fiber optic attenuator (varied gap SMA Connector, Thorlabs, Inc., USA).

Data analysis was performed with Matlab and OriginPro and custom scripts were used to analyse the local field potential and spike sorting. The raw extracellular recordings were first band filtered for local field potential results (LFP, $0.5 - 300$ Hz) and spike results ($300 - 5000$ Hz). A custom Matlab script was used to create

spectrograms to visually support the analysis of the LFPs in both the time domain and the frequency domain. The spike sorting algorithm was implemented through several steps: first, individual spike signals with length of 3 ms were picked up from the full recording through a standard amplitude threshold method; then the dimensionality of each spike signal was reduced via the principal component analysis (PCA) and unsupervised learning algorithms (K-means clustering) was used to separate out the clusters.

3.2.7 Foreign body response assessment via immunohistochemistry

To compare the tissue response, animals were implanted with a silica optical fiber (diameter = 300 μm , FT300EMT, Thorlabs, Inc, USA) and mFOE for 3 days or 4 weeks. Then at target timepoints, animals were euthanized and transcardially perfused with phosphate-buffered saline (PBS, ThermoFisher Scientific, USA) followed by 4% paraformaldehyde (PFA, ThermoFisher Scientific, USA) in PBS. The fiber probes were carefully extracted before the extraction and then the brains were kept in 4% PFA solution for one day at 4 °C. Brains were sectioned in the horizontal plane at 75 μm on an oscillating tissue slicer (OST-4500, Electron Microscopy Sciences). Free-floating brain slices were washed in PBS and blocked for 1 hour at room temperature in a blocking solution consisting of 0.3% Triton X-100 (vol/vol) and 2.5% goat serum (vol/vol) in PBS. After blocking, brain slices were incubated with the primary antibodies in the PBS solution with 2.5% goat serum (vol/vol) for 24 hours at 4 °C. Primary antibodies used included rat anti-GFAP (Abcam Cat. # ab279291, 1:500), chicken anti-NeuN (Millipore Cat. # ABN91, 1:500), and rabbit anti-Iba1 (Abcam Cat. # ab178846, 1:500). Following primary incubation, slices were washed three times with PBS for 10 min at room temperature. The brain slices were then incubated with secondary antibodies in the PBS solution with 2.5% goat serum (vol/vol) for 2 hours at room temperature. Secondary antibodies used included goat anti-rat

Alexa Fluor 488 (Abcam Cat. # ab150157, 1:1000), goat anti-rabbit Alexa Fluor 568 (Abcam Cat. # ab175471, 1:1000) and goat anti-chicken Alexa Fluor 647 (Abcam Cat. # ab150171, 1:1000). Slices were then washed three times with PBS for 10 min at room temperature. Before imaging, slices were stained with DAPI solution (1 $\mu\text{g}/\text{ml}$, Millipore, USA) for 15 minutes at room temperature. Perfusion, staining and mounting procedures were identical to all samples regardless of the implants.

All brain slices were prepared by using an oscillating tissue slicer (OST-4500, Electron Microscopy Sciences) with the same thickness of 75 μm controlled by the machine. Before imaging, stained brain slices were gently transferred on the cover glass by a brush without any folding. Perfusion, staining and mounting procedures were identical to all samples regardless of the implants.

All fluorescent images were acquired with a laser scanning confocal microscope (Olympus FV3000) with an air 20 \times objective and a numerical aperture $\text{NA} = 0.75$ unless otherwise noted. Regions centered on the wound induced by implants, i.e. mFOE or silica fibers, with the dimension of 650 $\mu\text{m} \times 650 \mu\text{m}$ were selected for later quantitative analysis. Neuron density was then calculated within the selected areas by counting NeuN labeled cell bodies using the cell counter plugin (ImageJ). Sample with obvious uneven neuron distribution (Figure 3.1) was excluded for comparison. Area analysis of Iba1 and GFAP labeled cells was performed by creating binary layers of the fluorescence images using the threshold function and quantified using the measurement tool (ImageJ Fiji). The IsoData algorithm⁸⁶ in ImageJ Fiji was used to unbiasedly determine the threshold value to distinguish the signal area from the background.

3.2.8 Statistical information

Data shown are mean \pm standard deviation. For the comparison on peak fluorescence change of in vitro optoacoustic stimulation, one-way ANOVA and Tukey's mean com-

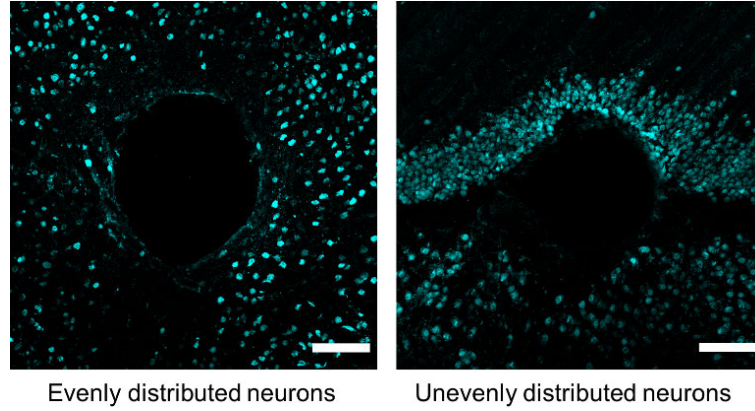


Figure 3-1: Confocal imaging of NeuN labelled neurons. At certain depth, NeuN labelled neurons are distributed unevenly because of the intrinsic structure of mice brain. For fair comparison, those samples were excluded from the later quantitative analysis. Scale bar: 100 μm .

parison test were conducted by using OriginLab. 15 stimulation events were compared for each condition. For the comparison of foreign body response between silica fiber and mFOE, $N > 8$ brain slices from 3 animals were analysed using one-way ANOVA and Tukey’s mean comparison test. The p values were determined as n.s.: nonsignificant, $p > 0.05$; *: $p < 0.05$; **: $p < 0.01$; ***: $p < 0.001$. Statistic analysis were conducted using OriginPro.

3.3 Results

3.3.1 Design, fabrication and characterization of mFOE

Towards bidirectional neural communication, we have designed the mFOE to utilize the optoacoustic stimulation as “writing” and electrophysiological recording as “reading” of the neural interface (Figure 3-2). Previously, fiber based optoacoustic emitters have been developed as a miniature invasive ultrasound transducer for the biomedical applications, such as intravascular imaging and interventional cardiology. (Colchester et al., 2014; Noimark et al., 2016) Recently, our work showed that fiber based optoacoustic emitters can also be applied to neural stimulation in vitro and in

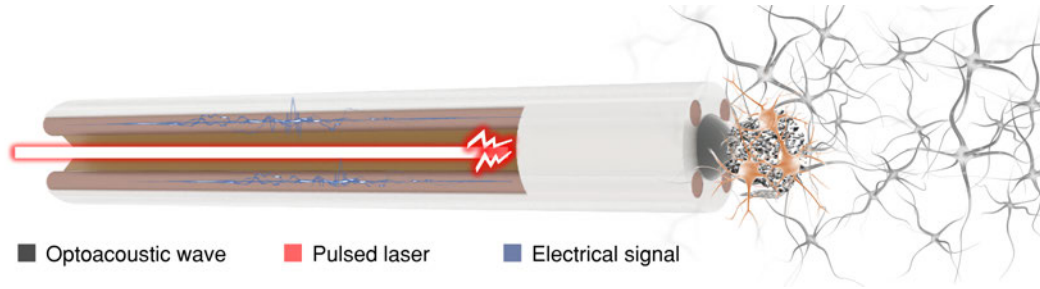


Figure 3.2: Schematic of mFOE for bidirectional communication with neurons. Input laser pulse (red) is used to generate optoacoustic waves (black mesh next to the emitter at the mFOE tip) by the emitter. Neural activities are recorded by embedded electrodes (brown) as the output electrical signal (blue). Neurons stimulated are highlight in the tan color, in contrast to the unstimulated neurons in the gray color.

vivo, with single neuron resolution and dual site capability. (Shi et al., 2021; Chen et al., 2022) In these studies, typically commercial silica fibers were used, together with optoacoustic coating. However, the silica fiber, with Young's modulus of 70 GPa, is mismatched with mechanical properties of native neural tissue (kilo- to megapascals) (Chen et al., 2017) and not easy to integrate with miniaturized electrodes for recording. In this study, we took advantage of the fiber fabrication method developed by Fink and Anikeeva, (Canales et al., 2015; Abouraddy et al., 2007) and utilized the polymer multifunctional fiber design as the base for the mFOE to delivering nanosecond laser to the optoacoustic coating and to record electrical signals. Specifically, a multifunctional fiber with a core optical waveguide and miniaturized electrodes was fabricated using the thermal drawing process (TDP) as previously reported (Figure 3.3). (Jiang et al., 2020a) The waveguide is made of polycarbonate core (PC, refractive index $n_{PC} = 1.586$, diameter = 150 μm) and polyvinylidene difluoride cladding (PVDF, refractive index $n_{PVDF} = 1.426$, thickness = 50 μm) as the core and the shell, respectively (Figure 3.4). The notable difference in the refractive index of those two materials facilitates efficient light transmission at 1030 nm (loss = 0.38 dB/cm, Figure 3.5a). Both polymer materials show a much lower young's modulus than the

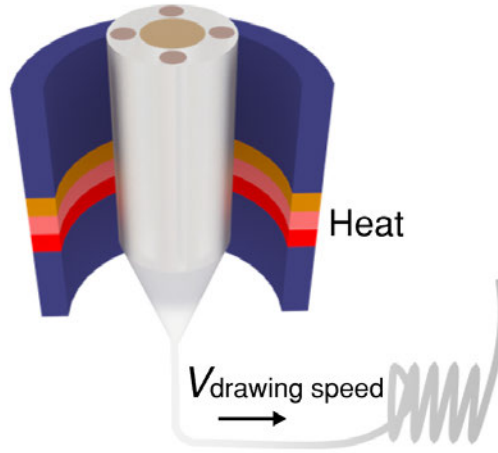


Figure 3-3: Illustration of the thermal drawing process.

commercial silica fiber (Table 3.1) and significantly reduced the bending stiffness to 60 N/m. (Jiang et al., 2020a) BiSn alloy is used in surrounding electrodes with diameters of 35 μm because of its conductivity and compatibility with TDP (Figure 3-4). As an implant device, the biocompatibility is also a critical factor when choose the electrode materials. Based on previous studies, bismuth and its alloy showed very low toxicity or even non-toxicity the animal and cell experiments. (Yi et al., 2014; He et al., 2021; Chen et al., 2023) This multifunctional fiber showed broadband transmission across the visible range to near infrared region (Jiang et al., 2020a; Guo et al., 2020) and sub-megaohm impedance at 1k Hz (Figure 3-6) when it has been prepared into a length about two centimetres.

Table 3.1: The Young's modulus of polymer materials used in mFOE (Vinogradov and Holloway, 1999; Khun and Liu, 2013) and the commercial silica optical fiber. (Holmes et al., 2022)

Materials	PVDF	PC	Silica
Young's Modulus (GPa)	2.5-2.7	2.3-2.6	70

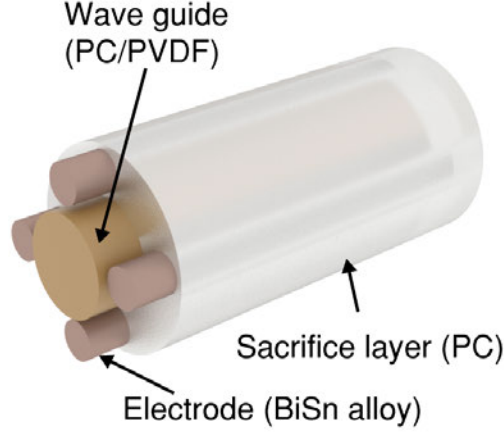


Figure 3.4: Components of the multifunctional fiber, including a PC/PVDF waveguide, BiSn alloy electrodes and PC sacrifice layer.

To integrate the optoacoustic converter to the multifunctional fiber, the optoacoustic coating, composed of light absorbers and thermal expansion matrix, needs to be selectively coated on the core waveguide distal end while keeping the surrounding electrodes exposed and conductive. Compared to our prior FOE fabrication using the dip-coating method, (Jiang et al., 2020b; Shi et al., 2021) here we took several innovative steps. First, a pressure-driven pico-liter injector was used to precisely deposit the optoacoustic materials to the core waveguide distal end. The coating area was controlled through varying the injection volume (0.1 – 0.5 nL), which is controlled by the regulated pressure (2-4 psi) over a set period of time (1-2 s, Figure 3.7) as described in Equation 3.1,

$$V = C \cdot d_{inner}^3 \cdot p \cdot t \quad (3.1)$$

where V is the injection volume, C is a constant attributed to the unit conversion factors, effects of liquid viscosity and the taper angle of micropipette, d_{inner} is the inner diameter of the pico-liter injector, p is the pressure, and t is the deposition time. Two 3D translational stages with stereo microscopes were used to precisely control the deposition localization. Second, instead of using carbon nanotubes (CNT),

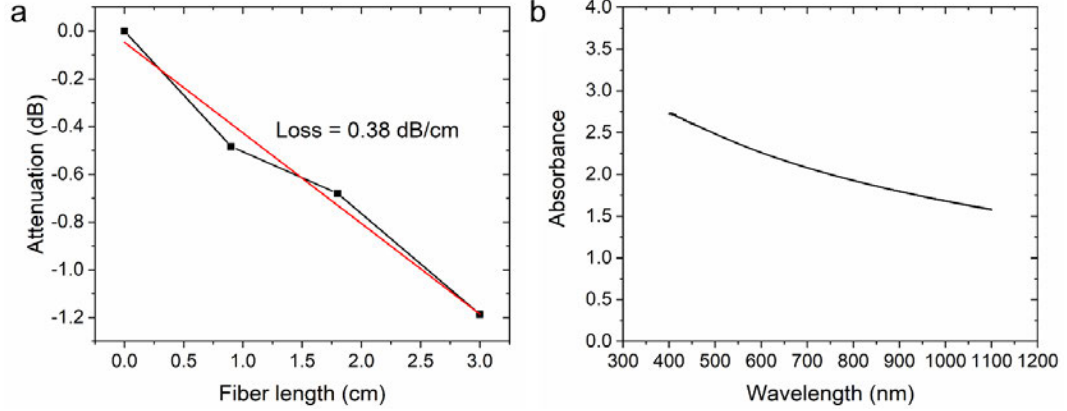


Figure 3-5: Optical properties of the waveguide and optoacoustic emitter of mFOE. a. The optical loss of waveguide measured at 1030 nm with the cut-back method. b. Vis-NIR absorption spectrum of CB/PDMS mixture.

we used carbon black (CB) embedded polydimethylsiloxane (PDMS) as the composite optoacoustic material. CB exhibited similar wideband light absorption (Figure 3-5b), (Han et al., 2011) assuring the sufficient photoacoustic conversion for neural stimulation. Importantly, due to its relative low viscosity, (Hilarius et al., 2013; Brigandi et al., 2017) CB/PDMS composite shows much higher injectability compared with CNT/PDMS, therefore more comparable to the pico-liter deposition process. Through these steps, we successfully coated 10-20 μm thick 10% w/w CB/PDMS composite onto the 150 μm diameter core waveguide distal end while electrodes were still exposed as shown in Figure 3-8. Collectively mFOE with the photoacoustic emitter and multiple electrodes has been successfully fabricated.

To characterize the optoacoustic performance of mFOE, a Q-switched 1030 nm pulsed nanosecond laser with repetition rate of 1.7 kHz was applied with pulse energies of 16.6 μJ , 27.3 μJ and 41.8 μJ , respectively. Each pulse was 3 ns and this short duration enabled the thermal and mechanical stress confinement during laser excitation, which was critical to the high efficient generation of optoacoustic waves. The generated acoustic waves were measured by a 40 μm needle hydrophone placed

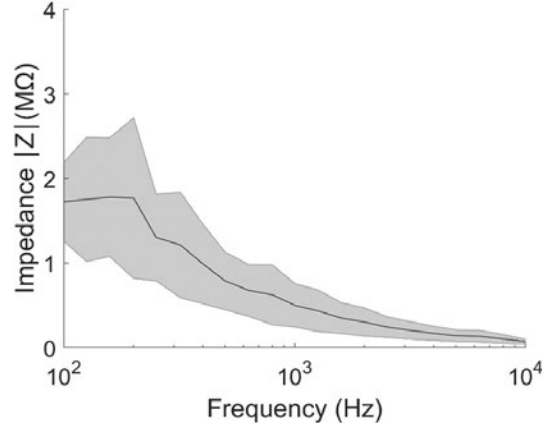


Figure 3-6: Impedance measurements of the BiSn electrodes in multifunctional fiber. Shaded areas and solid curve in the figure represent the standard deviation and mean value respectively.

at about 100 μm away from the fiber tip. The representative pulse acoustic pulse with a width of approximately 0.08 μs was generated by a single laser pulse as shown in Figure 3-9a. Higher input laser pulse energy led to larger acoustic pressure. A peak-to-peak pressure of 1.0, 1.6 and 2.3 MPa were measured with the pulse energy of 16.6, 27.3 and 41.8 μJ , respectively. The frequency spectrum shows the broadband characteristic of typical optoacoustic waves, (Lee et al., 2018) and the peak frequencies are around 12.5 MHz (Figure 3-9b). Based on our previous work, (Jiang et al., 2020b; Shi et al., 2021) we expected that such pressure and frequency is capable to successfully stimulate neurons in vitro and in vivo. To quantify the attenuation of the optoacoustic signal generated by the mFOE, we measured the pressure generated P using a hydrophone and plotted it as a function of distance x from the optoacoustic emitter (Figure 3-10). Results were fitted to a fitting curve $P = 0.92 \cdot \exp(-x/335.54) + 0.18$ ($R^2=0.976$). According to the fitting curve, the pressure of acoustic wave drops to $1/e$ of P_0 at the characteristic distance of 335 μm indicated by the attenuation constant. Considering the attenuation of acoustic wave in soft tissue such as brain is several folds larger than that in water due to the higher absorption and scattering

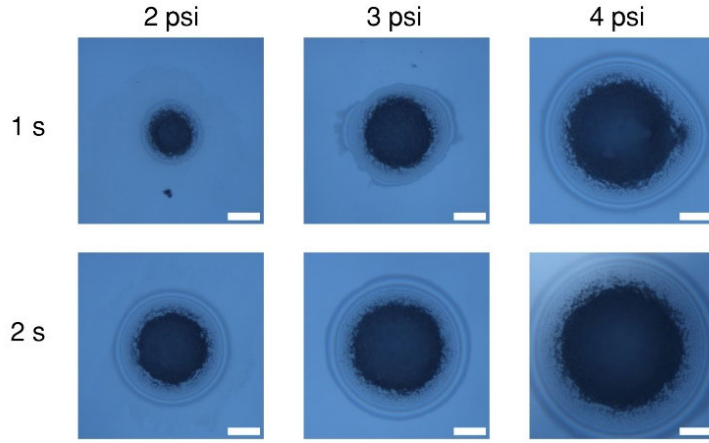


Figure 3-7: The coverage area was controlled through tuning the injection pressure and time. Injection time was varied between 1 second and 2 seconds, and the pressure was varied from 2 psi, 3 psi and 4 psi. Scale bar: 50 μm .

effect, (Wells, 1975) the acoustic wave generated by mFOE is expected to attenuate much faster, with a characteristic length much smaller than 335 μm in the brain tissue than that measured in water. Notably, a small electrode with a similar diameter of 100 μm shows attenuation of the electrical field at a characteristic distance of 100 μm . (Zhao et al., 2016) This suggests that photoacoustic stimulation could have a potential to provide at least a comparable spatial resolution. We also calculated the mechanical index (MI), a commonly used matrix, to evaluate the probability of mechanical damage due to ultrasound generated. The MI of acoustic waves generated by 2.3 MPa is 0.2 (calculation in the Appendix), lower than 1.9, the safety threshold suggested by the Food and Drug Administration (FDA) safety guidelines. (Şen et al., 2015)

3.3.2 mFOE stimulation of cultured primary neurons

To investigate mFOE can directly trigger the neuronal activity, we examined the response of cultured primary neurons under mFOE stimulation. Because of the presence of calcium channels in neuronal membrane and their activation during the depolar-

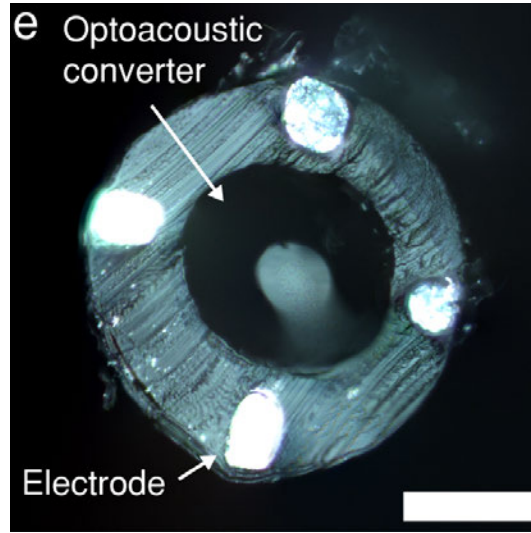


Figure 3-8: Top view microscope image of the mFOE. Scale bar: 100 μm .

ization, calcium imaging has been widely used to monitor the neuronal activities. (Smetters et al., 1999; Yang and Yuste, 2017) Here, we cultured and loaded the rat cortical neurons (days in vitro 10-14) with a calcium indicator, Oregon GreenTM 488 BAPTA-1 dextran (OGD-1)58, and performed the calcium imaging with an inverted wide-field fluorescence microscope (Figure 3-11). To perform the optoacoustic stimulation, mFOE was placed approximately 50 μm above the in-focus target neurons (Figure 3-12a) by a micromanipulator under the microscope. 1030 nm 3 ns pulsed laser with a repetition rate of 1.7 kHz was delivered to the mFOE through an optical fiber. The energy of laser pulse was 41.8 μJ , corresponding to a peak-to-peak pressure of 2.3 MPa generated. Lower energy was tested but did not induce calcium transient. The stimulation duration determined by each laser burst was 100 ms, corresponding to 170 pulses (Figure 3-13). By applying 5 bursts of laser pulses with interval of 1s, we investigated the reproducibility of the stimulation.

Using calcium imaging, we monitored the activities of all neurons in the field of view and divided them into two groups: groups within the converter area (Figure

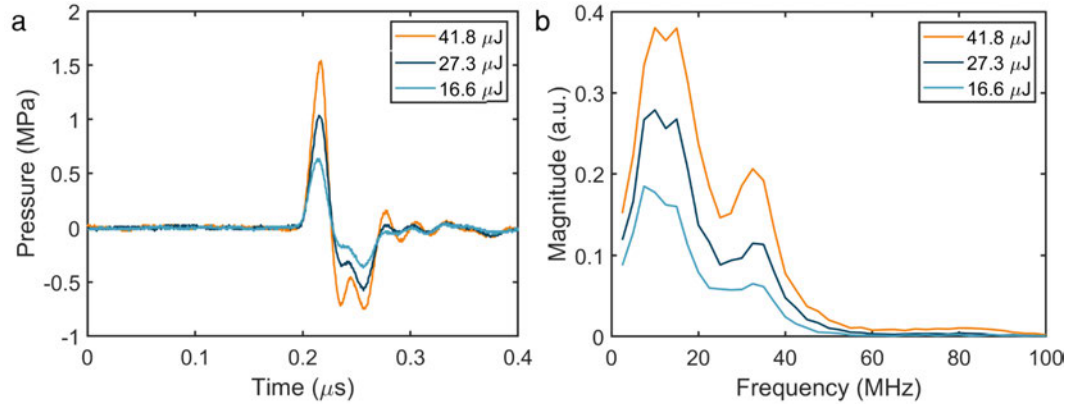


Figure 3-9: a. Representative acoustic waveforms under different laser pulse energy recorded by a needle hydrophone. b. Frequency spectrum of acoustic waveforms shown in a.

3-12b) and outside the converter area (Figure 3-12c). For neurons within the converter area, i.e. the 100 μm from the center of the mFOE, Figure 3-12b shows that 8 of 10 neurons showed successful and repeatable calcium transient ($\Delta F/F > 1\%$, the baseline standard deviation) corresponding to each stimulation. Calcium transients are also repeatable for each burst applied over the 1 s period, indicating the evoked neuronal activities and confirming the reliability of mFOE stimulation. For neurons outside the converter area, only 2 of 10 neurons responded. This result also suggested the mFOE with the 150 μm center waveguide with photoacoustic coating provided a spatial precision of $\sim 200 \mu\text{m}$ for stimulation in vitro. This observation is consistent with that fiber based optoacoustic converters generate a confined ultrasound fields with sizes comparable with the radius of converter. (Jiang et al., 2020b)

Next, to investigate the threshold of mFOE stimulation, we varied the stimulation duration from 5 ms, 50 ms, 100 ms to 200 ms on neurons in different cultures ($N = 15$) under the same laser pulse energy of 41.8 μJ and the same repetition rate of 1.7 kHz. mFOE stimulation with duration of 5 ms did not evoked any observable fluorescence change (n.s., $p > 0.05$) (Figure 3-12g). Only when the duration was 50 ms or longer, the mFOE successfully produced neural activation ($\Delta F/F > 1\%$, $p < 0.01$) as shown

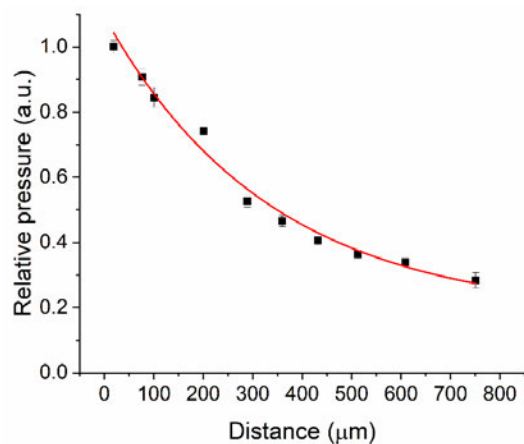


Figure 3-10: Attenuation curve of optoacoustic wave generated by mFOE along the axial direction. Relative pressure plotted as a function of the distance. Laser pulse energy was fixed at 41.8 μJ .

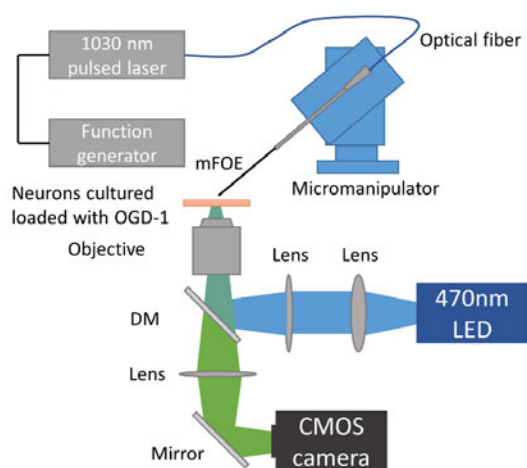


Figure 3-11: Schematic of in vitro mFOE stimulation and calcium imaging set up. Stimulation: 1030 nm pulsed laser is triggered by a function generator and delivered to the mFOE through an optical fiber. Calcium imaging: Oregon green is excited by 470 nm LED and the fluorescence signal is detected through a CMOS camera.

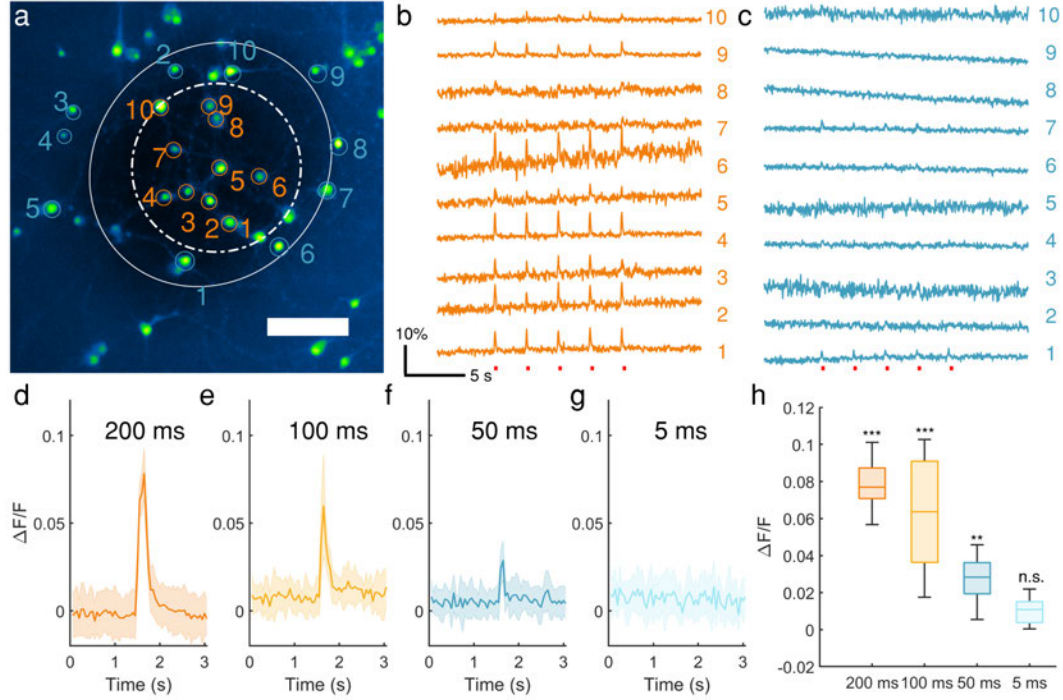


Figure 3-12: Calcium transients induced by mFOE in cultured primary neurons. a. Calcium image of primary cultured neurons loaded with OGD-1. Twenty neurons within (orange) and outside (blue) the optoacoustic converter area are circled and labelled. Scale bar: 100 μm . Solid circle: area outside the converter area; dashed line circle: area within the optoacoustic converter area. b-c. Calcium traces of neurons undergone repeated mFOE stimulations with a laser pulse train duration of 100 ms (red dots). Each pulse train was repeated 5 times. Colors and numbers of the traces are corresponding to the neurons labelled in a. d-g. Average calcium traces of neurons triggered by mFOE stimulation with durations of 200 ms (d), 100 ms (e), 50 ms (f) and 5 ms (g), respectively. Shaded area: the standard deviation (SD). N=15. h. Average maximum $\Delta F/F$ of neurons stimulated by mFOE. N = 15. (n.s.: non-significant, $p > 0.05$; *: $p < 0.05$; **: $p < 0.01$; ***: $p < 0.001$, One-Way ANOVA and Tukey's mean comparison test)

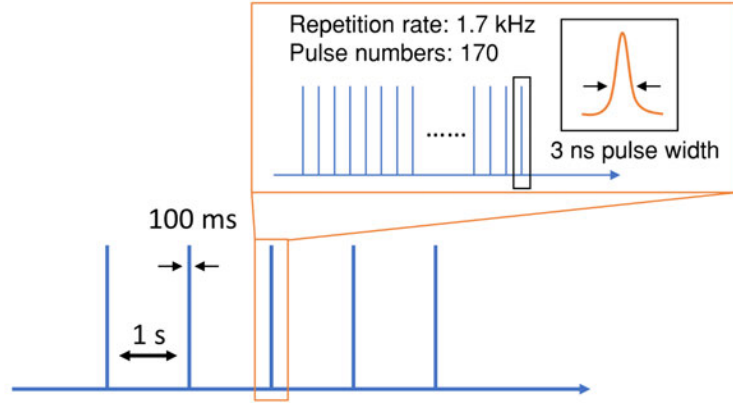


Figure 3-13: Illustration of the laser pulse train for 5 bursts with 100 ms duration at 1Hz.

in Figure 3-12d-f, and Figure 3-12h. Longer pulse durations leads to larger peak fluorescence changes, from $2.9 \pm 1.1\%$, $6.0 \pm 2.8\%$ to $7.8 \pm 1.3\%$ corresponding to 50 ms, 100 ms and 200 ms, respectively. For the longest stimulation duration of 200 ms tested, no obvious change on morphology or elevation of baseline fluorescence intensity was detected in neurons after multiple stimulations (Figure 3-14), indicating the safety of stimulation.

A laser only control experiment was also performed. Laser light with the same pulse energy of $41.8 \mu\text{J}$ and duration (200 ms, 100 ms and 50 ms) was delivered to OGD-1 loaded neurons through the multifunctional fiber but without optoacoustic coating. None of neuron cultures showed a detectable calcium response, distinct from the observed in mFOE stimulated neurons (Figure 3-15).

To evaluate the photothermal effect of the mFOE stimulation and its potential impact on neurons, we also characterized the thermal profile of the mFOE in PBS during the acoustic generation. Temperature was measured by an ultrafast thermal sensor with a sampling rate of 2000 Hz placed in contact with mFOE optoacoustic coating under the microscope. The laser conditions were consistent with neural stimulation test, i.e., the pulse energy was maintained at $41.8 \mu\text{J}$ and the burst duration

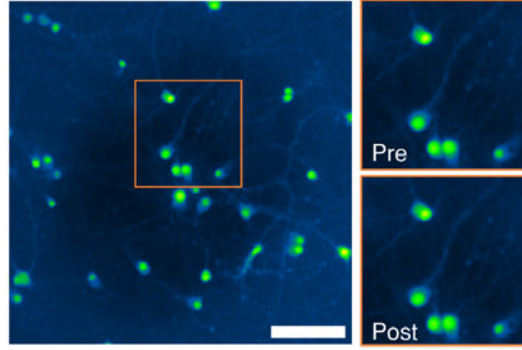


Figure 3.14: Calcium imaging of neurons before and after mFOE stimulation with duration of 200 ms. Neurons were subjected to repeated stimulation using mFOE with a duration of 200 ms, repeated five times. The morphology and calcium signal of the same field of view were subsequently imaged and compared. No obvious differences were observed. Scale bar: 100 μm .

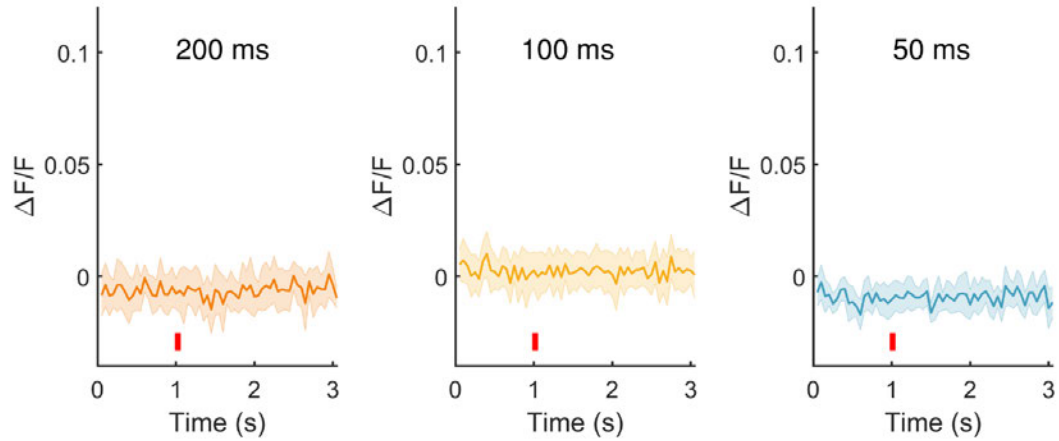


Figure 3.15: Average calcium traces of laser only control groups. The laser duration was same with three conditions tested in mFOE stimulation (200 ms, 100 ms and 50 ms). Laser light with pulse energy of 41.8 μJ was triggered at the time point labelled by the red bar. Shaded areas: standard deviation. (N=3)

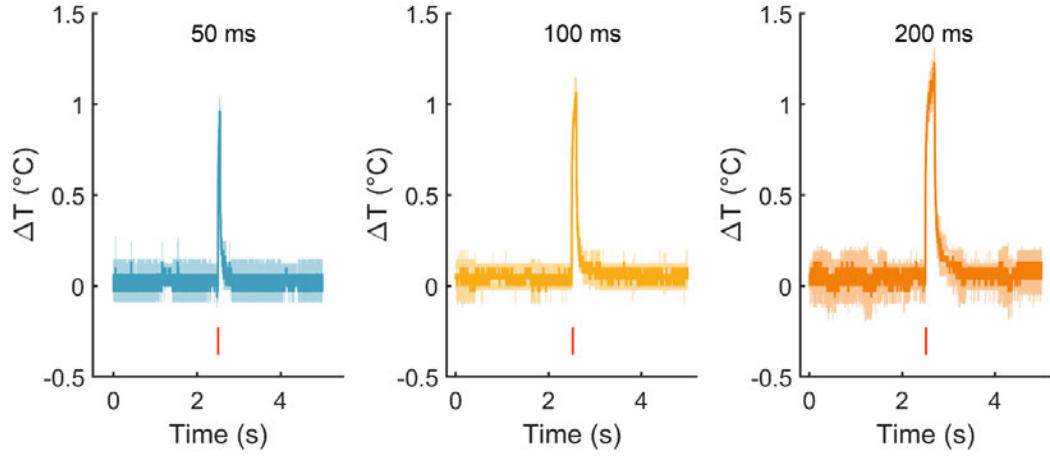


Figure 3-16: Temperature change of the optoacoustic emitter integrated on mFOE. The pulse energy was maintained at 41.8 μJ and the burst duration was varied from 50 ms (blue), 100 ms (yellow) to 200 ms (orange). Laser was trigger at 2.5 second as labelled by the red bar.

was varied from 50 ms, 100 ms to 200 ms. The temperature increase on the mFOE surface was found to be 1.23 ± 0.09 $^{\circ}\text{C}$, 1.07 ± 0.08 $^{\circ}\text{C}$, 0.96 ± 0.08 $^{\circ}\text{C}$ for 200, 100, 50 ms laser durations, respectively (Figure 3-16). Such temperature increase is far below the previously reported threshold of thermal-induced neural stimulation ($\Delta T > 5$ $^{\circ}\text{C}$). (Shapiro et al., 2012; Lyu et al., 2016) In addition, a recent study by Kim et al. shows that small temperature increases of 1 $^{\circ}\text{C}$ caused transient suppression of neurons. (Kim et al., 2022) This also proves that the temperature effect is not the main contributor to the neuronal response induced by mFOE. Taken together, we conclude that activation of neurons was due to the mFOE optoacoustic stimulation.

3.3.3 In vivo simultaneous optoacoustic stimulation and electrophysiological recording

Since the animal experiment is a significant part of the study in neuroscience and neurological diseases, we further investigated the performance of mFOE in the wild type C57BL/6J mice. In vivo optoacoustic stimulation was performed by delivering pulsed laser to the implanted mFOE, and the optoacoustically stimulated neuronal

activities were recorded through electrodes in the mFOE (Figure 3-17a). Experimentally, we implanted the mFOE into the hippocampus of mice ($N = 5$). The chronically implanted mFOE allows mice to move freely after surgery (Figure 3-17b). During stimulation and recording tests, the mFOE was coupled with the laser source and electrophysiological recording headstage through the standard ferrule and pin connector, respectively. The stimulation and recording were conducted in the mice under continuous anesthesia induced and maintained by isoflurane. Based on the threshold of optoacoustic stimulation obtained in *in vitro* studies, 50 ms bursts of laser pulses with a pulse energy of 41.8 μJ were delivered to the mFOE at 1Hz during the 5 second treatment period. The simultaneous electrophysiological recording by mFOE electrodes was bandpass filtered to examine the local field potential (LFP, 0.5-300 Hz). Simultaneous optoacoustic stimulation and electrophysiological recording were performed at multiple time points, including 3 days, 7 days, 2 weeks and 1 month (Figure 3-17c-f). Three out of five mice tested showed successful simultaneous stimulation and recording functions for testing periods of 3 days to one month.

The evoked brain activities corresponding to the optoacoustic stimulation were confirmed by monitoring the LFP response. LFP response at two weeks after implantation was detected with latency of 7.19 ± 2.29 ms ($N = 15$, from three mice). The amplitude of LFP response varied at four time points. The largest and smallest responses occurred at 2 weeks and 1 month, respectively. The decreased response observed after 1 month can be attributed to multiple factors. For example, the formation of glial scar around the implanted electrodes can not only block the propagation of electrical signals but also push neurons away from the optoacoustic emitter of mFOE. Both reduce the intensity of the LFP response. Further optimization of the electrode surface coating could improve the reliability of the recording interface. (Kozai et al., 2015; Eles et al., 2017) These results collectively demonstrate the relia-

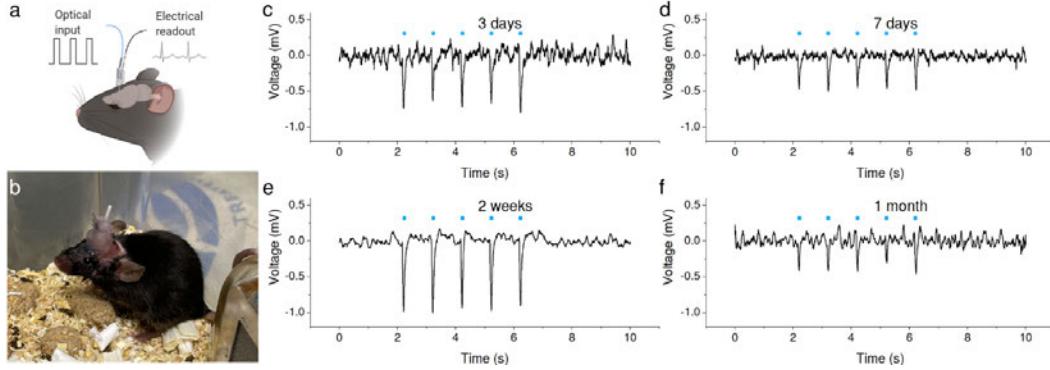


Figure 3-17: a. Illustration of the mFOE enabled bidirectional neural communication using laser signal as input and electrical signal as readout. b. mFOE was implanted into hippocampus of a wild type C57BL/6J mouse. c-f. Simultaneous optoacoustic stimulation and electrophysiological recording performed at 3 days (c), 7 days (d), two weeks (e) and one month (f) after implantation. Blue dots the laser pulse trains. For each laser train: 50 ms burst of pulses, pulse energy of 41.8 μ J, laser repetition rate 1.7 kHz.

bility of the optoacoustic stimulation and recording functions of the implanted mFOE in the animals.

To eliminate the possibility that LFP response was induced by electrical noise or laser artifacts, we also conducted two sham control experiments. In the light only control group, we implanted a multifunctional fiber without optoacoustic coating to the mouse hippocampus and delivered the laser light with the same condition. The LFP recorded didn't correlate to the laser pulse train, indicating the spontaneous brain activities were recorded and light only did not invoke the LFP response (Figure 3-18a). In the dead brain control group, we tested the optoacoustic stimulation through mFOE implanted to the euthanized mouse and did not observe the corresponding LFP response (Figure 3-18b). These results collectively confirm the signals we detected from mFOE stimulation were not artifacts.

We further evaluated the recording performance of implanted mFOE. To evaluate the ability of mFOE for recording spike activity, the electrophysiological signals

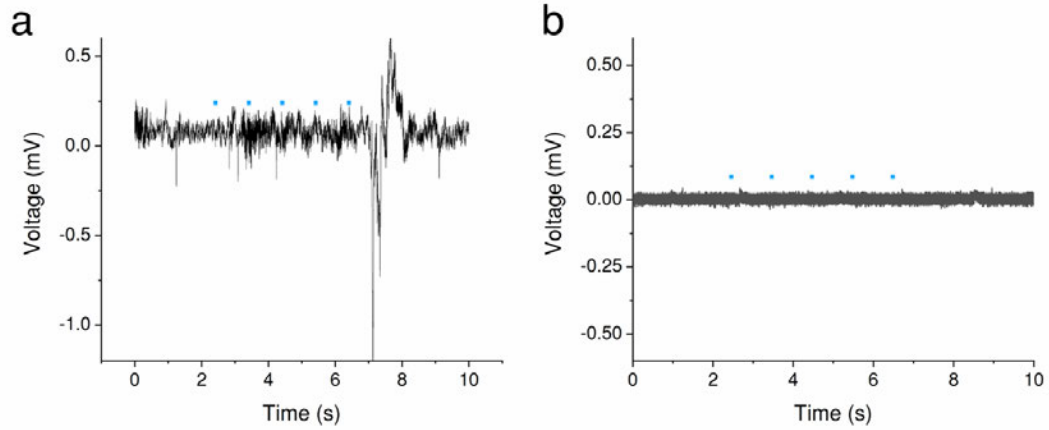


Figure 3-18: LFP recording of sham control stimulation experiments. a. Electrophysiological recording under light only stimulations delivered through a bare multifunctional fiber without optoacoustic emitter. b. Simultaneous optoacoustic stimulation and electrophysiological recording of a euthanized mouse. Same laser condition was used: pulse energy of 41.8 μJ , 50 ms burst of pulses, 1 Hz, blue dots indicate the laser onset.

recorded were first bandpass filtered (0.5-3 kHz, Figure 3-19a). Through a principal-component analysis (PCA) based spike sorting algorithm, two spike clusters can be isolated from an endogenous neural recording (3-19b). The cluster quality was assessed by two common measures⁶³, Lratio and isolation distance. Lratio is 0.0017 and isolation distance has the value of 99.37. Both of them are comparable to the prior reported value of the spike recording with good cluster-separation quality. (Canales et al., 2015; Park et al., 2017; Jiang et al., 2020a) The first averaged spike shape (3-19c) showed a narrower and larger depolarization than that of the second spike shape (3-19d). The different spike waveform and the cluster analysis suggested that the action potentials were recorded from at least two different groups of neurons. (Heinricher, 2004; Henze et al., 2000) Thus, the successfully clustered neural activities from CA3 confirmed the ability of mFOE electrodes for the spike recording.

To examine the sensitivity of LFP recording, at one month after implantation we

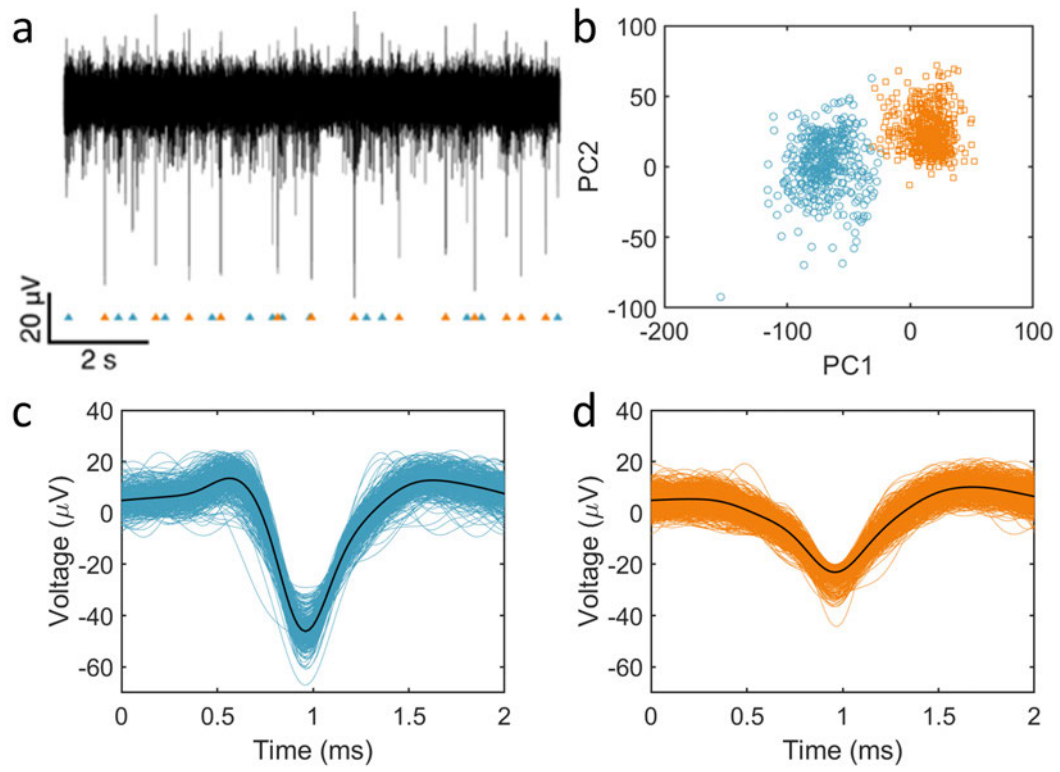


Figure 3.19: a. Part of the filtered spontaneous activity containing two separable group of spikes recorded by mFOE electrode at one month after implantation. b. Principal-components analysis (PCA) of the two group of spikes. c-d. Waveform of two group of spikes in b.

altered the anesthesia level via adjusting the induced isoflurane concentration during the recording to see if the characteristic anesthesia dosage-dependent changes can be observed (Figure 3-20a). Initially, a low level of anesthesia was maintained at 0.5% v/v isoflurane, and recorded LFP showed that spontaneous brain activities occurred continuously (i in Figure 3-20a and Figure 3-20b). Then a higher-level anesthesia (3% v/v isoflurane) was applied for 3 minutes. After the isoflurane level was increased, some spontaneous brain activities were suppressed and a hyperexcitable brain state was induced, where the voltage alternation (bursts) and isoelectric quiescence (suppression) appeared quasiperiodically (ii in Figure 3-20a (Jiang et al., 2020a; Ching et al., 2012) and Figure 3-20c). With maintaining 3% v/v isoflurane, a deep anesthesia state was induced in the animal. At the same time, both respiration rate and responsiveness to toe pinch decreased due to the higher anesthetic level.

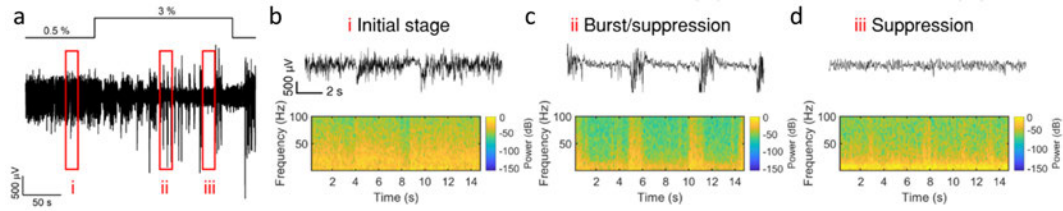


Figure 3-20: a. Local field potential (LFP) recorded by mFOE one month after implantation with an alternating anaesthesia level (0.5-3% v/v isoflurane). b-d. different LFP responses induced by varying the concentration of isoflurane: b corresponds to the initial stage (0.5% of isoflurane level); c corresponds to the burst/suppression transition stage (after increasing the isoflurane level to 3%); d corresponds to the suppression stage (the isoflurane level was maintained at 3% and took effect).

Less voltage alternation occurred and for the most of time the LFP signal was a flat line (suppression, iii in Figure 3-20a and Figure 3-20d). Compared with initial stage, γ band LFP activity in 30-100 Hz was decreased due to the higher concentration of isoflurane as shown in the power spectrum (Figure 3-20d). (Hudetz et al., 2011) Later, when the concentration of isoflurane was reduced to 0.5% v/v again, the LFP activity

returned to a similar level as measured in the initial stage. Taken together, this isoflurane dosage-dependent characteristic confirmed the accuracy of LFP recording by mFOE.

3.3.4 Foreign body response comparison between mFOE and standard optical fiber using immunohistochemistry

Foreign body response is a critical property of implantable neural interface to assure their usage in a safe and chronic way, since the physical insertion into brain tissue commonly initiates a progressive inflammatory tissue response. (Kozai et al., 2015) To evaluate the biocompatibility of mFOE, we compared the foreign body response of mouse brain to mFOE with the similar size standard silica optical fibers (diameter = 300 μm), which is widely used in optogenetic technologies. (Aravanis et al., 2007; Ung and Arenkiel, 2012) The immunohistochemistry analysis of surrounding brain tissue was performed from mice ($N = 3$) implanted with the mFOE and a conventional silica fiber 3 days and 1 month after implantation (Figure 3-21a). The damage to surrounding neurons from implant was assessed through evaluating neuronal density using the neuronal nuclei (NeuN) markers (Figure 3-21b). Number of neurons was calculated by counting the NeuN-positive cells per field of view ($650 \times 650 \mu\text{m}$). The presence of ionized calcium-binding adaptor molecule 1 (Iba1, Figure 3-21c) and glial fibrillary acidic protein (GFAP, Figure 3-21d) were used as the markers for activated microglia and astrocytic response, respectively.

Compared with the silica fiber, mFOE induced significantly less microglial response ($p < 0.01$, Figure 3-21c, f) and astrocyte reactivity ($p < 0.001$, Figure 3-21d, g), but no significant difference was observed on the neuronal density (Figure 3-21b, e) 3 days after implantation. A decrease in foreign body response, specifically, higher neuronal density and lower microglia and astrocytic response (Figure 3-21e-g), was observed from 3 days to 1 month after implantation of both mFOE and silica fiber

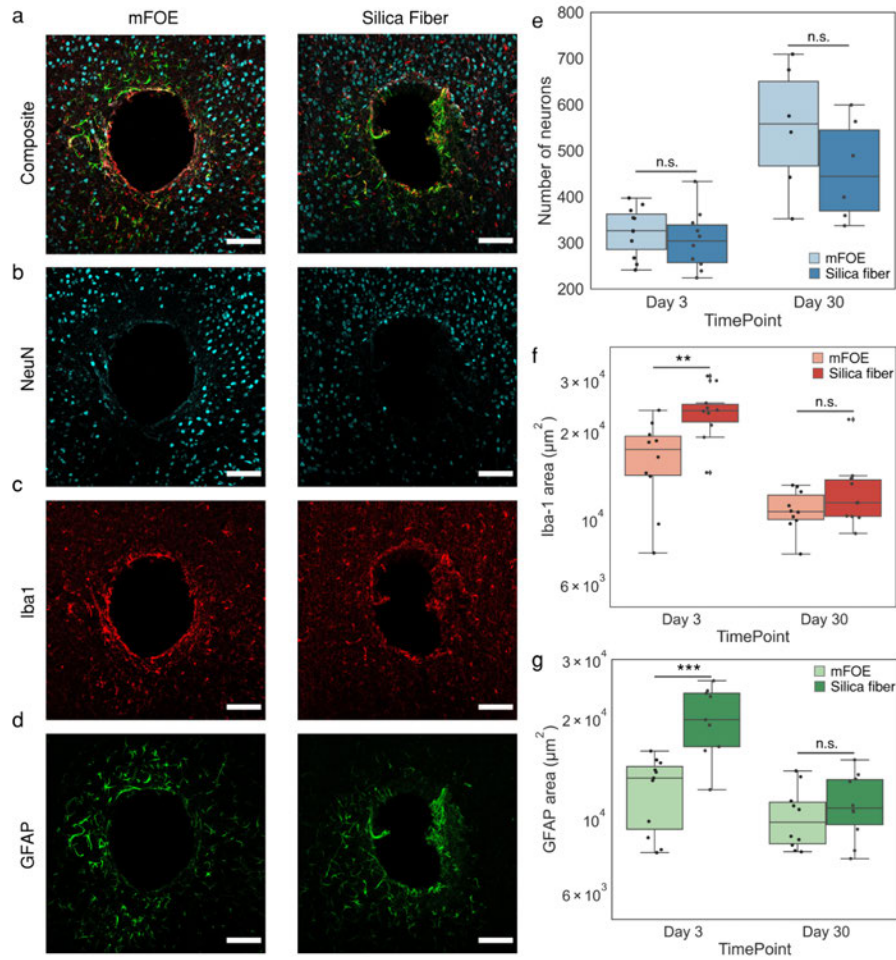


Figure 3-21: Foreign body response comparison of mFOE and silica fiber using immunohistochemistry. a-d. Immunohistochemistry images of mouse brains implanted with mFOE and silica fiber one month after implantation (N = 3). Scale bar: 100 μm . Brain slices were labelled with the neuron-specific protein (NeuN, cyan), ionized calcium-binding adaptor molecule 1 (Iba1, red) and glial fibrillary acidic protein (GFAP, green). e. Number of neurons in the field of view, calculated by counting the NeuN-positive cells for mFOE and silica fiber at 3 days and 1 mon after implantation. f. Microglial reactivity, assessed by counting the Iba-1 labelled area, for mFOE and silica fiber at 3 days and 1 mon after implantation. g. Astrocyte reactivity, assessed by counting the GFAP labelled area, for mFOE and silica fiber at 3 days and 1 mon after implantation. For each experimental group, two to four brain slices were used from each mouse (N = 3). (n.s.: non-significant, $p > 0.05$; **: $p < 0.01$; ***: $p < 0.001$, One-Way ANOVA and Tukey's mean comparison test)

and no significant difference was observed between mFOE and silica fiber 1 month after implantation. Taken together, the immunohistochemistry analysis confirmed that mFOE yielded less foreign body response in the short period, i.e., 3 days, after implantation and showed similar biocompatibility with silica fiber at longer implantation time, i.e., 1 month.

3.4 Discussion

In this study, we designed and developed a miniaturized fiber-based device, i.e. mFOE, for bidirectional neural communication. mFOE performs the “write” function, i.e. non-genetic optoacoustic stimulation and the “read” function, i.e. simultaneous electrophysiological recording. The broadband acoustic wave with a broadband ultrasound pulse with pulse width about $0.1\ \mu\text{s}$ and a center frequency at 12.5 MHz and a peak pressure of 2.3 MPa with pulse numbers > 85 generated by mFOE successfully stimulate neurons with a spatial resolution of approximately $200\ \mu\text{m}$ in primary rat cortical neuron culture. By implanting mFOE into mouse hippocampus, we demonstrated its ability for simultaneous optoacoustic stimulation and electrophysiological recording and superior biocompatibility as a chronic bidirectional neural interface. Reliable stimulation and LFP recording have been achieved up to one month post implantation. Recording quality has been demonstrated by the spike recording.

For the first time, combining this pico-liter deposition and thermal fiber pulling, we successfully integrated an optoacoustic converter to the polymer multifunctional fiber. Different from the conventional dip-coating method, (Colchester et al., 2014; Poduval et al., 2017) the selective deposition through micro-injection allows the easy fabrication of optoacoustic emitter in a volume and position-controlled way. Through the selective deposition, the dimension of optoacoustic emitter is no longer limited by the tip sizes of optical fibers. Our choice of CB/PDMS composite as the optoacoustic

material is also essential as it is comparable with this deposition process with a fine volume control at pico liter level. Besides the application in neural interface, such design and fabrication method can also be applied to optical ultrasound probes used in imaging, (Noimark et al., 2016; Finlay et al., 2017) for example, in the tip engineering and the integration to photonics crystal fibers.

We introduced the optoacoustic stimulation as a new strategy for “writing” in the bidirectional neural interface. Compared with previous optoelectrode devices based on optogenetics (Canales et al., 2015; Vöröslakos et al., 2022; Jiang et al., 2020a) and photothermal, (Yoo et al., 2013; Abaya et al., 2012b) the non-genetic optoacoustic stimulation enabled by mFOE reduces the barrier of transgenic techniques for applications in primate and potentially human, and avoids the thermal toxicity. At the same time, it offers the spatial precision benefit from the confined ultrasound field. It is orthogonal to electrical recording, therefore minimizing crosstalk with electrical recording. As an emerging neuromodulation method, the mechanism of optoacoustic stimulation is still not fully understood. In addition to the micropore formation and cavitations, (Plaksin et al., 2014; Krasovitski et al., 2011) more recent studies also indicated that mechanosensitive ion channels are responsible for the activation of neurons. (Yoo et al., 2022; Shi et al., 2022)

Bidirectional brain interfaces are important research tools to understand brain circuits, potential treatments for neurological disease and bridges to brain computer interface for broad applications. In addition to electrical recording, there are other modalities for recording neural activity in the brain, (Vázquez-Guardado et al., 2020) such as fiber photometry, calcium imaging with a Gradient-Index (GRIN) lens, and microdialysis providing orthogonal ways to record neural activity in the brain. However, due to their disadvantages in temporal resolution and ease of integration, these modalities have not yet replaced electrophysiology recording, the gold standard

method “reading” from brain in bidirectional neural interfaces.

New features of mFOE compared to the previous fiber-based interface, such as non-genetic and non-electrical stimulation are critical to advance many applications. For example, closed-loop neuromodulation has been demonstrated to be superior to the conventional open-loop system, as it can achieve more responsive and real-time control over neural dynamics. In neurological diseases treatment, combining the detection and in situ intervention improves the treatment effectiveness and safety. Because of its bidirectional capabilities, mFOE has the potential to be used as a new brain interface with closed-loop capability. Using epilepsy as an example, the implantation of mFOE into seizure foci enables continuous LFP recording. This recording can serve as a guide for localized optoacoustic stimulation, allowing for timely intervention at the early stage before the initial seizure activity progresses into a severe seizure. Such capabilities are also desirable in the application of closed-loop stimulation. For conventional electrical stimulation system, various tools were developed to remove the stimulation artifacts from the recording signal in real time. (Nie et al., 2021; Dastin-van Rijn et al., 2021) However, they are still limited by the issues on the temporal delay, (Oyama and Itiki, 2010) complex design, (Stanslaski et al., 2012) and higher hardware resource needed for the computationally intensiveness. The unique orthogonal non-electrical optoacoustic stimulation and electrical recording avoids electrical artifacts from stimulation appearing in the recording signals, potentially offering a simpler design for the closed-loop strategy.

In comparison of the optoelectrodes fabricated through semiconductor fabrication process, the recording and stimulation sites of the current mFOE design is fixed at the core waveguide and the number of channels is limited because of the nature of multifunctional fiber. Some post processing methods have been proposed to tackle this challenge, like the laser micromachining technique. (Jiang et al., 2020a) It is

possible to further engineer the fiber to offer multiple and selective stimulation sites. (Pisanello et al., 2014) Additionally, while the utilization of soft polymer material (Sui et al., 2022; Park et al., 2015b) is effective in reducing the bending stiffness compared to silica fiber, the implementation of novel design strategies, such as incorporating a hydrogel matrix, (Park et al., 2021) can further enhance flexibility, softness, and biocompatibility, making it more suitable for long-term applications. With the further development of multifunctional fiber strategy, we believe the bandwidth of mFOE would be improved and open more opportunities in the research of neuroscience and neurological diseases.

Chapter 4

Photoacoustic Neuromodulation in Disease Treatments

By developing the photoacoustic materials introduced in the preceding chapters, we have addressed two critical gaps in the field of photoacoustic neuromodulation: material mismatch and simultaneous recording capabilities. The introduction of these new materials offers significant advantages for the application of photoacoustic neuromodulation in the treatment of neurological and neurodegenerative diseases. Unlike conventional fiber-based devices, the flexible photoacoustic film provides conformal contact with curved nerve structures, including the brain cortex, retina, and nerve bundles, thereby enabling enhanced stimulation efficacy. Moreover, its soft mechanical properties ensure a biocompatible neural interface, crucial for long-term chronic applications where mechanical mismatch can trigger foreign body responses. Additionally, the capability of simultaneous recording, when combined with photoacoustic stimulation, provides real-time feedback on the effectiveness of the stimulation. This feedback empowers researchers and clinicians to optimize the stimulation conditions and fine-tune parameters to achieve desired outcomes. In certain neurological diseases such as epilepsy or Parkinson's disease, the recorded signals can serve as triggers and feedback signals to achieve the desired brain state.

In this chapter, we present two demonstration applications as examples. The first application showcases the use of the flexible photoacoustic film to stimulate the degenerated retina, thereby restoring vision. In the second application, the bidirectional

photoacoustic emitter demonstrates its potential in the prevention of epilepsy.

4.1 Application in Retinal Degenerative Diseases

Before delving into the specific application of the flexible photoacoustic film for retinal stimulation, it is important to understand the background of the retina. In a healthy retina, multiple layers of neurons work together to convert light into action potentials. Photoreceptors, located at the top layer, play a crucial role in this process by converting light into neural signals. These signals are then transmitted through bipolar cells and ganglion cells, ultimately reaching the visual cortex, where they are processed and interpreted. However, in cases of degenerated retina, the gradual loss of photoreceptors leads to a progressive reduction in the patient’s visual field, affecting either the central or peripheral vision, depending on the specific disease. Conventional medication treatments often struggle to reverse this process, making alternative strategies necessary.

One such strategy involves external stimulation of the retina. Early pioneering works have demonstrated the feasibility of this approach using photovoltaic devices. By utilizing light as the medium for stimulation, these devices eliminate the need for electrical connections and can mimic natural vision during eye movements. However, one limitation of photovoltaic devices is their inherent current leakage, which restricts their spatial resolution regardless of the electrode size. In contrast, photoacoustic stimulation offers higher spatial resolution. It is also a light-mediated technique but with superior capabilities. Thus, based on these advantages, we propose the hypothesis that retinal stimulation enabled by the soft photoacoustic film can serve as an improved method for treating retinal degenerative diseases.

4.1.1 Introduction to Retinal Regenerative Diseases (RRDs)

The eye is an intricate and remarkable organ, responsible for the conversion of visual light into biological signals that the brain interprets, allowing us to perceive the world around us. A large patient population exist around the world with blindness and vision impairments. The dysfunction or death of photoreceptors leading to retinal neurodegeneration is a significant contributor to incurable vision loss. Age-related macular degeneration (AMD) and retinitis pigmentosa (RP) are two major types of RRDs. Both of disease affect a large population in the world.

AMD is one of the leading causes of blindness in people over 60 years of age in developed countries and is projected to reach almost 280 million by 2040. (Wong et al., 2014; Lim et al., 2012) Both genetic and lifestyle factors are contributing to the AMD. Because the various contributing factors, the population of AMD is one of the most diverse and widespread group. The symptoms of AMD share similarities with the aging process. Patients with AMD have symptoms, including the progressive loss of photoreceptors, thickening of the Bruch's membrane, choroidal thinning, and formation of hard drusen. (Ardeljan and Chan, 2013) For late stage of AMD, the size and distribution of drusen can continue to enlarge and cause loss of RPE and photoreceptor cells.

RP is another RDD affection a large group of population. It is estimated to affect 1 in 4000 individuals totaling over 2 million individuals worldwide. (Sorrentino et al., 2016) Unlike AMD, the age of onset for RP can range from infancy to late middle age, with individuals experiencing severe visual impairments typically detected between the ages of 40 and 50. (Parmeggiani, 2011) The RP patients experience the disease progression from the loss of night vision to the tunnel vision, due to the development of rod and cone degeneration. More than one fourth of patients become legally blind (20/200) and 0.5% become completely blind in both eyes. (Grover et al., 1999)

Because RP vision deficits are due to photoreceptor degeneration through apoptosis, it's irreversible and hard to be treated through conventional medication methods.

4.1.2 Retinal Degenerative Disease Model

To study the retinal disorders characterized by the progressive degeneration of photoreceptor cells, P23H rat model is a commonly used animal model. It has been created by incorporation of a mutated mouse rhodopsin (Rho) transgene in the wild-type (WT) Sprague Dawley rat. (Orhan et al., 2015) Rats with the P23H mutation exhibit several key characteristics similar to human RP, including photoreceptor cell degeneration, progressive loss of vision, and morphological changes in the retina. These rats typically develop symptoms of retinal degeneration at an early age, making them valuable for studying the underlying mechanisms of the disease and testing potential therapeutic interventions.

The P23H rat model has been extensively utilized to investigate the efficacy and safety of various treatment strategies, such as gene therapy, cell transplantation, and pharmacological interventions. Researchers can assess the effectiveness of these interventions by evaluating visual function, retinal structure, and biochemical changes in the P23H rats. Similarly, for external retinal stimulation, P23H is also a commonly used animal model to investigate the performance of the stimulation method. For instance, Sekirnjak et al. investigated the electrical stimulation in the P23H degenerated retina model and found the ganglion cells of P23H rat showed similar response to electrical stimulation as wild-type ganglion cells. (Sekirnjak et al., 2009) Ronzani et al. developed a film of TiO_2 nanotubes and demonstrated its ability to drive the blind retina under UV flash light by using P23H blind retina model. (Ronzani et al., 2018) Inspired by the previous studies, we also chose the P23H rat model to evaluate the performance of photoacoustic film in the degenerated retina.

4.1.3 Experimental Methods

Photoacoustic film preparation

To prepare the photoacoustic film, a composite of 15% multi-wall carbon nanotubes (VWR, MFCD06202029) and 85% polydimethylsiloxane (10:1 weight ratio, Dow Corning Corporation, Sylgard 184) were used as the photoacoustic material. The mixture was spincoated on a cover glass and heated in an oven to 60 °C for 2.5 hours to get fully cured before being removed from the glass substrate.

Multichannel electrode recording of P23H degenerated retina

Experiments were conducted in accordance with the National Institutes of Health Guide for the Care and Use of Laboratory Animals. The animal experiments were performed in Vision Institute, France. Retinal pieces were flattened on a dialysis membrane and placed on an MEA (electrode diameter, 30 μm ; spacing, 100 μm ; MEA256 100/30 iR-ITO, MultiChannel Systems) coated with poly-D-lysine (0.1%, Sigma), with retinal ganglion cells facing the electrodes. Ames' medium (Sigma) bubbled with 5% carbon dioxide, oxygen balanced gas were supplied through the perfusion system. For photoacoustic stimulation, a 1030 nm Q-switch laser with a pulse width of 3 ns was delivered to the photoacoustic film through a multimodal optical fiber with 200 μm core diameter (Thorlabs Inc.). The position of fiber was controlled through a 3D motorized stage. From retinal ganglion cells recordings with a 252 channel preamplifier and MCRack (MultiChannel Systems), spikes were recorded and detected through the amplitude threshold method.

4.1.4 Results

Our research, conducted in collaboration with our French counterparts, focuses on restoring vision for patients with retinal degenerative diseases. To accomplish this,

we utilized the P23H rat strain, which serves as a reliable model for studying retinal degeneration, closely mirroring the characteristics observed in human retinitis pigmentosa.

In our study, we specifically investigated the efficacy of the CNT/PDMS photoacoustic film for retinal stimulation. The P23H rat retina was extracted and placed on the MEA with ganglion cells facing electrodes. The photoacoustic film was attached to the retina on the photoreceptor side as shown in Figure. 4-1. To generate the photoacoustic waves for retinal stimulation, a pulse laser was delivered through a optical fiber and the position was controlled by a 3D manipulator.

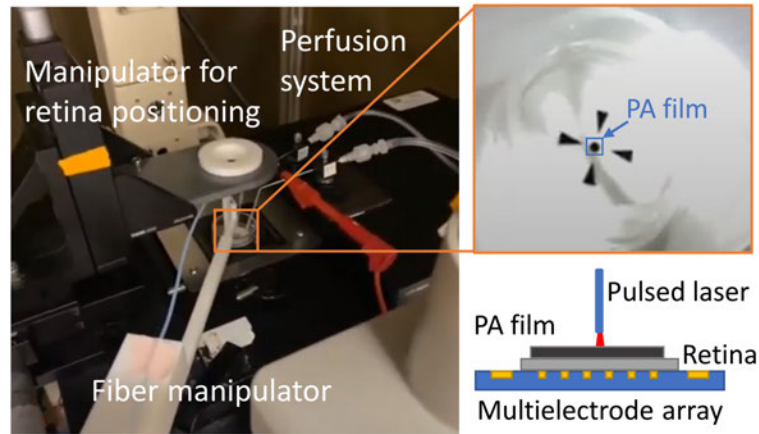


Figure 4-1: Image of MEA recording setup. Two manipulator were used to control the position of retina and fiber. Ames’s medium was supplied through the perfusion system. The response of ganglion cells under photoacoustic stimulation was recorded during the experiment.

The results were promising, as the photoacoustic stimulation robustly elicited neural activity in the ganglion cells that were targeted as shown in Figure. 4-2a-b. The recorded two groups of spikes could be attributed to both direct stimulation and indirect upstream signaling pathways. Pulse energy was about 14 μJ and the laser pulse train is shown in Figure. 4-2c. These findings demonstrate the potential of the soft photoacoustic film as a viable method for retinal stimulation in the context of retinal degenerative diseases.

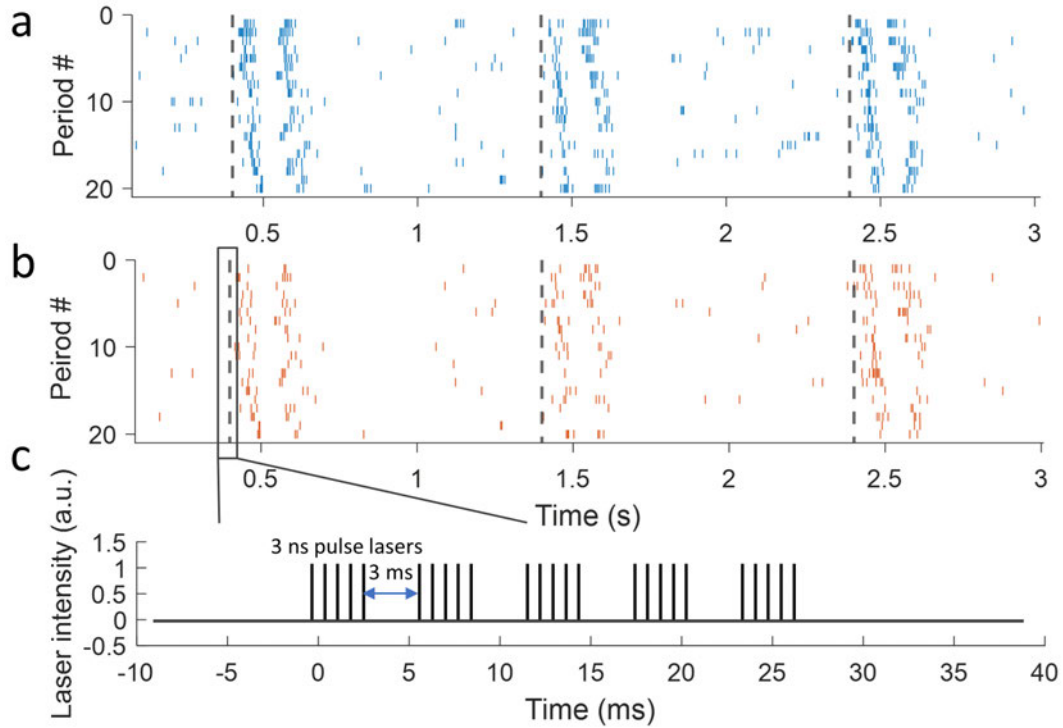


Figure 4.2: a-b. Ganglion cells response under repeated photoacoustic stimulation recorded from two separate channels. c. Schematic of laser pulse train. In total of fifteen pulses were delivered as 5 groups. The gap between each group was 3 ms.

Moreover, the film's ability to induce neural activity in the degenerating retina holds significant implications for developing therapeutic interventions aimed at restoring vision in affected individuals. By leveraging the unique properties of the photoacoustic film, we are hopeful that our research will contribute to the advancement of vision restoration strategies for patients with retinal degenerative diseases.

4.2 Application in Epilepsy

Epilepsy is a neurological disorder characterized by recurrent seizures, which are abnormal electrical discharges in the brain. Approximately 50 million people in the world are afflicted by the active seizure. (Johnson et al., 2019) These seizures can vary in frequency, duration, and intensity, and they can significantly impact an in-

dividual’s quality of life. Epilepsy can affect people of all ages, from children to older adults, and it can be caused by various factors such as genetics, brain injuries, infections, or developmental disorders. Despite significant advancements in medical treatments for epilepsy, it is estimated that approximately 35% of individuals with epilepsy still develop drug-resistant epilepsy (DRE). Traditional surgical approaches for drug-resistant epilepsy involve the removal or disconnection of epileptic brain tissue, which has shown to be effective in reducing seizures for certain patients with intractable epilepsy. (Al-Kaylani et al., 2007) However, the surgical removal add extra risk to the patients and may induce adverse effects. In addition, many patients are not eligible for the surgery, because the suspect seizure foci is diffuse, poorly-localized, or in regions associated with a high risk. (Spencer and Huh, 2008) An alternative treatment option is urgently needed. Neuromodulation offers another strategy with reversible and adjustable nature. Studies demonstrated that deep brain stimulation, responsive neural stimulation, and vagus nerve stimulation are safe and effective neurostimulation therapies used to treat refractory epilepsy. (Foutz and Wong, 2022) Therefore, we hypothesize that photoacoustic stimulation can also play a role in the seizure treatment as a neuromodulation approach.

4.2.1 Epilepsy Disease Model

Among the patient of epilepsy, partial epileptic disorders represent 60% of their cases, with temporal lobe epilepsy (TLE) being the most common type. The kainic acid model is a widely used animal model of TLE. Kainic acid is a potent neuroexcitatory substance which is a cyclic analog of l-glutamate and an agonist of ionotropic KA receptors. When kainic acid is injected into the brain, it induces seizures that mimic many of the characteristics of human TLE. This model is commonly used in laboratory research to study the underlying mechanisms of TLE and to test potential treatments for the condition.

In the kainic acid model, kainic acid is typically injected directly into specific brain regions associated with temporal lobe structures, such as the hippocampus (Raedt et al., 2009; Carriero et al., 2012) and amygdala (Dunleavy et al., 2010). The injection leads to excessive neuronal activity and the development of spontaneous recurrent seizures over time. These seizures can be monitored and characterized using electroencephalography (EEG), allowing researchers to study the progression of the disease and evaluate the efficacy of interventions. It's important to note that while the kainic acid model shares some similarities with human TLE, it does not fully replicate the complex nature of the human condition. Therefore, findings from this model need to be interpreted with caution and confirmed in other models or human studies. Nonetheless, the kainic acid model remains a valuable tool in epilepsy research, contributing to our understanding of the mechanisms underlying temporal lobe epilepsy and aiding in the development of new treatments. (Lévesque and Avoli, 2013)

4.2.2 Experimental Methods

Kainic acid induced TLE model

Mice were injected with KA or phosphate buffered saline into the right dorsal hippocampus. In brief, C57/BL6 mice were deeply anesthetized (5% isoflurane for induction, 2% isoflurane for maintenance) followed by a stereotaxic injection of 50 nL of either 10, 15, or 20 mM KA solution (Tocris, Bristol, UK) in sterile phosphate buffered saline or injection of saline only. Stereotaxic coordinates relative to bregma were: anteroposterior (AP) = -2.0 mm, mediolateral (ML) = 1.5 mm, and relative to the cortical surface: dorsoventral (DV) = 2 mm. Following KA injection the occurrence of a epileptic brain activity was verified.

4.2.3 Results

We tested the application of bidirectional optoacoustic fiber in epilepsy models- kainic acid induced temporal lobe epilepsy. We investigated the utility of the recording ability in the epilepsy monitoring. In the kainic acid epilepsy model, we injected 50 nL of 20 mM KA solution and implanted the bidirectional optoacoustic fiber to the same location in mice hippocampus to record the brain activity before and after the KA injection.

Figure. 4-3 shows an example of EEG recording obtained by the implanted bidirectional optoacoustic emitter. The fiber probe detected several electrographic features associated with KA-induced seizure, including pre-ictal spiking, the gradual evolution of spike amplitude and frequency during the ictal phase, as well as post-ictal spiking and post-ictal suppression. During the preictal phase, the fiber probe captured instances of preictal spiking. These abnormal neuronal activities, manifested as epileptic spikes, occurred prior to the onset of seizures. The spikes were observed to vary in frequency and amplitude. Throughout the ictal phase, the amplitude and frequency of spikes exhibited a gradual evolution. Initially, low-amplitude, high-frequency discharges were recorded, which gradually transformed into high-amplitude, low-frequency spikes or rhythmic activity as the seizure progressed. Additionally, the fiber probe identified post-ictal suppression, which denotes a period of relative electrical silence or reduced neuronal activity immediately after the seizure. This transient state was characterized by a decrease or absence of epileptic spikes or abnormal activity in the recorded EEG signals.

We investigated the histology of the mice brain 5 days after the KA injection to evaluate the neuropathological change. The hippocampus is highly susceptible to neuropathological changes following local administration of KA. Previous study demonstrated that administration of KA preferentially destroys the CA3 and CA4

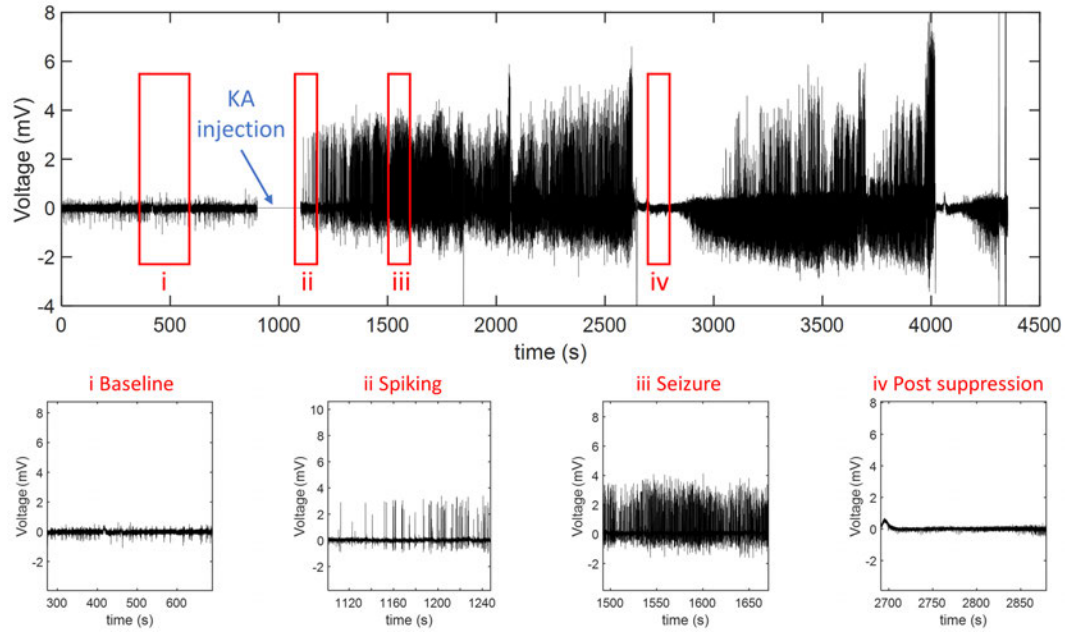


Figure 4-3: An example of electrographic recording by a fiber probe implanted in the hippocampus of KA injected mouse is shown. Various stages of mouse behavior before, during and after convulsive seizure are identified in red rectangles and the corresponding magnified traces are depicted below: baseline (non-ambulatory physiological stage), pre-ictal spiking (periodic electrographic discharges before or during seizure initiation), seizure (high frequency spikings during fully generalized tonic-clonic seizure), post-ictal spiking (periodic electrographic discharges immediately after seizure), and post-ictal suppression (behavioral arrest following convulsive seizure).

regions of the hippocampus but leaves the CA1 region and the dentate gyrus almost intact. (Lancaster and Wheal, 1982) In our results, in addition to inducing epileptic activities, the KA injection also resulted in observable gliosis at the injection site compared to the contralateral side as shown in Figure. 4-4. This gliosis confirmed that the KA injection not only triggered epileptic activities but also led to pathological changes in the brain tissue.

Overall, various electrographic features and the neuropathological change associated with seizures demonstrated the successful epilepsy induction through KA injection.

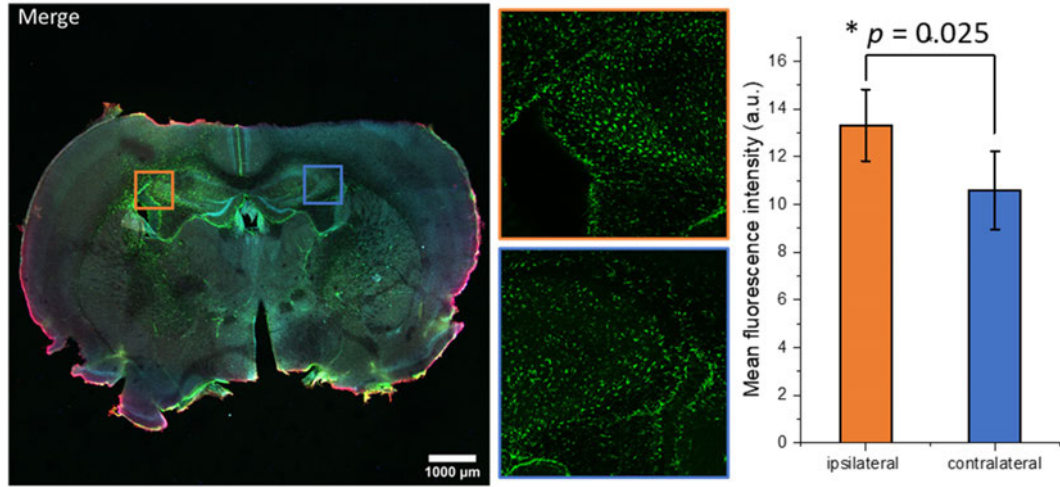


Figure 4-4: Gliosis in the hippocampus following Intrahippocampal administration of KA. Brain slice with thickness of 100 μm was stained by anti-GFAP to visualize the astrocyte distribution.

Next, we aimed to investigate the potential preventive effect of low-frequency photoacoustic stimulation on seizure activity. Prior studies utilizing optogenetics have suggested the efficacy of low-frequency stimulation in preventing seizures. (Paschen et al., 2020) In order to test this hypothesis, we conducted experiments on mice 21 days after inducing spontaneous seizure-like activity through KA injection.

During the 30-minute experiment session, the stimulation group received 2 minutes of low-frequency (0.5 Hz) photoacoustic stimulation at the beginning, while the control group did not receive any external stimulation. As shown in Figure. 4-5, our findings indicated that the control group mice exhibited a higher level of spontaneous seizure-like activity characterized by more high-load/medium-load spontaneous activity. In contrast, the mice in the stimulation group displayed reduced levels of spontaneous activity.

These results suggest that low-frequency photoacoustic stimulation may have a preventive effect on the occurrence of severe seizure activity. By providing targeted stimulation at a specific frequency, it is possible to modulate neural activity and

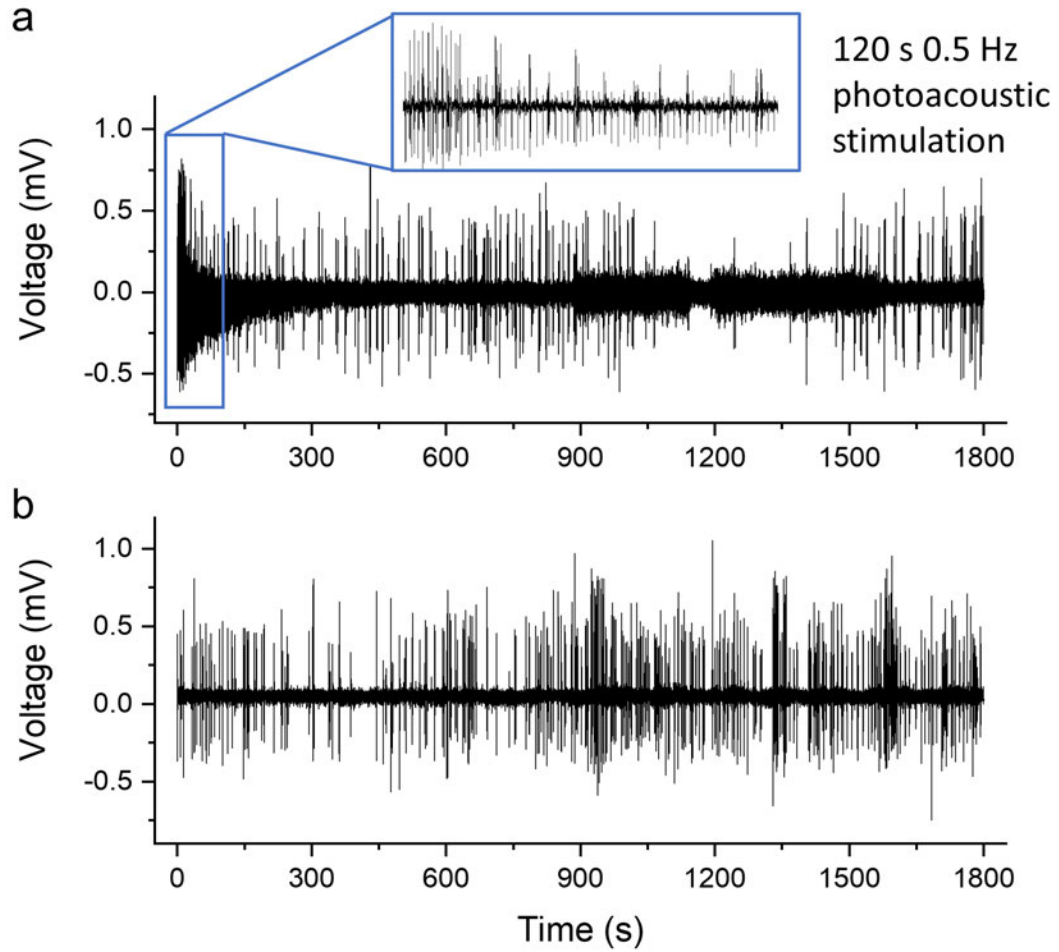


Figure 4.5: Representative EEG recording of 30 minutes experiment session. a. Stimulation group: KA injected mice received 2 minutes of low-frequency (0.5 Hz) photoacoustic stimulation at the session beginning. b. Control group: The spontaneous epileptic activity of KA injected mice. No external stimulation was provided.

potentially mitigate the development of seizures. These findings contribute to the growing body of evidence supporting the potential therapeutic applications of low-frequency stimulation in epilepsy research. The use of photoacoustic stimulation in this study provides a novel method to influence neural activity and potentially intervene in the progression of seizures. Further, it demonstrated the advantage of the spontaneous recording capability in epilepsy study and treatment, which enables an efficient monitoring on the epileptic activity.

Chapter 5

Conclusion and Outlook

5.1 Conclusion

Our research has successfully addressed two significant gaps in the field of photoacoustic neuromodulation: one is the mismatch between the physical properties of photoacoustic materials and neural structures, and the need for simultaneous recording capability. The dedicated efforts allowed us to explore the potential of photoacoustic materials for neuromodulation as a neural interface and applications in diseases treatment, such as vision restoration and epilepsy prevention.

Specifically, we introduced a biocompatible silk fibroin scaffold embedded with CNTs for photoacoustic stimulation and neural regeneration. The flexible photoacoustic material addresses the challenge posed by the incompatibility of fiber-based photoacoustic emitters with curved neural tissue. The incorporation of CNTs into the silk matrix provided structural support for tissue growth, while the embedded CNTs absorbed NIR light and transduced it into acoustic energy, stimulating neural activity and promoting neurite outgrowth. This scaffold-based approach using PA biomaterials presents a new neural interface, offering the potential for non-invasive neural stimulation and regeneration.

In addition, we focused on the development of a multifunctional fiber-based optoacoustic emitter (mFOE) as a bidirectional brain interface. The mFOE integrated optical waveguides and multiple electrodes within a single fiber, enabling simultaneous non-genetic neural stimulation and electrical recording of neural activities. Through

in vitro and in vivo experiments, the mFOE demonstrated its reliability in stimulating and recording neurons, establishing a stable and biocompatible neural interface. The bidirectional capabilities of the mFOE open new avenues for studying brain circuits and hold promise for closed-loop neural stimulation and brain-machine interfaces.

In the last part, we presented two demonstration applications to showcase the potential of optoacoustic neuromodulation technique. The first application focused on using a flexible photoacoustic film to stimulate the degenerated retina and restore vision. Promising results were observed, demonstrating the potential of the film for retinal stimulation in the context of retinal degenerative diseases. The second application explored the use of the bidirectional optoacoustic fiber for epilepsy prevention. By recording brain activity in a kainic acid-induced epilepsy model, the fiber showed utility in monitoring and preventing epileptic seizures.

Collectively, our research highlights the versatility and potential of optoacoustic techniques in various neural applications. The combination of biocompatible scaffolds, fiber-based neural interfaces, and targeted stimulation opens up new possibilities for neural modulation and regenerative medicine. Moreover, the demonstrated applications in vision restoration and epilepsy prevention emphasize the clinical relevance and translational potential of optoacoustic approaches.

5.2 Outlook

Future research in this field should concentrate on refining and optimizing optoacoustic technologies, expanding their applications to larger animal models, and eventually to human subjects. For instance, while a flexible film is desirable for implantation on curved neural tissue, such as the retina, the current implantation process remains invasive and may not be feasible for devices with large volumes. A potential solution to this clinical challenge is the use of injectable materials. These synthetic or nat-

ural materials rapidly transform from a liquid to a gel state upon injection into the target area, seamlessly integrating with the host tissue. The injection process allows for the delivery of the photoacoustic interface with minimal invasiveness. Moreover, once the injected neural interface forms the intended structure, it remains stable. The strategy has been investigated and developed in the other biomedical field, like tissue scaffold (Alonso et al., 2021; Macaya and Spector, 2012) and drug delivery. (Liu et al., 2022) Incorporating this advanced concept can significantly accelerate the clinical translation of optoacoustic materials.

The potential of advanced closed-loop control has been demonstrated in numerous previous studies. The simultaneous recording capability of mFOE establishes a foundation for future closed-loop photoacoustic neuromodulation. However, further exploration is required to fully realize its potential. Moreover, incorporating functions such as a microfluidic channel into the fiber-based optoacoustic emitter can enable chemical signaling, which plays a vital role in neural communications. In neuroscience research, *in situ* fluid injection allows researchers to chemically modulate the brain state, while deep brain drug delivery addresses the challenge posed by the blood-brain barrier in clinical applications.

In summary, photoacoustic neuromodulation is a novel yet promising technique. However, it still faces several challenges compared to existing methods. Each challenge represents an opportunity to enhance its performance and expedite its translational application. Investigating the functionality, long-term stability, biocompatibility, and scalability of this technique will be pivotal for its successful clinical implementation. The findings presented in this dissertation contribute to the growing body of knowledge in photoacoustic neuromodulation and offer insights for future advancements in the field.

Appendix A

Appendix

A.1 Mechanical Index Calculation

The mechanical index (MI) is a unitless metric commonly used in the field of ultrasound imaging.¹ It provides an indication of the potential bioeffects when the tissue is exposure to a certain ultrasound field. Both the intensity and frequency of the ultrasound waves are taken into account. It's defined as the peak negative pressure divided by the square root of the center frequency of the ultrasound wave. It is represented by the equation:

$$MI = \frac{P_-}{\sqrt{F_c}} \quad (\text{A.1})$$

Where P_- is the peak negative pressure of the ultrasound wave (MPa) and F_c is the center frequency of the ultrasound pulse (MHz). For the ultrasound with pressure of 2.3 MPa generated by mFOE, the peak negative pressure is -0.72 MPa and the central frequency is 12.5 MHz. Therefore, the MI is calculated as $0.72 \text{ MPa} / \sqrt{12.5 \text{ MHz}} = 0.2$.

References

- Abaya, T., Blair, S., Tathireddy, P., Rieth, L., and Solzbacher, F. (2012a). A 3d glass optrode array for optical neural stimulation. *Biomedical optics express*, 3(12):3087–3104.
- Abaya, T., Diwekar, M., Blair, S., Tathireddy, P., Rieth, L., Clark, G., and Solzbacher, F. (2012b). Characterization of a 3d optrode array for infrared neural stimulation. *Biomedical optics express*, 3(9):2200–2219.
- Abouraddy, A., Bayindir, M., Benoit, G., Hart, S., Kuriki, K., Orf, N., Shapira, O., Sorin, F., Temelkuran, B., and Fink, Y. (2007). Towards multimaterial multifunctional fibres that see, hear, sense and communicate. *Nature materials*, 6(5):336–347.
- Al-Kaylani, M., Konrad, P., Lazenby, B., Blumenkopf, B., and Abou-Khalil, B. (2007). Seizure freedom off antiepileptic drugs after temporal lobe epilepsy surgery. *Seizure*, 16(2):95–98.
- Al-Majed, A. A., Brushart, T. M., and Gordon, T. (2000a). Electrical stimulation accelerates and increases expression of bdnf and trkb mrna in regenerating rat femoral motoneurons. *European Journal of Neuroscience*, 12(12):4381–4390.
- Al-Majed, A. A., Neumann, C. M., Brushart, T. M., and Gordon, T. (2000b). Brief electrical stimulation promotes the speed and accuracy of motor axonal regeneration. *Journal of Neuroscience*, 20(7):2602–2608.
- Alles, E. J., Noimark, S., Zhang, E., Beard, P. C., and Desjardins, A. E. (2016). Pencil beam all-optical ultrasound imaging. *Biomedical optics express*, 7(9):3696–3704.
- Alonso, J. M., Andrade del Olmo, J., Perez Gonzalez, R., and Saez-Martinez, V. (2021). Injectable hydrogels: From laboratory to industrialization. *Polymers*, 13(4):650.
- An, Y. and Nam, Y. (2021). Closed-loop control of neural spike rate of cultured neurons using a thermoplasmonics-based photothermal neural stimulation. *Journal of Neural Engineering*, 18(6):066002.
- Anderson, J. M., Rodriguez, A., and Chang, D. T. (2008). Foreign body reaction to biomaterials. In *Seminars in immunology*, volume 20, pages 86–100. Elsevier.

- Andoy, N. M. O., Jeon, K., Kreis, C. T., and Sullan, R. M. A. (2020). Multifunctional and stimuli-responsive polydopamine nanoparticle-based platform for targeted antimicrobial applications. *Advanced Functional Materials*, 30(40):2004503.
- Ansari, R., Zhang, E. Z., Desjardins, A. E., and Beard, P. C. (2018). All-optical forward-viewing photoacoustic probe for high-resolution 3d endoscopy. *Light: Science & Applications*, 7(1):75.
- Antonini, M.-J., Sahasrabudhe, A., Tabet, A., Schwalm, M., Rosenfeld, D., Garwood, I., Park, J., Loke, G., Khudiyev, T., Kanik, M., et al. (2021). Customizing mri-compatible multifunctional neural interfaces through fiber drawing. *Advanced Functional Materials*, 31(43):2104857.
- Aravanis, A. M., Wang, L.-P., Zhang, F., Meltzer, L. A., Mogri, M. Z., Schneider, M. B., and Deisseroth, K. (2007). An optical neural interface: in vivo control of rodent motor cortex with integrated fiberoptic and optogenetic technology. *Journal of neural engineering*, 4(3):S143.
- Ardeljan, D. and Chan, C.-C. (2013). Aging is not a disease: distinguishing age-related macular degeneration from aging. *Progress in retinal and eye research*, 37:68–89.
- Asteriti, S., Liu, C.-H., and Hardie, R. C. (2017). Calcium signalling in drosophila photoreceptors measured with gcamp6f. *Cell Calcium*, 65:40–51.
- Audouard, E., Rousselot, L., Folcher, M., Cartier, N., and Piguet, F. (2021). Optimized protocol for subcutaneous implantation of encapsulated cells device and evaluation of biocompatibility. *Frontiers in Bioengineering and Biotechnology*, 9:620967.
- Bansal, A., Shikha, S., and Zhang, Y. (2022). Towards translational optogenetics. *Nature Biomedical Engineering*, pages 1–21.
- Bell, A. G. (1880). On the production and reproduction of sound by light. *American journal of science*, 3(118):305–324.
- Benfenati, F. and Lanzani, G. (2021). Clinical translation of nanoparticles for neural stimulation. *Nature Reviews Materials*, 6(1):1–4.
- Benfenati, V., Stahl, K., Gomis-Perez, C., Toffanin, S., Sagnella, A., Torp, R., Kaplan, D. L., Ruani, G., Omenetto, F. G., Zamboni, R., et al. (2012). Biofunctional silk/neuron interfaces. *Advanced Functional Materials*, 22(9):1871–1884.
- Bettinger, C. J., Cyr, K. M., Matsumoto, A., Langer, R., Borenstein, J. T., and Kaplan, D. L. (2007). Silk fibroin microfluidic devices. *Advanced Materials*, 19(19):2847–2850.

- Bloch, E., Luo, Y., and da Cruz, L. (2019). Advances in retinal prosthesis systems. *Therapeutic advances in ophthalmology*, 11:2515841418817501.
- Brigandi, P. J., Cogen, J. M., Reffner, J. R., Wolf, C. A., and Pearson, R. A. (2017). Influence of carbon black and carbon nanotubes on the conductivity, morphology, and rheology of conductive ternary polymer blends. *Polymer Engineering & Science*, 57(12):1329–1339.
- Brown, J., Lu, C.-L., Coburn, J., and Kaplan, D. L. (2015). Impact of silk biomaterial structure on proteolysis. *Acta biomaterialia*, 11:212–221.
- Buhlmann, J., Hofmann, L., Tass, P. A., and Hauptmann, C. (2011). Modeling of a segmented electrode for desynchronizing deep brain stimulation. *Frontiers in neuroengineering*, 4:15.
- Cafarelli, A., Marino, A., Vannozzi, L., Puigmartí-Luis, J., Pané, S., Ciofani, G., and Ricotti, L. (2021). Piezoelectric nanomaterials activated by ultrasound: the pathway from discovery to future clinical adoption. *ACS nano*, 15(7):11066–11086.
- Canales, A., Jia, X., Froriep, U. P., Koppes, R. A., Tringides, C. M., Selvidge, J., Lu, C., Hou, C., Wei, L., Fink, Y., et al. (2015). Multifunctional fibers for simultaneous optical, electrical and chemical interrogation of neural circuits in vivo. *Nature biotechnology*, 33(3):277–284.
- Canalón, P. (1985). Influence of temperature on various mechanisms associated with neuronal growth and nerve regeneration. *Progress in neurobiology*, 25(1):27–92.
- Cao, J., Zhu, B., Zheng, K., He, S., Meng, L., Song, J., and Yang, H. (2020). Recent progress in nir-ii contrast agent for biological imaging. *Frontiers in bioengineering and biotechnology*, 7:487.
- Cao, Y. and Wang, B. (2009). Biodegradation of silk biomaterials. *International journal of molecular sciences*, 10(4):1514–1524.
- Cardin, J. A., Carlén, M., Meletis, K., Knoblich, U., Zhang, F., Deisseroth, K., Tsai, L.-H., and Moore, C. I. (2010). Targeted optogenetic stimulation and recording of neurons in vivo using cell-type-specific expression of channelrhodopsin-2. *Nature protocols*, 5(2):247–254.
- Carriero, G., Arcieri, S., Cattalini, A., Corsi, L., Gnatkovsky, V., and de Curtis, M. (2012). A guinea pig model of mesial temporal lobe epilepsy following nonconvulsive status epilepticus induced by unilateral intrahippocampal injection of kainic acid. *Epilepsia*, 53(11):1917–1927.
- Carvalho-de Souza, J. L., Treger, J. S., Dang, B., Kent, S. B., Pepperberg, D. R., and Bezanilla, F. (2015). Photosensitivity of neurons enabled by cell-targeted gold nanoparticles. *Neuron*, 86(1):207–217.

- Cayce, J. M., Friedman, R. M., Chen, G., Jansen, E. D., Mahadevan-Jansen, A., and Roe, A. W. (2014). Infrared neural stimulation of primary visual cortex in non-human primates. *Neuroimage*, 84:181–190.
- Chen, G., Shi, L., Lan, L., Wang, R., Li, Y., Du, Z., Hyman, M., Cheng, J.-X., and Yang, C. (2022). High-precision neural stimulation by a highly efficient candle soot fiber optoacoustic emitter. *Frontiers in Neuroscience*, 16:1850.
- Chen, R., Canales, A., and Anikeeva, P. (2017). Neural recording and modulation technologies. *Nature Reviews Materials*, 2(2):1–16.
- Chen, R., Romero, G., Christiansen, M. G., Mohr, A., and Anikeeva, P. (2015). Wireless magnetothermal deep brain stimulation. *Science*, 347(6229):1477–1480.
- Chen, S., Weitemier, A. Z., Zeng, X., He, L., Wang, X., Tao, Y., Huang, A. J., Hashimoto, Y., Kano, M., Iwasaki, H., et al. (2018a). Near-infrared deep brain stimulation via upconversion nanoparticle-mediated optogenetics. *Science*, 359(6376):679–684.
- Chen, S., Zhao, R., Sun, X., Wang, H., Li, L., and Liu, J. (2023). Toxicity and biocompatibility of liquid metals. *Advanced Healthcare Materials*, 12(3):2201924.
- Chen, X., Wu, Y., Ranjan, V. D., and Zhang, Y. (2018b). Three-dimensional electrical conductive scaffold from biomaterial-based carbon microfiber sponge with bioinspired coating for cell proliferation and differentiation. *Carbon*, 134:174–182.
- Ching, S., Purdon, P. L., Vijayan, S., Kopell, N. J., and Brown, E. N. (2012). A neurophysiological-metabolic model for burst suppression. *Proceedings of the National Academy of Sciences*, 109(8):3095–3100.
- Choi, Y. S., Hsueh, Y.-Y., Koo, J., Yang, Q., Avila, R., Hu, B., Xie, Z., Lee, G., Ning, Z., Liu, C., et al. (2020). Stretchable, dynamic covalent polymers for soft, long-lived bioresorbable electronic stimulators designed to facilitate neuromuscular regeneration. *Nature communications*, 11(1):5990.
- Chow, B. Y. and Boyden, E. S. (2013). Optogenetics and translational medicine. *Science translational medicine*, 5(177):177ps5–177ps5.
- Cogan, S. F. (2008). Neural stimulation and recording electrodes. *Annu. Rev. Biomed. Eng.*, 10:275–309.
- Cohen, J. E. and Fields, R. D. (2004). Extracellular calcium depletion in synaptic transmission. *The Neuroscientist*, 10(1):12–17.

- Colchester, R. J., Mosse, C. A., Bhachu, D. S., Bear, J. C., Carmalt, C. J., Parkin, I. P., Treeby, B. E., Papakonstantinou, I., and Desjardins, A. E. (2014). Laser-generated ultrasound with optical fibres using functionalised carbon nanotube composite coatings. *Applied Physics Letters*, 104(17):173502.
- Dastin-van Rijn, E. M., Provenza, N. R., Calvert, J. S., Allawala, A. B., Darie, R., Syed, S., Matteson, E., Vogt, G. S., Avendano-Ortega, M., Vasquez, A. C., et al. (2021). Uncovering biomarkers during therapeutic neuromodulation with parrm: Period-based artifact reconstruction and removal method. *Cell reports methods*, 1(2):100010.
- Deisseroth, K. (2011). Optogenetics. *Nature methods*, 8(1):26–29.
- Delmas, P., Hao, J., and Rodat-Despoix, L. (2011). Molecular mechanisms of mechanotransduction in mammalian sensory neurons. *Nature Reviews Neuroscience*, 12(3):139–153.
- Doherty, P., Williams, G., and Williams, E.-J. (2000). Cams and axonal growth: a critical evaluation of the role of calcium and the mapk cascade. *Molecular and Cellular Neuroscience*, 16(4):283–295.
- Dunleavy, M., Shinoda, S., Schindler, C., Ewart, C., Dolan, R., Gobbo, O. L., Kerskens, C. M., and Henshall, D. C. (2010). Experimental neonatal status epilepticus and the development of temporal lobe epilepsy with unilateral hippocampal sclerosis. *The American journal of pathology*, 176(1):330–342.
- Eles, J. R., Vazquez, A. L., Snyder, N. R., Lagenaur, C., Murphy, M. C., Kozai, T. D., and Cui, X. T. (2017). Neuroadhesive li coating attenuates acute microglial attachment to neural electrodes as revealed by live two-photon microscopy. *Biomaterials*, 113:279–292.
- Fenno, L., Yizhar, O., and Deisseroth, K. (2011). The development and application of optogenetics. *Annual review of neuroscience*, 34:389–412.
- Finlay, M. C., Mosse, C. A., Colchester, R. J., Noimark, S., Zhang, E. Z., Ourselin, S., Beard, P. C., Schilling, R. J., Parkin, I. P., Papakonstantinou, I., et al. (2017). Through-needle all-optical ultrasound imaging in vivo: a preclinical swine study. *Light: Science & Applications*, 6(12):e17103–e17103.
- Foutz, T. J. and Wong, M. (2022). Brain stimulation treatments in epilepsy: basic mechanisms and clinical advances. *biomedical journal*, 45(1):27–37.
- Frank, J. A., Antonini, M.-J., and Anikeeva, P. (2019). Next-generation interfaces for studying neural function. *Nature biotechnology*, 37(9):1013–1023.

- Gangrade, A., Gawali, B., Jadi, P. K., Naidu, V. G., and Mandal, B. B. (2020). Photo-electro active nanocomposite silk hydrogel for spatiotemporal controlled release of chemotherapeutics: An in vivo approach toward suppressing solid tumor growth. *ACS applied materials & interfaces*, 12(25):27905–27916.
- Georges, P. C., Miller, W. J., Meaney, D. F., Sawyer, E. S., and Janmey, P. A. (2006). Matrices with compliance comparable to that of brain tissue select neuronal over glial growth in mixed cortical cultures. *Biophysical journal*, 90(8):3012–3018.
- Geremia, N. M., Gordon, T., Brushart, T. M., Al-Majed, A. A., and Verge, V. M. (2007). Electrical stimulation promotes sensory neuron regeneration and growth-associated gene expression. *Experimental neurology*, 205(2):347–359.
- Gooch, C. L., Pracht, E., and Borenstein, A. R. (2017). The burden of neurological disease in the united states: A summary report and call to action. *Annals of neurology*, 81(4):479–484.
- Grover, S., Fishman, G. A., Anderson, R. J., Tozatti, M. S., Heckenlively, J. R., Weleber, R. G., Edwards, A. O., and Brown Jr, J. (1999). Visual acuity impairment in patients with retinitis pigmentosa at age 45 years or older. *Ophthalmology*, 106(9):1780–1785.
- Guo, Y., Werner, C. F., Canales, A., Yu, L., Jia, X., Anikeeva, P., and Yoshinobu, T. (2020). Polymer-fiber-coupled field-effect sensors for label-free deep brain recordings. *Plos one*, 15(1):e0228076.
- Ha, G. E. and Cheong, E. (2017). Spike frequency adaptation in neurons of the central nervous system. *Experimental neurobiology*, 26(4):179.
- Han, D., Meng, Z., Wu, D., Zhang, C., and Zhu, H. (2011). Thermal properties of carbon black aqueous nanofluids for solar absorption. *Nanoscale research letters*, 6:1–7.
- Han, S., Park, J., Choi, W. S., and Youn, I. (2020). Ultrasound stimulation increases neurite regeneration in injured dorsal root ganglion neurons through mammalian target of rapamycin activation. *Brain Sciences*, 10(7):409.
- Harmsen, I. E., Elias, G. J., Beyn, M. E., Boutet, A., Pancholi, A., Germann, J., Mansouri, A., Lozano, C. S., and Lozano, A. M. (2020). Clinical trials for deep brain stimulation: current state of affairs. *Brain Stimulation*, 13(2):378–385.
- Harvey, E. N. (1929). The effect of high frequency sound waves on heart muscle and other irritable tissues. *American Journal of Physiology-Legacy Content*, 91(1):284–290.

- He, Y., Zhao, Y., Fan, L., Wang, X., Duan, M., Wang, H., Zhu, X., and Liu, J. (2021). Injectable affinity and remote magnetothermal effects of bi-based alloy for long-term bone defect repair and analgesia. *Advanced Science*, 8(14):2100719.
- Heck, C. N., King-Stephens, D., Massey, A. D., Nair, D. R., Jobst, B. C., Barkley, G. L., Salanova, V., Cole, A. J., Smith, M. C., Gwinn, R. P., et al. (2014). Two-year seizure reduction in adults with medically intractable partial onset epilepsy treated with responsive neurostimulation: final results of the rns system pivotal trial. *Epilepsia*, 55(3):432–441.
- Heinricher, M. M. (2004). Principles of extracellular single-unit recording. *Microelectrode Recording in Movement Disorder Surgery*, 8.
- Henze, D. A., Borhegyi, Z., Csicsvari, J., Mamiya, A., Harris, K. D., and Buzsaki, G. (2000). Intracellular features predicted by extracellular recordings in the hippocampus in vivo. *Journal of neurophysiology*, 84(1):390–400.
- Hilarius, K., Lellinger, D., Alig, I., Villmow, T., Pegel, S., and Pötschke, P. (2013). Influence of shear deformation on the electrical and rheological properties of combined filler networks in polymer melts: Carbon nanotubes and carbon black in polycarbonate. *Polymer*, 54(21):5865–5874.
- Hiltunen, M., Peltö, J., Ellä, V., and Kellomäki, M. (2016). Uniform and electrically conductive biopolymer-doped polypyrrole coating for fibrous pla. *Journal of Biomedical Materials Research Part B: Applied Biomaterials*, 104(8):1721–1729.
- Hodgkin, A. L. and Huxley, A. F. (1952). A quantitative description of membrane current and its application to conduction and excitation in nerve. *The Journal of physiology*, 117(4):500.
- Holmes, C., Godfrey, M., Mennea, P., Zahertar, S., and Dulieu-Barton, J. M. (2022). Flexible photonics in low stiffness doped silica for use in fibre reinforced polymer composite materials. *Optical Materials*, 134:113133.
- Horan, R. L., Antle, K., Collette, A. L., Wang, Y., Huang, J., Moreau, J. E., Volloch, V., Kaplan, D. L., and Altman, G. H. (2005). In vitro degradation of silk fibroin. *Biomaterials*, 26(17):3385–3393.
- Hu, X., Shmelev, K., Sun, L., Gil, E.-S., Park, S.-H., Cebe, P., and Kaplan, D. L. (2011). Regulation of silk material structure by temperature-controlled water vapor annealing. *Biomacromolecules*, 12(5):1686–1696.
- Huang, H., Delikanli, S., Zeng, H., Ferkey, D. M., and Pralle, A. (2010). Remote control of ion channels and neurons through magnetic-field heating of nanoparticles. *Nature nanotechnology*, 5(8):602–606.

- Huang, L., Zhu, L., Shi, X., Xia, B., Liu, Z., Zhu, S., Yang, Y., Ma, T., Cheng, P., Luo, K., et al. (2018). A compound scaffold with uniform longitudinally oriented guidance cues and a porous sheath promotes peripheral nerve regeneration in vivo. *Acta biomaterialia*, 68:223–236.
- Huang, Y., Fitzpatrick, V., Zheng, N., Cheng, R., Huang, H., Ghezzi, C., Kaplan, D. L., and Yang, C. (2020). Self-folding 3d silk biomaterial rolls to facilitate axon and bone regeneration. *Advanced healthcare materials*, 9(18):2000530.
- Hudetz, A. G., Vizuite, J. A., and Pillay, S. (2011). Differential effects of isoflurane on high-frequency and low-frequency γ oscillations in the cerebral cortex and hippocampus in freely moving rats. *The Journal of the American Society of Anesthesiologists*, 114(3):588–595.
- Hughes, C., Herrera, A., Gaunt, R., and Collinger, J. (2020). Bidirectional brain-computer interfaces. *Handbook of clinical neurology*, 168:163–181.
- Huguenard, J. (1996). Low-threshold calcium currents in central nervous system neurons. *Annual review of physiology*, 58(1):329–348.
- Hwang, J.-Y., Shin, U. S., Jang, W.-C., Hyun, J. K., Wall, I. B., and Kim, H.-W. (2013). Biofunctionalized carbon nanotubes in neural regeneration: a mini-review. *Nanoscale*, 5(2):487–497.
- Hynynen, K. and Clement, G. (2007). Clinical applications of focused ultrasound—the brain. *International Journal of Hyperthermia*, 23(2):193–202.
- Jiang, S., Patel, D. C., Kim, J., Yang, S., Mills III, W. A., Zhang, Y., Wang, K., Feng, Z., Vijayan, S., Cai, W., et al. (2020a). Spatially expandable fiber-based probes as a multifunctional deep brain interface. *Nature communications*, 11(1):6115.
- Jiang, W., Wang, Y., Tang, J., Peng, J., Wang, Y., Guo, Q., Guo, Z., Li, P., Xiao, B., and Zhang, J. (2016a). Low-intensity pulsed ultrasound treatment improved the rate of autograft peripheral nerve regeneration in rat. *Scientific reports*, 6(1):22773.
- Jiang, Y., Carvalho-de Souza, J. L., Wong, R. C., Luo, Z., Isheim, D., Zuo, X., Nicholls, A. W., Jung, I. W., Yue, J., Liu, D.-J., et al. (2016b). Heterogeneous silicon mesostructures for lipid-supported bioelectric interfaces. *Nature materials*, 15(9):1023–1030.
- Jiang, Y., Huang, Y., Luo, X., Wu, J., Zong, H., Shi, L., Cheng, R., Zhu, Y., Jiang, S., Lan, L., et al. (2021). Neural stimulation in vitro and in vivo by photoacoustic nanotransducers. *Matter*, 4(2):654–674.
- Jiang, Y., Lee, H. J., Lan, L., Tseng, H.-a., Yang, C., Man, H.-Y., Han, X., and Cheng, J.-X. (2020b). Optoacoustic brain stimulation at submillimeter spatial precision. *Nature communications*, 11(1):881.

- Jin, H.-J., Park, J., Karageorgiou, V., Kim, U.-J., Valluzzi, R., Cebe, P., and Kaplan, D. L. (2005). Water-stable silk films with reduced β -sheet content. *Advanced Functional Materials*, 15(8):1241–1247.
- Johnson, C. O., Nguyen, M., Roth, G. A., Nichols, E., Alam, T., Abate, D., Abd-Allah, F., Abdelalim, A., Abraha, H. N., Abu-Rmeileh, N. M., et al. (2019). Global, regional, and national burden of stroke, 1990–2016: a systematic analysis for the global burden of disease study 2016. *The Lancet Neurology*, 18(5):439–458.
- Jonsson, A., Inal, S., Uguz, I., Williamson, A. J., Kergoat, L., Rivnay, J., Khodagholy, D., Berggren, M., Bernard, C., Malliaras, G. G., et al. (2016). Bioelectronic neural pixel: Chemical stimulation and electrical sensing at the same site. *Proceedings of the National Academy of Sciences*, 113(34):9440–9445.
- Kandel, E. R., Schwartz, J. H., Jessell, T. M., Siegelbaum, S., Hudspeth, A. J., Mack, S., et al. (2000). *Principles of neural science*, volume 4. McGraw-hill New York.
- Karatum, O., Gwak, M.-J., Hyun, J., Onal, A., Koirala, G. R., Kim, T.-i., and Nizamoglu, S. (2023). Optical neuromodulation at all scales: from nanomaterials to wireless optoelectronics and integrated systems. *Chemical Society Reviews*.
- Kater, S. and Mills, L. (1991). Regulation of growth cone behavior by calcium. *The Journal of neuroscience*, 11(4):891.
- Khun, N. W. and Liu, E. (2013). Thermal, mechanical and tribological properties of polycarbonate/acrylonitrile-butadiene-styrene blends. *Journal of Polymer Engineering*, 33(6):535–543.
- Kim, D., Ye, M., and Grigoropoulos, C. (1998). Pulsed laser-induced ablation of absorbing liquids and acoustic-transient generation. *Applied Physics A*, 67:169–181.
- Kim, T., Kadji, H., Whalen, A. J., Ashourvan, A., Freeman, E., Fried, S. I., Tadi-gadapa, S., and Schiff, S. J. (2022). Thermal effects on neurons during stimulation of the brain. *Journal of neural engineering*, 19(5):056029.
- Klimovich, P., Rubina, K., Sysoeva, V., and Semina, E. (2020). Three-dimensional model of dorsal root ganglion explant as a method of studying neurotrophic factors in regenerative medicine. *Biomedicines*, 8(3):49.
- Klopfleisch, R. and Jung, F. (2017). The pathology of the foreign body reaction against biomaterials. *Journal of biomedical materials research Part A*, 105(3):927–940.
- Knoben, R., Alosaimi, F., Dominguez-Paredes, D., Temel, Y., and Jahanshahi, A. (2022). Nanomaterials in neuromodulation: what is the potential? *Expert Review of Neurotherapeutics*, 22(4):287–290.

- Koessler, L., Colnat-Coulbois, S., Cecchin, T., Hofmanis, J., Dmochowski, J. P., Norcia, A. M., and Maillard, L. G. (2017). In-vivo measurements of human brain tissue conductivity using focal electrical current injection through intracerebral multicontact electrodes. *Human brain mapping*, 38(2):974–986.
- Koo, J., MacEwan, M. R., Kang, S.-K., Won, S. M., Stephen, M., Gamble, P., Xie, Z., Yan, Y., Chen, Y.-Y., Shin, J., et al. (2018). Wireless bioresorbable electronic system enables sustained nonpharmacological neuroregenerative therapy. *Nature medicine*, 24(12):1830–1836.
- Kozai, T. D., Jaquins-Gerstl, A. S., Vazquez, A. L., Michael, A. C., and Cui, X. T. (2015). Brain tissue responses to neural implants impact signal sensitivity and intervention strategies. *ACS chemical neuroscience*, 6(1):48–67.
- Krasovitski, B., Frenkel, V., Shoham, S., and Kimmel, E. (2011). Intramembrane cavitation as a unifying mechanism for ultrasound-induced bioeffects. *Proceedings of the National Academy of Sciences*, 108(8):3258–3263.
- Kravitz, A. V., Owen, S. F., and Kreitzer, A. C. (2013). Optogenetic identification of striatal projection neuron subtypes during in vivo recordings. *Brain research*, 1511:21–32.
- Kubaneck, J., Shi, J., Marsh, J., Chen, D., Deng, C., and Cui, J. (2016). Ultrasound modulates ion channel currents. *Scientific reports*, 6(1):1–14.
- Kubaneck, J., Shukla, P., Das, A., Baccus, S. A., and Goodman, M. B. (2018). Ultrasound elicits behavioral responses through mechanical effects on neurons and ion channels in a simple nervous system. *Journal of Neuroscience*, 38(12):3081–3091.
- Lancaster, B. and Wheal, H. V. (1982). A comparative histological and electrophysiological study of some neurotoxins in the rat hippocampus. *Journal of Comparative Neurology*, 211(2):105–114.
- Lavrador, P., Esteves, M. R., Gaspar, V. M., and Mano, J. F. (2021). Stimuli-responsive nanocomposite hydrogels for biomedical applications. *Advanced Functional Materials*, 31(8):2005941.
- Lee, A. C., Vivian, M. Y., Lowe III, J. B., Brenner, M. J., Hunter, D. A., Mackinnon, S. E., and Sakiyama-Elbert, S. E. (2003). Controlled release of nerve growth factor enhances sciatic nerve regeneration. *Experimental neurology*, 184(1):295–303.
- Lee, T., Baac, H. W., Li, Q., and Guo, L. J. (2018). Efficient photoacoustic conversion in optical nanomaterials and composites. *Advanced Optical Materials*, 6(24):1800491.

- Lever, I. J., Bradbury, E. J., Cunningham, J. R., Adelson, D. W., Jones, M. G., McMahon, S. B., Marvizón, J. C. G., and Malcangio, M. (2001). Brain-derived neurotrophic factor is released in the dorsal horn by distinctive patterns of afferent fiber stimulation. *Journal of Neuroscience*, 21(12):4469–4477.
- Lévesque, M. and Avoli, M. (2013). The kainic acid model of temporal lobe epilepsy. *Neuroscience & Biobehavioral Reviews*, 37(10):2887–2899.
- Lewis, P. M., Thomson, R. H., Rosenfeld, J. V., and Fitzgerald, P. B. (2016). Brain neuromodulation techniques: a review. *The neuroscientist*, 22(4):406–421.
- Li, C., Guo, C., Fitzpatrick, V., Ibrahim, A., Zwierstra, M. J., Hanna, P., Lechtig, A., Nazarian, A., Lin, S. J., and Kaplan, D. L. (2020). Design of biodegradable, implantable devices towards clinical translation. *Nature Reviews Materials*, 5(1):61–81.
- Li, N., Zhang, Q., Gao, S., Song, Q., Huang, R., Wang, L., Liu, L., Dai, J., Tang, M., and Cheng, G. (2013). Three-dimensional graphene foam as a biocompatible and conductive scaffold for neural stem cells. *Scientific reports*, 3(1):1–6.
- Li, R., Li, Y., Wu, Y., Zhao, Y., Chen, H., Yuan, Y., Xu, K., Zhang, H., Lu, Y., Wang, J., et al. (2018). Heparin-polyoxamer thermosensitive hydrogel loaded with bfgf and ngf enhances peripheral nerve regeneration in diabetic rats. *Biomaterials*, 168:24–37.
- Lim, L. S., Mitchell, P., Seddon, J. M., Holz, F. G., and Wong, T. Y. (2012). Age-related macular degeneration. *The Lancet*, 379(9827):1728–1738.
- Lin, C.-R., Chen, K.-H., Yang, C.-H., Cheng, J.-T., Sheen-Chen, S.-M., Wu, C.-H., Sy, W.-D., and Chen, Y.-S. (2010). Sonoporation-mediated gene transfer into adult rat dorsal root ganglion cells. *Journal of biomedical science*, 17:1–6.
- Liu, L., Chen, B., Liu, K., Gao, J., Ye, Y., Wang, Z., Qin, N., Wilson, D. A., Tu, Y., and Peng, F. (2020). Wireless manipulation of magnetic/piezoelectric micromotors for precise neural stem-like cell stimulation. *Advanced Functional Materials*, 30(11):1910108.
- Liu, Y., Geng, Y., Yue, B., Lo, P.-C., Huang, J., and Jin, H. (2022). Injectable hydrogel as a unique platform for antitumor therapy targeting immunosuppressive tumor microenvironment. *Frontiers in Immunology*, 12:832942.
- Lu, Z., Piechowicz, M., and Qiu, S. (2016). A simplified method for ultra-low density, long-term primary hippocampal neuron culture. *Journal of visualized experiments: JoVE*, 1(109).

- Lyu, Y., Xie, C., Chechetka, S. A., Miyako, E., and Pu, K. (2016). Semiconducting polymer nanobioconjugates for targeted photothermal activation of neurons. *Journal of the American Chemical Society*, 138(29):9049–9052.
- Macaya, D. and Spector, M. (2012). Injectable hydrogel materials for spinal cord regeneration: a review. *Biomedical materials*, 7(1):012001.
- Mahar, M. and Cavalli, V. (2018). Intrinsic mechanisms of neuronal axon regeneration. *Nature Reviews Neuroscience*, 19(6):323–337.
- Mandal, B. B., Grinberg, A., Seok Gil, E., Panilaitis, B., and Kaplan, D. L. (2012). High-strength silk protein scaffolds for bone repair. *Proceedings of the National Academy of Sciences*, 109(20):7699–7704.
- Marino, A., Arai, S., Hou, Y., Sinibaldi, E., Pellegrino, M., Chang, Y.-T., Mazzolai, B., Mattoli, V., Suzuki, M., and Ciofani, G. (2015). Piezoelectric nanoparticle-assisted wireless neuronal stimulation. *ACS nano*, 9(7):7678–7689.
- Maya-Vetencourt, J. F., Manfredi, G., Mete, M., Colombo, E., Bramini, M., Di Marco, S., Shmal, D., Mantero, G., Dipalo, M., Rocchi, A., et al. (2020). Subretinally injected semiconducting polymer nanoparticles rescue vision in a rat model of retinal dystrophy. *Nature nanotechnology*, 15(8):698–708.
- McKemy, D. D., Neuhausser, W. M., and Julius, D. (2002). Identification of a cold receptor reveals a general role for trp channels in thermosensation. *Nature*, 416(6876):52–58.
- Meneghetti, M., Kaur, J., Sui, K., Sørensen, J. F., Berg, R. W., and Markos, C. (2022). Opsin-free optical neuromodulation and electrophysiology enabled by a soft monolithic infrared multifunctional neural interface. *bioRxiv*, pages 2022–05.
- Meyer-Franke, A., Wilkinson, G. A., Kruttgen, A., Hu, M., Munro, E., Hanson, M. G., Reichardt, L. F., and Barres, B. A. (1998). Depolarization and camp elevation rapidly recruit trkb to the plasma membrane of cns neurons. *Neuron*, 21(4):681–693.
- Miocinovic, S., Lempka, S. F., Russo, G. S., Maks, C. B., Butson, C. R., Sakaie, K. E., Vitek, J. L., and McIntyre, C. C. (2009). Experimental and theoretical characterization of the voltage distribution generated by deep brain stimulation. *Experimental neurology*, 216(1):166–176.
- Molino, P. J., Garcia, L., Stewart, E. M., Lamaze, M., Zhang, B., Harris, A. R., Winberg, P., and Wallace, G. G. (2018). Pedot doped with algal, mammalian and synthetic dopants: polymer properties, protein and cell interactions, and influence of electrical stimulation on neuronal cell differentiation. *Biomaterials science*, 6(5):1250–1261.

- Nakatsuji, H., Numata, T., Morone, N., Kaneko, S., Mori, Y., Imahori, H., and Murakami, T. (2015). Thermosensitive ion channel activation in single neuronal cells by using surface-engineered plasmonic nanoparticles. *Angewandte Chemie International Edition*, 54(40):11725–11729.
- Nie, Y., Guo, X., Li, X., Geng, X., Li, Y., Quan, Z., Zhu, G., Yin, Z., Zhang, J., and Wang, S. (2021). Real-time removal of stimulation artifacts in closed-loop deep brain stimulation. *Journal of Neural Engineering*, 18(6):066031.
- Noimark, S., Colchester, R. J., Blackburn, B. J., Zhang, E. Z., Alles, E. J., Ourselin, S., Beard, P. C., Papakonstantinou, I., Parkin, I. P., and Desjardins, A. E. (2016). Carbon-nanotube–pdms composite coatings on optical fibers for all-optical ultrasound imaging. *Advanced Functional Materials*, 26(46):8390–8396.
- Ordaz, J. D., Wu, W., and Xu, X.-M. (2017). Optogenetics and its application in neural degeneration and regeneration. *Neural Regeneration Research*, 12(8):1197.
- Orhan, E., Dalkara, D., Neuillé, M., Lechauve, C., Michiels, C., Picaud, S., Léveillard, T., Sahel, J.-A., Naash, M. I., Lavail, M. M., et al. (2015). Genotypic and phenotypic characterization of p23h line 1 rat model. *PLoS One*, 10(5):e0127319.
- Oyama, A. M. and Itiki, C. (2010). Influence of evoked response latency and amplitude on stimulus artifact removal. In *2010 Annual International Conference of the IEEE Engineering in Medicine and Biology*, pages 6091–6094. IEEE.
- Paff, M., Loh, A., Sarica, C., Lozano, A. M., and Fasano, A. (2020). Update on current technologies for deep brain stimulation in parkinson’s disease. *Journal of movement disorders*, 13(3):185.
- Park, S., Guo, Y., Jia, X., Choe, H. K., Grena, B., Kang, J., Park, J., Lu, C., Canales, A., Chen, R., et al. (2017). One-step optogenetics with multifunctional flexible polymer fibers. *Nature neuroscience*, 20(4):612–619.
- Park, S., Koppes, R. A., Froriep, U. P., Jia, X., Achyuta, A. K. H., McLaughlin, B. L., and Anikeeva, P. (2015a). Optogenetic control of nerve growth. *Scientific reports*, 5(1):9669.
- Park, S., Yuk, H., Zhao, R., Yim, Y. S., Woldeghebriel, E. W., Kang, J., Canales, A., Fink, Y., Choi, G. B., Zhao, X., et al. (2021). Adaptive and multifunctional hydrogel hybrid probes for long-term sensing and modulation of neural activity. *Nature communications*, 12(1):3435.
- Park, S. I., Brenner, D. S., Shin, G., Morgan, C. D., Copits, B. A., Chung, H. U., Pullen, M. Y., Noh, K. N., Davidson, S., Oh, S. J., et al. (2015b). Soft, stretchable, fully implantable miniaturized optoelectronic systems for wireless optogenetics. *Nature biotechnology*, 33(12):1280–1286.

- Parmeggiani, F. (2011). Editorial [hot topic: clinics, epidemiology and genetics of retinitis pigmentosa (guest editor: francesco parmeggiani)]. *Current genomics*, 12(4):236–237.
- Paschen, E., Elgueta, C., Heining, K., Vieira, D. M., Kleis, P., Orcinha, C., Häussler, U., Bartos, M., Egert, U., Janz, P., et al. (2020). Hippocampal low-frequency stimulation prevents seizure generation in a mouse model of mesial temporal lobe epilepsy. *Elife*, 9:e54518.
- Patapoutian, A., Peier, A. M., Story, G. M., and Viswanath, V. (2003). Thermotrp channels and beyond: mechanisms of temperature sensation. *Nature Reviews Neuroscience*, 4(7):529–539.
- Paulk, A. C., Kirszenblat, L., Zhou, Y., and van Swinderen, B. (2015). Closed-loop behavioral control increases coherence in the fly brain. *Journal of Neuroscience*, 35(28):10304–10315.
- Paz, J. T., Davidson, T. J., Frechette, E. S., Delord, B., Parada, I., Peng, K., Deisseroth, K., and Huguenard, J. R. (2013). Closed-loop optogenetic control of thalamus as a tool for interrupting seizures after cortical injury. *Nature neuroscience*, 16(1):64–70.
- Peier, A. M., Moqrich, A., Hergarden, A. C., Reeve, A. J., Andersson, D. A., Story, G. M., Earley, T. J., Dragoni, I., McIntyre, P., Bevan, S., et al. (2002). A trp channel that senses cold stimuli and menthol. *Cell*, 108(5):705–715.
- Pisanello, F., Sileo, L., Oldenburg, I. A., Pisanello, M., Martiradonna, L., Assad, J. A., Sabatini, B. L., and De Vittorio, M. (2014). Multipoint-emitting optical fibers for spatially addressable in vivo optogenetics. *Neuron*, 82(6):1245–1254.
- Plaksin, M., Shoham, S., and Kimmel, E. (2014). Intramembrane cavitation as a predictive bio-piezoelectric mechanism for ultrasonic brain stimulation. *Physical review X*, 4(1):011004.
- Poduval, R. K., Noimark, S., Colchester, R. J., Macdonald, T. J., Parkin, I. P., Desjardins, A. E., and Papakonstantinou, I. (2017). Optical fiber ultrasound transmitter with electrospun carbon nanotube-polymer composite. *Applied physics letters*, 110(22):223701.
- Pritchard, E. M. and Kaplan, D. L. (2011). Silk fibroin biomaterials for controlled release drug delivery. *Expert opinion on drug delivery*, 8(6):797–811.
- Qian, X., Chen, Y., Feng, Y., Ma, B., Hao, H., and Li, L. (2016). A method for removal of deep brain stimulation artifact from local field potentials. *IEEE Transactions on Neural Systems and Rehabilitation Engineering*, 25(12):2217–2226.

- Raedt, R., Van Dycke, A., Van Melkebeke, D., De Smedt, T., Claeys, P., Wyckhuys, T., Vonck, K., Wadman, W., and Boon, P. (2009). Seizures in the intrahippocampal kainic acid epilepsy model: characterization using long-term video-EEG monitoring in the rat. *Acta Neurologica Scandinavica*, 119(5):293–303.
- Rastogi, S. K., Garg, R., Scopelliti, M. G., Pinto, B. I., Hartung, J. E., Kim, S., Murphey, C. G., Johnson, N., San Roman, D., Bezanilla, F., et al. (2020). Remote nongenetic optical modulation of neuronal activity using fuzzy graphene. *Proceedings of the National Academy of Sciences*, 117(24):13339–13349.
- Rockwood, D. N., Preda, R. C., Yücel, T., Wang, X., Lovett, M. L., and Kaplan, D. L. (2011). Materials fabrication from bombyx mori silk fibroin. *Nature protocols*, 6(10):1612–1631.
- Ronzani, C., Cottineau, T., Gonzalez-Valls, I., Keller, V., Picaud, S., Keller, N., and Roux, M. J. (2018). High-frequency stimulation of normal and blind mouse retinas using tio₂ nanotubes. *Advanced Functional Materials*, 28(50):1804639.
- Rosencwaig, A. and Gersho, A. (1976). Theory of the photoacoustic effect with solids. *Journal of Applied Physics*, 47(1):64–69.
- Rosin, B., Slovik, M., Mitelman, R., Rivlin-Etzion, M., Haber, S. N., Israel, Z., Vaadia, E., and Bergman, H. (2011). Closed-loop deep brain stimulation is superior in ameliorating parkinsonism. *Neuron*, 72(2):370–384.
- Royer, S., Zemelman, B. V., Barbic, M., Losonczy, A., Buzsáki, G., and Magee, J. C. (2010). Multi-array silicon probes with integrated optical fibers: light-assisted perturbation and recording of local neural circuits in the behaving animal. *European Journal of Neuroscience*, 31(12):2279–2291.
- Sekirnjak, C., Hulse, C., Jepson, L. H., Hottowy, P., Sher, A., Dabrowski, W., Litke, A. M., and Chichilnisky, E. (2009). Loss of responses to visual but not electrical stimulation in ganglion cells of rats with severe photoreceptor degeneration. *Journal of neurophysiology*, 102(6):3260–3269.
- Şen, T., Tüfekçioğlu, O., and Koza, Y. (2015). Mechanical index. *Anatolian journal of cardiology*, 15(4):334.
- Shao, J., Ruan, C., Xie, H., Li, Z., Wang, H., Chu, P. K., and Yu, X.-F. (2018). Black-phosphorus-incorporated hydrogel as a sprayable and biodegradable photothermal platform for postsurgical treatment of cancer. *Advanced Science*, 5(5):1700848.
- Shapiro, M. G., Homma, K., Villarreal, S., Richter, C.-P., and Bezanilla, F. (2012). Infrared light excites cells by changing their electrical capacitance. *Nature communications*, 3(1):736.

- Shi, K., Liu, Z., Wei, Y.-Y., Wang, W., Ju, X.-J., Xie, R., and Chu, L.-Y. (2015). Near-infrared light-responsive poly (n-isopropylacrylamide)/graphene oxide nanocomposite hydrogels with ultrahigh tensibility. *ACS applied materials & interfaces*, 7(49):27289–27298.
- Shi, L., Jiang, Y., Fernandez, F. R., Chen, G., Lan, L., Man, H.-Y., White, J. A., Cheng, J.-X., and Yang, C. (2021). Non-genetic photoacoustic stimulation of single neurons by a tapered fiber optoacoustic emitter. *Light: Science & Applications*, 10(1):143.
- Shi, L., Jiang, Y., Zhang, Y., Lan, L., Huang, Y., Cheng, J.-X., and Yang, C. (2020). A fiber optoacoustic emitter with controlled ultrasound frequency for cell membrane sonoporation at submillimeter spatial resolution. *Photoacoustics*, 20:100208.
- Shi, L., Jiang, Y., Zheng, N., Cheng, J.-X., and Yang, C. (2022). High-precision neural stimulation through optoacoustic emitters. *Neurophotonics*, 9(3):032207.
- Shi, Z., Zheng, F., Zhou, Z., Li, M., Fan, Z., Ye, H., Zhang, S., Xiao, T., Chen, L., Tao, T. H., et al. (2019). Silk-enabled conformal multifunctional bioelectronics for investigation of spatiotemporal epileptiform activities and multimodal neural encoding/decoding. *Advanced Science*, 6(9):1801617.
- Simunovic, M., Shen, W., Lin, J., Protti, D., Lisowski, L., and Gillies, M. (2019). Optogenetic approaches to vision restoration. *Experimental eye research*, 178:15–26.
- Smetters, D., Majewska, A., and Yuste, R. (1999). Detecting action potentials in neuronal populations with calcium imaging. *Methods*, 18(2):215–221.
- Sohal, V. S., Zhang, F., Yizhar, O., and Deisseroth, K. (2009). Parvalbumin neurons and gamma rhythms enhance cortical circuit performance. *Nature*, 459(7247):698–702.
- Sorrentino, F., Gallenga, C., Bonifazzi, C., and Perri, P. (2016). A challenge to the striking genotypic heterogeneity of retinitis pigmentosa: a better understanding of the pathophysiology using the newest genetic strategies. *Eye*, 30(12):1542–1548.
- Spencer, S. and Huh, L. (2008). Outcomes of epilepsy surgery in adults and children. *The Lancet Neurology*, 7(6):525–537.
- Stanslaski, S., Afshar, P., Cong, P., Giftakis, J., Stypulkowski, P., Carlson, D., Linde, D., Ullestad, D., Avestruz, A.-T., and Denison, T. (2012). Design and validation of a fully implantable, chronic, closed-loop neuromodulation device with concurrent sensing and stimulation. *IEEE Transactions on Neural Systems and Rehabilitation Engineering*, 20(4):410–421.

- Sui, K., Meneghetti, M., Kaur, J., Sørensen, R. J. F., Berg, R. W., and Markos, C. (2022). Adaptive polymer fiber neural device for drug delivery and enlarged illumination angle for neuromodulation. *Journal of Neural Engineering*, 19(1):016035.
- Sun, F. T. and Morrell, M. J. (2014). The rns system: responsive cortical stimulation for the treatment of refractory partial epilepsy. *Expert review of medical devices*, 11(6):563–572.
- Tam, A. C. (1986). Applications of photoacoustic sensing techniques. *Reviews of Modern Physics*, 58(2):381.
- Tao, X., West, A. E., Chen, W. G., Corfas, G., and Greenberg, M. E. (2002). A calcium-responsive transcription factor, carf, that regulates neuronal activity-dependent expression of bdnf. *Neuron*, 33(3):383–395.
- Tufail, Y., Matyushov, A., Baldwin, N., Tauchmann, M. L., Georges, J., Yoshihiro, A., Tillery, S. I. H., and Tyler, W. J. (2010). Transcranial pulsed ultrasound stimulates intact brain circuits. *Neuron*, 66(5):681–694.
- Tufail, Y., Yoshihiro, A., Pati, S., Li, M. M., and Tyler, W. J. (2011). Ultrasonic neuromodulation by brain stimulation with transcranial ultrasound. *nature protocols*, 6(9):1453–1470.
- Tyler, W. J. (2011). Noninvasive neuromodulation with ultrasound? a continuum mechanics hypothesis. *The Neuroscientist*, 17(1):25–36.
- Tyler, W. J., Lani, S. W., and Hwang, G. M. (2018). Ultrasonic modulation of neural circuit activity. *Current opinion in neurobiology*, 50:222–231.
- Ung, K. and Arenkiel, B. R. (2012). Fiber-optic implantation for chronic optogenetic stimulation of brain tissue. *JoVE (Journal of Visualized Experiments)*, 1(68):e50004.
- Vázquez-Guardado, A., Yang, Y., Bandodkar, A. J., and Rogers, J. A. (2020). Recent advances in neurotechnologies with broad potential for neuroscience research. *Nature neuroscience*, 23(12):1522–1536.
- Vinogradov, A. and Holloway, F. (1999). Electro-mechanical properties of the piezoelectric polymer pvdf. *Ferroelectrics*, 226(1):169–181.
- Vöröslakos, M., Kim, K., Slager, N., Ko, E., Oh, S., Parizi, S. S., Hendrix, B., Seymour, J. P., Wise, K. D., Buzsáki, G., et al. (2022). Hectostar μ led optoelectrodes for large-scale, high-precision in vivo opto-electrophysiology. *Advanced Science*, 9(18):2105414.

- Wang, J., Wagner, F., Borton, D. A., Zhang, J., Ozden, I., Burwell, R. D., Nurmikko, A. V., van Wagenen, R., Diester, I., and Deisseroth, K. (2011). Integrated device for combined optical neuromodulation and electrical recording for chronic in vivo applications. *Journal of neural engineering*, 9(1):016001.
- Wang, L. V. and Hu, S. (2012). Photoacoustic tomography: in vivo imaging from organelles to organs. *science*, 335(6075):1458–1462.
- Wang, L. V. and Wu, H.-i. (2012). *Biomedical optics: principles and imaging*. John Wiley & Sons.
- Wang, Y., Garg, R., Hartung, J. E., Goad, A., Patel, D. A., Vitale, F., Gold, M. S., Gogotsi, Y., and Cohen-Karni, T. (2021). Ti₃C₂T_x mxene flakes for optical control of neuronal electrical activity. *ACS nano*, 15(9):14662–14671.
- Wang, Y., Rudym, D. D., Walsh, A., Abrahamsen, L., Kim, H.-J., Kim, H. S., Kirker-Head, C., and Kaplan, D. L. (2008). In vivo degradation of three-dimensional silk fibroin scaffolds. *Biomaterials*, 29(24-25):3415–3428.
- Wells, P. (1975). Absorption and dispersion of ultrasound in biological tissue. *Ultrasound in medicine & biology*, 1(4):369–376.
- Wemmie, J. A., Taugher, R. J., and Kreple, C. J. (2013). Acid-sensing ion channels in pain and disease. *Nature Reviews Neuroscience*, 14(7):461–471.
- West, A. E., Chen, W. G., Dalva, M. B., Dolmetsch, R. E., Kornhauser, J. M., Shaywitz, A. J., Takasu, M. A., Tao, X., and Greenberg, M. E. (2001). Calcium regulation of neuronal gene expression. *Proceedings of the National Academy of Sciences*, 98(20):11024–11031.
- Wilbrecht, L. and Shohamy, D. (2009). Neural circuits can bridge systems and cognitive neuroscience. *Frontiers in Human Neuroscience*, 9:81.
- Won Baac, H., Ok, J. G., Park, H. J., Ling, T., Chen, S.-L., Hart, A. J., and Guo, L. J. (2010). Carbon nanotube composite optoacoustic transmitters for strong and high frequency ultrasound generation. *Applied physics letters*, 97(23):234104.
- Wong, W. L., Su, X., Li, X., Cheung, C. M. G., Klein, R., Cheng, C.-Y., and Wong, T. Y. (2014). Global prevalence of age-related macular degeneration and disease burden projection for 2020 and 2040: a systematic review and meta-analysis. *The Lancet Global Health*, 2(2):e106–e116.
- Wu, F., Stark, E., Ku, P.-C., Wise, K. D., Buzsáki, G., and Yoon, E. (2015). Monolithically integrated μ LEDs on silicon neural probes for high-resolution optogenetic studies in behaving animals. *Neuron*, 88(6):1136–1148.

- Xu, C., Xu, Y., Yang, M., Chang, Y., Nie, A., Liu, Z., Wang, J., and Luo, Z. (2020). Black-phosphorus-incorporated hydrogel as a conductive and biodegradable platform for enhancement of the neural differentiation of mesenchymal stem cells. *Advanced Functional Materials*, 30(39):2000177.
- Xu, H., Holzwarth, J. M., Yan, Y., Xu, P., Zheng, H., Yin, Y., Li, S., and Ma, P. X. (2014). Conductive ppy/pdlla conduit for peripheral nerve regeneration. *Biomaterials*, 35(1):225–235.
- Xu, M. and Wang, L. V. (2006). Photoacoustic imaging in biomedicine. *Review of scientific instruments*, 77(4):041101.
- Yang, W. and Yuste, R. (2017). In vivo imaging of neural activity. *Nature methods*, 14(4):349–359.
- Ye, J., Tang, S., Meng, L., Li, X., Wen, X., Chen, S., Niu, L., Li, X., Qiu, W., Hu, H., et al. (2018). Ultrasonic control of neural activity through activation of the mechanosensitive channel mscl. *Nano letters*, 18(7):4148–4155.
- Yi, L., Jin, C., Wang, L., and Liu, J. (2014). Liquid-solid phase transition alloy as reversible and rapid molding bone cement. *Biomaterials*, 35(37):9789–9801.
- Yoo, M., Koo, H., Kim, M., Kim, H.-I., and Kim, S. (2013). Near-infrared stimulation on globus pallidus and subthalamus. *Journal of Biomedical Optics*, 18(12):128005–128005.
- Yoo, S., Mittelstein, D. R., Hurt, R. C., Lacroix, J., and Shapiro, M. G. (2022). Focused ultrasound excites cortical neurons via mechanosensitive calcium accumulation and ion channel amplification. *Nature communications*, 13(1):493.
- Zeng, F.-G., Rebscher, S., Harrison, W., Sun, X., and Feng, H. (2008). Cochlear implants: system design, integration, and evaluation. *IEEE reviews in biomedical engineering*, 1:115–142.
- Zhang, F., Gradinaru, V., Adamantidis, A. R., Durand, R., Airan, R. D., De Lecea, L., and Deisseroth, K. (2010). Optogenetic interrogation of neural circuits: technology for probing mammalian brain structures. *Nature protocols*, 5(3):439–456.
- Zhang, H., Pei, W., Yang, X., Guo, X., Xing, X., Liu, R., Liu, Y., Gui, Q., and Chen, H. (2016). A sapphire based monolithic integrated optrode. In *2016 38th Annual International Conference of the IEEE Engineering in Medicine and Biology Society (EMBC)*, pages 6186–6189. IEEE.
- Zhang, J., Laiwalla, F., Kim, J. A., Urabe, H., Van Wagenen, R., Song, Y.-K., Connors, B. W., Zhang, F., Deisseroth, K., and Nurmikko, A. V. (2009). Integrated device for optical stimulation and spatiotemporal electrical recording of neural activity in light-sensitized brain tissue. *Journal of neural engineering*, 6(5):055007.

- Zhao, G., Zhang, X., Li, B., Huang, G., Xu, F., and Zhang, X. (2020). Solvent-free fabrication of carbon nanotube/silk fibroin electrospun matrices for enhancing cardiomyocyte functionalities. *ACS Biomaterials Science & Engineering*, 6(3):1630–1640.
- Zhao, Z., Gong, R., Huang, H., and Wang, J. (2016). Design, fabrication, simulation and characterization of a novel dual-sided microelectrode array for deep brain recording and stimulation. *Sensors*, 16(6):880.
- Zhigilei, L. V. and Garrison, B. J. (2000). Microscopic mechanisms of laser ablation of organic solids in the thermal and stress confinement irradiation regimes. *Journal of Applied Physics*, 88(3):1281–1298.
- Zhou, A., Johnson, B. C., and Muller, R. (2018). Toward true closed-loop neuro-modulation: artifact-free recording during stimulation. *Current opinion in neurobiology*, 50:119–127.
- Zhu, L., Luo, D., and Liu, Y. (2020). Effect of the nano/microscale structure of biomaterial scaffolds on bone regeneration. *International Journal of Oral Science*, 12(1):6.
- Zou, Y., Qin, J., Huang, Z., Yin, G., Pu, X., and He, D. (2016). Fabrication of aligned conducting ppy-plla fiber films and their electrically controlled guidance and orientation for neurites. *ACS applied materials & interfaces*, 8(20):12576–12582.

CURRICULUM VITAE

